ARMY RESEARCH LABORATORY



Experimental Investigations of Wave and Fracture Phenomena in Impacted Ceramics and Glasses

E. Straβburger
H. Senf

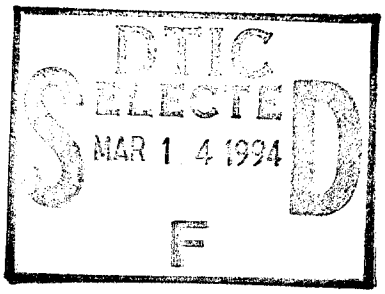
ARL-CR-214 February 1995

prepared by

Fraunhofer-Institut Für Kurzzeitdynamik
Ernst-Mach-Institut
Weil am Rhein, Germany

under contract

DAJA 45-90-C-0053



19950310 057

APPROVED FOR PUBLIC RELEASE; DISTRIBUTION IS UNLIMITED.

NOTICES

Destroy this report when it is no longer needed. DO NOT return it to the originator.

Additional copies of this report may be obtained from the National Technical Information Service, U.S. Department of Commerce, 5285 Port Royal Road, Springfield, VA 22161.

The findings of this report are not to be construed as an official Department of the Army position, unless so designated by other authorized documents.

The use of trade names or manufacturers' names in this report does not constitute endorsement of any commercial product.

REPORT DOCUMENTATION PAGE

Form Approved
OMB No. 0704-0188

Public reporting burden for this collection of information is estimated to average 1 hour per response, including the time for reviewing instructions, searching existing data sources, gathering and maintaining the data needed, and completing and reviewing the collection of information. Send comments regarding this burden estimate or any other aspect of this collection of information, including suggestions for reducing this burden, to Washington Headquarters Services, Directorate for Information Operations and Reports, 1215 Jefferson Davis Highway, Suite 1204, Arlington, VA 22202-4302, and to the Office of Management and Budget, Paperwork Reduction Project (0704-0188), Washington, DC 20503.

1. AGENCY USE ONLY *(Leave blank)*	2. REPORT DATE	3. REPORT TYPE AND DATES COVERED
	February 1995	Final, September 1990—June 1994

4. TITLE AND SUBTITLE

Experimental Investigations of Wave and Fracture Phenomena in Impacted Ceramics and Glasses

5. FUNDING NUMBERS

C: DAJA 45-90-C-0053

6. AUTHOR(S)

E. Straßburger and H. Senf

7. PERFORMING ORGANIZATION NAME(S) AND ADDRESS(ES)

Fraunhofer-Institut Für Kurzzeitdynamik
Ernst-Mach-Institut
Weil am Rhein, Germany

8. PERFORMING ORGANIZATION REPORT NUMBER

9. SPONSORING / MONITORING AGENCY NAME(S) AND ADDRESS(ES)

U.S. Army Research Laboratory
ATTN: AMSRL-OP-AP-L
Aberdeen Proving Ground, MD 21005-5066

10. SPONSORING / MONITORING AGENCY REPORT NUMBER

ARL-CR-214

11. SUPPLEMENTARY NOTES

Point of contact for this report is William A. Gooch, Jr., U.S. Army Research Laboratory, ATTN: AMSRL-WT-TA, Aberdeen Proving Ground, MD 21005-5066.

12a. DISTRIBUTION / AVAILABILITY STATEMENT

Approved for public release; distribution is unlimited.

12b. DISTRIBUTION CODE

13. ABSTRACT *(Maximum 200 words)*

Four types of glass which differ in their chemical composition, hardness and material density and tiles of SiC, TiB_2, and Al_2O_3 were impacted edge-on with blunt steel projectiles at striking velocities between 20 m/s and 1000 m/s. The propagation of shock waves and primary and secondary cracks and crack systems and the growing of crack systems from nucleated centers were visualized by means of a Cranz-Schardin high-speed camera within the first 20 µs before the projectile penetrated the target more than a few millimeters. The concept of damage velocity was introduced to describe the different damage processes quantitatively. All four types of glass revealed a similar behavior. The damage velocity equaled terminal crack velocity at low loadings, rose to transversal wave velocity when nucleation occurred and approached longitudinal wave velocity with very high loadings. Unlike glass, the ceramics generated different types of cracks, and different fracture velocities were observed at one impact velocity in one specimen. One had to distinguish between the velocity of continuously growing cracks, including the secondary cracks with sharp edges, fuzzy crack traces and crack fronts. In each of the ceramics, the damage velocity increased with increasing striking velocity and approached the longitudinal wave velocity at high loadings. A terminal crack velocity was found for one type of fracture in SiC. Ceramographical investigations of TiB_2 fragments have shown that cracks within large grains as well as intercrystalline cracks are generated by coalescence of voids.

14. SUBJECT TERMS

glasses, ceramics, SiC, TiB_2, Al_2O_3, impact, edge-on experiments, energy transfer, high-speed photography, damage velocity, terminal crack velocity, nucleation

15. NUMBER OF PAGES
140

16. PRICE CODE

17. SECURITY CLASSIFICATION OF REPORT	18. SECURITY CLASSIFICATION OF THIS PAGE	19. SECURITY CLASSIFICATION OF ABSTRACT	20. LIMITATION OF ABSTRACT
UNCLASSIFIED	UNCLASSIFIED	UNCLASSIFIED	UL

INTENTIONALLY LEFT BLANK.

PREFACE

This report documents the experimental investigation of wave and fracture phenomena in impacted glasses and ceramics that was conducted for the U.S. Army Research Laboratory (ARL) by the Fraunhofer-Institut Für Kurzzeitdynamik Ernst-Mach-Institut, Weil am Rhein, Germany. The work was conducted over a three-year period and provides significant insight into the crack and fracture of both ceramics and glasses. The work was made possible by the state-of-the-art, high-speed photographic capability available at the Ernst-Mach-Institut, specifically two 24-spark Cranz-Shradin cameras, which were used both in transmission and reflectance. This equipment allowed observation of the damage and fracture effects on the materials when impacted by a penetrator up to 1000 m/s. Twenty-four high quality photographic images could be obtained at predetermined time intervals of less than 1 μs from one or two sides of the tiles concurrently.

The report was originally published as the final report to contract no. DAJA 45-90-C-0053, prepared for the European Research Office (ERO) of the U.S. Army which oversaw the contract for the Armor Mechanics Branch, Terminal Effects Division, Weapons Technology Directorate of ARL. The Armor Mechanics Branch would like to specifically thank Dr. Reichenbach of ERO for his assistance in this matter.

The Armor Mechanics Branch would also like to acknowledge the long-term professional interaction with Mr. Senf, Mr. Straßburger and Mr.Rothenhäusler which has led to many fruitful technical exchanges during the course of this work. Further fracture and crack analysis are expected on other ceramics of interest in the future.

Any questions or requests for clarification can be directed to William A. Gooch, Armor Mechanics Branch, (410) 278-6080.

Accesion For
NTIS CRA&I ☑
DTIC TAB ☐
Unannounced ☐
Justification
By
Distribution /
Availability Codes
Dist | Avail and / or Special
A-1

INTENTIONALLY LEFT BLANK.

TABLE OF CONTENTS

		Page
	PREFACE	iii
	LIST OF FIGURES	vii
	LIST OF TABLES	xiii
1.	INTRODUCTION	1
	PART I. EXPERIMENTS WITH GLASSES	3
2.	EXPERIMENTAL SET-UP	5
3.	CHARACTERIZATION OF THE TARGET MATERIALS	5
4.	DAMAGE PHENOMENOLOGY	7
5.	WAVE PROPAGATION IN PLATES	12
6.	THE DAMAGE VELOCITY CONCEPT	14
7.	DAMAGE VELOCITIES AND NUCLEATION THRESHOLDS	16
7.1	Experimental Results	16
7.2	Crack Velocities	21
7.3	Discussion of the Damage Velocities	22
8.	INFLUENCE OF SPECIMEN GEOMETRY	24
8.1	Lateral Dimensions	24
8.2	Influence of Plate Thickness	24
9.	EXPERIMENTS WITH BLOCKS OF K5	29
10.	FAILURE WAVES	41
10.1	Review of Work on Failure Waves	41
10.2	Plate Impact Tests on K5 Glass	42
10.3	Discussion	44
11.	SUMMARY OF THE RESULTS WITH GLASSES	45

PART II. EXPERIMENTS WITH CERAMICS 47

12. COMPILATION OF THE EXPERIMENTS 49

13. MATERIAL PROPERTIES 51

14. DESCRIPTION AND EVALUATION OF DAMAGE 53

14.1 Experiments with SiC 53
14.2 Experiments with TiB_2 80
14.3 Experiments with Alumina (Al_2O_3 101

15. CLASSIFICATION OF DAMAGE 107

16. ANALYSIS OF FRACTURE VELOCITIES 110

17. MICROSTRUCTURAL ANALYSIS 112

18. DUAL SIDE HIGH-SPEED PHOTOGRAPHY 113

19. SUMMARY OF THE RESULTS WITH CERAMICS 123

ACKNOWLEDGEMENT 125

20. REFERENCES 127

DISTRIBUTION LIST 129

LIST OF FIGURES

Figure		Page
2.1	Schematic of experimental configuration	5
4.1	Schematic of crack types	7
4.2	Float glass specimen 30.5 μs after impact of a steel cylinder (D = 30 mm)	7
4.3	Photographs of a float glass plate after impact at v_p = 48 m/s (shot no. 10286)	9
4.4	Photographs of a float glass plate impacted at v_p = 40 m/s (shot no. 10266)	10
4.5	Photographs of a float glass plate impacted at v_p = 220 m/s (shot no. 10013)	11
5.1	Schematic of wave and crack propagation in a plate caused by edge-on impact (side view)	12
5.2	Schematic of wave propagation in a plate caused by edge-on impact (top view)	13
6.1	Path-time plot of shot no. 10286 (see Figure 4.3)	15
7.1	Damage velocities v_p versus momentum flux E-A for float glass and the optical glasses K5, F6, and SF6	17
7.2	a) SF6 plate 21.5 μs after impact, v_p = 60 m/s (shot no. 10054) b) Corresponding path-time curve	23 23
7.3	a) SF6 plate 21.9 μs after impact, v_p = 450 m/s (shot no. 10045) b) Corresponding path-time curve	23 23
8.1	Schematic of wave propagation in a plate caused by impact	24
8.2	V_D versus around the nucleation threshold for K5 plates of different thicknesses	28

Figure		Page
8.3	V_D – E-A curve around the nucleation threshold for K5 plates of different thicknesses	28
9.1	High-speed photographs of a K5 block of 100 mm thickness, v_P = 90 m/s, shot no. 10259	30
9.2	Different views of the impacted K5 block (shot no. 10259) a) overview; b) top view; c) side view	31
9.3	Complete series of high-speed photographs of a 100 mm thick K5 block impacted at v_P = 1040 m/s (shot no. 10327); frame rate 1 MHz (impact directed from right to left)	34
9.4	Enlargements of the photographs no. 10 and no. 15 of shot no. 10327 (impact direction from left to right)	35
9.5	Path-time plot of shot no. 10327	35
9.6	Schematic of the experimental configuration for simultaneous side view and top view high-speed photography	36
9.7a	Complete series of high-speed photographs of a K5 block (200 mm × 150 mm × 100 mm) impacted at 416 m/s; side view (shot no. 10697)	37
9.7b	Complete series of top view photographs of shot no. 10697	38
9.8	Path-time plot of shot no. 10697	39
9.9a	Shot no. 10697, photograph no. 13, side view, 25 µs after impact	40
9.9b	Shot no. 10697, photograph no. 13, top view, 25 µs after impact	40
10.1	Free surface velocity versus time from plate impact experiment Gla296 on K5 glass, performed by H. Nahme and coworkers (EMI, Freiburg)	43
10.2	Distance-time plot of the plate impact experiment Gla296	43
13.1	Micrographs of the different ceramics in the initial state	52
14.1	High-speed photographs of shot no. 10105	54

Figure		Page
14.2	Path-time plots of shot no. 1010555	55
14.3	Reassembled specimen of shot no. 10105	55
14.4	Reassembled specimen of shot no. 10111	56
14.5	Fracture surface which changes from smooth (sharp edges) to rough (fuzzy edges) of shot no. 10111	56
14.6	High-speed photographs of shot no. 10111	57
14.7	Path-time plots of shot no. 10111	58
14.8	High-speed photographs of shot no. 10107	59
14.9	Reassembled specimen of shot no. 10107	60
14.10	Path-time plots of shot no. 10107	61
14.11	High-speed photographs of shot no. 10118	63
14.12	Path-time plots of shot no. 10118	65
14.13	Path-time plots of the main fractures R1, R2, R3, and the secondary cracks	66
14.14	High-speed photographs of shot no. 10137	67
14.15	Path-time plots of shot no. 10325	69
14.16	High-speed photographs of shot no. 10325	70
14.17	High-speed photographs of shot no. 10116	73
14.18	High-speed photographs of shot no. 10359	74
14.19	High-speed photographs of shot no. 10362	75
14.20	Path-time plot of shot no. 10116	76
14.21	Path-time plot of shot no. 10359	76
14.22	Path-time plot of shot no. 10362	76

Figure | Page

14.23 Path-time plot of shot no. 10142 77

14.24 Path-time plot of shot no. 10147 77

14.25 High-speed photographs of shot no. 10142 78

14.26 High-speed photographs of shot no. 10147 79

14.27 High-speed photographs of shot no. 10108 81

14.28 High-speed photographs of shot no. 10110 82

14.29 High-speed photographs of shot no. 10130 83

14.30 Reassembled specimen of shot no. 10108 84

14.31 Reassembled specimen of shot no. 10110 84

14.32 Reassembled specimen of shot no. 10130 85

14.33 Shot no. 10108 85

14.34 Shot no. 10110 85

14.35 Path-time plots of shot no. 10130 85

14.36 High-speed photographs of shot no. 10119 87

14.37 High-speed photographs of shot no. 10109 88

14.38 High-speed photographs of shot no. 10326 89

14.39 Reassembled specimen of shot no. 10119 90

14.40 Reassembled specimen of shot no. 10109 90

14.41 Shot no. 10119 91

14.42 Shot no. 10326 91

14.43 Path-time plots of shot no. 10109 91

14.44 High-speed photographs of shot no. 10136 92

Figure		Page
14.45	Path-time plot of shot no. 10136	93
14.46	Photograph of two fragments of the specimen from shot no. 10136	93
14.47	High-speed photographs of shot no. 10117	95
14.48	High-speed photographs of shot no. 10360	96
14.49	High-speed photographs of shot no. 10367	97
14.50	High-speed photographs of shot no. 10143	98
14.51	Path-time plot of shot no. 10117	99
14.52	Path-time plot of shot no. 10360	99
14.53	Path-time plot of shot no. 10367	99
14.54	Path-time plot of shot no. 10143	100
14.55	Photograph of two fragments of shot no. 10143	100
14.56	Fragments of 5 mm thickness from shot no. 10143 (scale in cm)	100
14.57	High-speed photograph of shot no. 10366	102
14.58	High-speed photograph of shot no. 10132	103
14.59	Path-time plot of shot no. 10366	104
14.60	Path-time plot of shot no. 10132	104
14.61	High-speed photographs of shot no. 10134	105
14.62	High-speed photograph of shot no. 10135	106
14.63	Path-time plot of shot no. 10134	107
14.64	Path-time plot of shot no. 10135	107
15.1	Schematic representation of the observed types with SiC and Al_2O_3 (a) and TiB_2 (b)	108

Figure		Page
15.2	SiC at a) v_P = 150 m/s, t = 10.5 μs, b) v_P = 185 m/s, t = 4.6 μs	108
15.3	TiB_2, v_P = 85 m/s, t = 5.3 μs	109
15.4	Al_2O_3, v_P = 85 m/s, t = 9.7 μs	109
15.5	SiC, v_P = 513 m/s, t = 4.6 μs (a) and TiB_2, v_P = 564 m/s, t = 4.5 μs (b)	109
15.6	TiB_2, v_P = 784 m/s, t = 6.2 μs, shot no. 10143	110
16.1	Damage velocity versus impact velocity for (a) SiC, (b) TiB_2, and (c) Al_2O_3 (CeramTech A 1898)	111
17.1	Micrographs of impacted ceramics a) TiB_2, v_P = 784 m/s, (b) SiC, v_P = 1040 m/s	113
18.1	Experimental configuration for dual-side high-speed photography	113
18.2	Comparison of three high-speed photographs from both sides of a SiC specimen, shot no. 10517, = 66 m/s	115
18.3	Comparison of three high-speed photographs from both sides of a SiC specimen, shot no. 10551, = 202 m/s, Δt = 1 μs	116
18.4a	Complete series of high-speed photographs of shot no. 10600, left side, Δt = 1 μs	117
18.4b	Complete series of high-speed photographs of shot no. 10600, right side, Δt = 1 μs	118
18.5	Reassembled specimen of shot no. 10600 a) left side, b) right side	120
18.6	Fracture surface normal to the impacted edge of the specimen (visible in the upper part of the micrograph)	121
18.7	Micrograph of the fracture surface near the impacted edge	121
18.8	Micrographs of the fracture surface at different distances from the impacted edge, a) 300 μm, b) 1 mm, c) 2 mm	122

LIST OF TABLES

Table		Page
3.1	Composition of Glass Target Material	6
3.2	Physical Properties	6
5.1	List of the Measured Values of C_L and D and Calculated Data (on the Basis of C_L and D) of μ and C_T	14
7.1	Experiments With Float Glass	18
7.2	Experiments With K5	18
7.3	Experiments With F6	19
7.4	Experiments With SF6	19
7.5	Impact Velocities and Initial Pressures at the Nucleation Threshold	20
7.6	Mean Values of the Measured Crack Velocities	21
8.1	Results With K5 Plates of the Thickness d = 8 mm	26
8.2	Results With K5 Plates of the Thickness d = 17 mm	26
8.3	Results With K5 Plates of the Thickness d = 20 mm	27
8.4	Results With K5 Plates of the Thickness d = 28 mm	27
8.5	Results With K5 Plates of the Thickness d = 40 mm	27
8.6	Crack and Damage Velocities at the Nucleation Threshold With K5 Plates of Different Thicknesses	29
12.1	Experiments With SiC	50
12.2	Experiments With TiB_2	50
12.3	Experiments With Al_2O_3 (CeramTech A 1898)	51
13.1	Physical and Mechanical Properties of the Ceramics	51

INTENTIONALLY LEFT BLANK.

1. Introduction

The interest in ceramic materials for armour applications has increased during the last two decades because it was and still is necessary to reduce the weight of armours for vehicles and in particular for aircrafts. Testing methods have been developed to establish a ballistic performance ranking of the different armour ceramics [1,2], and many composite armours exist which are designed to defeat specific threats. But testing the performance of structures mostly does not reveal the mechanisms that determine the protective strength because of the large number of geometric and material parameters. Starting from this situation two complementary research programs were initiated. Terminal ballistic experiments are conducted with laminated steel targets, laminated ceramic targets and combined targets (steel-ceramics-steel) at the Ernst-Mach-Institut (EMI) and at the Army Research Laboratory (ARL) with identical target and projectile materials. On the other hand, the failure mechanisms due to impact loading of the non-metallic component (glass or ceramics) itself is investigated. The experiments and results of this work are reported here. The aim of the investigations is to achieve more knowledge about how the ceramics is destroyed and comminuted by fracture processes and how the interaction between the fragments themselves or with the confining metal plates influences the penetration or perforation process. The answers to these questions are of importance with respect to the further development of models that describe brittle fracture and penetration processes.

In most of the experimental techniques used in terminal ballistics the important quantities (e. g., depth of penetration, residual velocity) are determined after the penetration process is finished. However, earlier impact experiments with glass and ceramics [3,4] demonstrated that the destruction of these materials starts together with the propagation of the stress waves. In the investigation presented here damage processes during so-called edge-on impact experiments were visualized by means of a Cranz-Schardin high-speed camera in order to study the relation between fracture and wave propagation before the projectile penetrates the target more than a few millimeters. Particularly, the damage phenomenology is considered in this work and the propagation velocities of different types of fracture are analyzed.

The experiments and results with glass (float glass and three optical glasses) are described in Part I, Chapters 2 to 11. Part II, Chapters 12 to 19, is dealing with the experiments and results with ceramics (Al_2O_3, TiB_2 and SiC). The experiments with sapphire are described and analyzed in a separate report (Experiments on Sapphire) prepared by S. Winkler [5].

INTENTIONALLY LEFT BLANK.

Part I.

Experiments with Glasses

INTENTIONALLY LEFT BLANK.

2. Experimental Setup

Figure 2.1 shows a schematic representation of the experimental setup for impact loading of the glass targets. The projectile hits the edge of the specimen. The destruction of the specimen is observed by means of a Cranz-Schardin camera in a shadow-optical arrangement. The impact velocity v_P was varied in the range from 20 m/s to 1000 m/s. In the velocity range below 350 m/s a gas gun was used to accelerate the projectiles. Higher impact velocities were achieved by the use of powder guns. The specimens were positioned at a distance of 10 mm in front of the gun muzzle so that the rear part of the projectile was still guided during impact. The impact velocity was measured by means of two infrared light barriers which are installed in the barrel at distances of 220 mm and 250 mm from the muzzle. With the experiments at high impact velocities the specimen were positioned a few meters away from the muzzle of the powder gun.

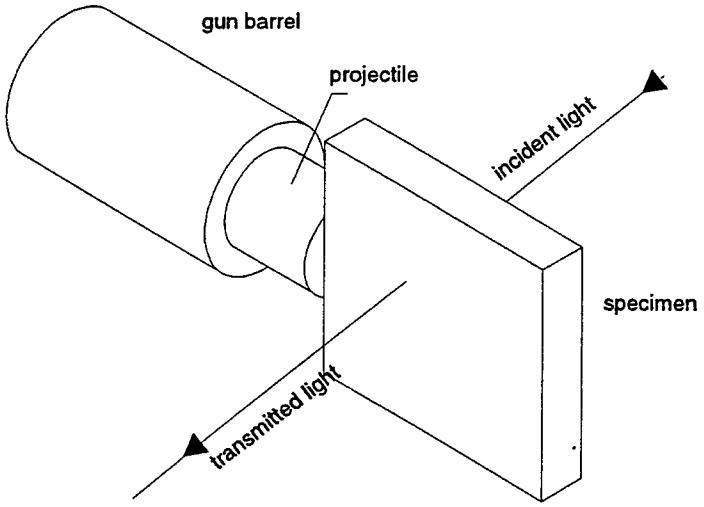


Figure 2.1 Schematic of experimental configuration

3. Characterization of the Target Materials

Float glass and three optical glasses (K5, F6 and SF6) from SCHOTT Company were used as target materials. The chemical composition and the physical properties of the different types of glass are listed in Tables 3.1 and 3.2. The density of the glasses varies in the range from 2.5 g/cm^3 with float glass to 5.28 g/cm^3 with SF6. The sound velocity and the hardness of the glasses decrease with increasing density. The highest longitudinal wave velocity c_L = 5860 m/s is observed with float glass. SF6 exhibits the lowest wave velocity

with c_L = 3600 m/s. The hardness of the glasses (microhardness, 0.49 N, 10 sec) varies in the range from HV 700 to HV 400.

The value of c_L with float glass results from the measurements of Kerkhof [6]. With the optical glasses c_L was calculated according to the equation

$$c_L = \sqrt{\frac{E}{\rho} \frac{1-\mu}{(1+\mu)(1-2\mu)}}$$

using the data of the density ρ, Young's Modulus E, and the Poisson Ratio μ given by the manufacturer. This relationship between the elastic constants of the material holds for an infinitely extended medium. However, high frequencies (i. e., small wavelengths compared to the thickness of the plate) dominate in a pressure wave generated by impact [7]. Therefore, the equation can be applied in the case of plates, too. This assumption was confirmed by our measurements (see Chapter 5).

Table 3.1 Composition of glass target material

Type	SiO_2	B_2O_3	Na_2O	K_2O	Al_2O_3	CaO	BaO	ZnO	TiO_2	PbO
Float	70		15*		1	12**				
K5	65	≤ 5	≤ 5	15		≤ 5		8	≤ 1	≤ 1
F6	40		≤ 5	≤ 5			≤ 5			45
SF6	25		≤ 1	≤ 1						70

* (Na_2O + K_2O); ** (CaO + MgO)

Table 3.2 Physical properties

Type	Density [g/cm^3]	E-Modulus [10^{3}N/mm^2]	Poisson ratio	HV	Sound speed [m/s]
Float	2.5	--	--	680	5860
K5	2.59	71	0.227	584	5624
F6	3.76	57	0.231	455	4196
SF6	5.18	56	0.248	407	3595

4. Damage Phenomenology

Several different types of fracture and fracture patterns occur when the edge of the glass plate is impacted by a blunt projectile. First of all the cracks which are generated at the impacted area of the edge of the specimen shall be considered. Two types of cracks develop in the impact zone. A high number of single cracks radiates from the center of impact (center of the projectile). These cracks will be denoted radial cracks, the front of their tips primary crack front. The surfaces of the radial cracks are oriented perpendicular to the surface planes of the specimen.

An other type of crack starts with its surface parallel to the surface planes. These cracks slowly approach the surface of the target plate with increasing distance from the impacted edge. Shell-shaped fragments are generated by this process. Figure 4.1 shows a schematic representation of both types of cracks. The high-speed photograph of a float glass plate (Fig. 4.2) gives an example of the two crack types. The front of the shell-shaped cracks appears as a black semicircular line along the tips of the radial cracks on the photograph. This means that the two crack systems were initiated simultaneously and propagated at the same velocity.

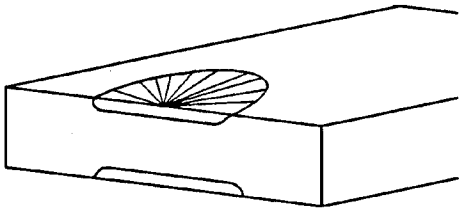


Figure 4.1 Schematic of crack types

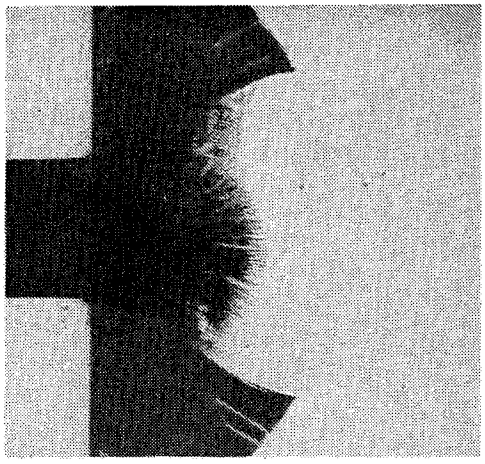


Figure 4.2 Float glass specimen 30.5 μs after impact of a steel cylinder (D = 30 mm)

It was also observed that the primary cracks form a planar front, i. e., cracks have been generated simultaneously on the whole contact area between projectile and target. This case is illustrated by six selected high-speed photographs of a float glass plate which show the specimen in the time interval from 8.8 μs to 18.7 μs after impact at 48 m/s (Fig. 4.3). In this experiment, the fronts of the radial cracks and the shell-shaped fracture coincide, too.

A significantly different fracture pattern is observed when the projectile hits the specimen with a small yaw. The fracture pattern in a float glass plate after impact of a projectile at a yaw angle of 1.2 mrad (in a plane parallel to the surface of the plate) is shown in Figure 4.4. Radial cracks and shell-shaped cracks are generated at the impact site of the edge of the projectile and within and beyond the contact zone. With all the experiments the impacted edges of the plates were polished to avoid different fracture patterns due to the roughness of the impacted surface.

The photographs in Figures 4.3 and 4.4 additionally show cracks which were initiated at the edge of the glass plate above and below the projectile.

The cracks start from the edge of the specimen in a direction normal to it and then change their direction of propagation so that an angle of about 30° is included between the cracks and the shot line. The spaces between these cracks are irregular. All these cracks grow with constant velocity v_C and will be denoted secondary cracks in the following. The secondary cracks are initiated successively by the shear wave which is generated at the edge of the projectile. Therefore, the secondary crack system exhibits a triangular shape. The secondary crack zones expand with transversal wave velocity c_T.

The Figures 4.3 to 4.5 show a further damage mechanism. Crack centers are initiated between the first compressive wave and the primary crack front. Inhomogeneities, flaws, impurities or existing microcracks may turn into initial points or nucleation points of cracks which propagate in all directions. These cracks and not the nucleation points or nuclei are visualized by the high-speed photography, but to simplify discussions the designations "crack center" and "nucleus" are used synonymously. In the first stage of development the centers are shaped like ellipsoids whose major axis is directed towards the impact center or the impact site of the edge of the projectile.

At high impact velocities no details can be recognized in the impact zone. Figure 4.5 shows an example where a float glass plate was impacted at 220 m/s. Only a black area is seen in front of the projectile. The light is deflected by the high density of primary cracks, shell-shaped fracture, crack centers and the stress waves in this zone.

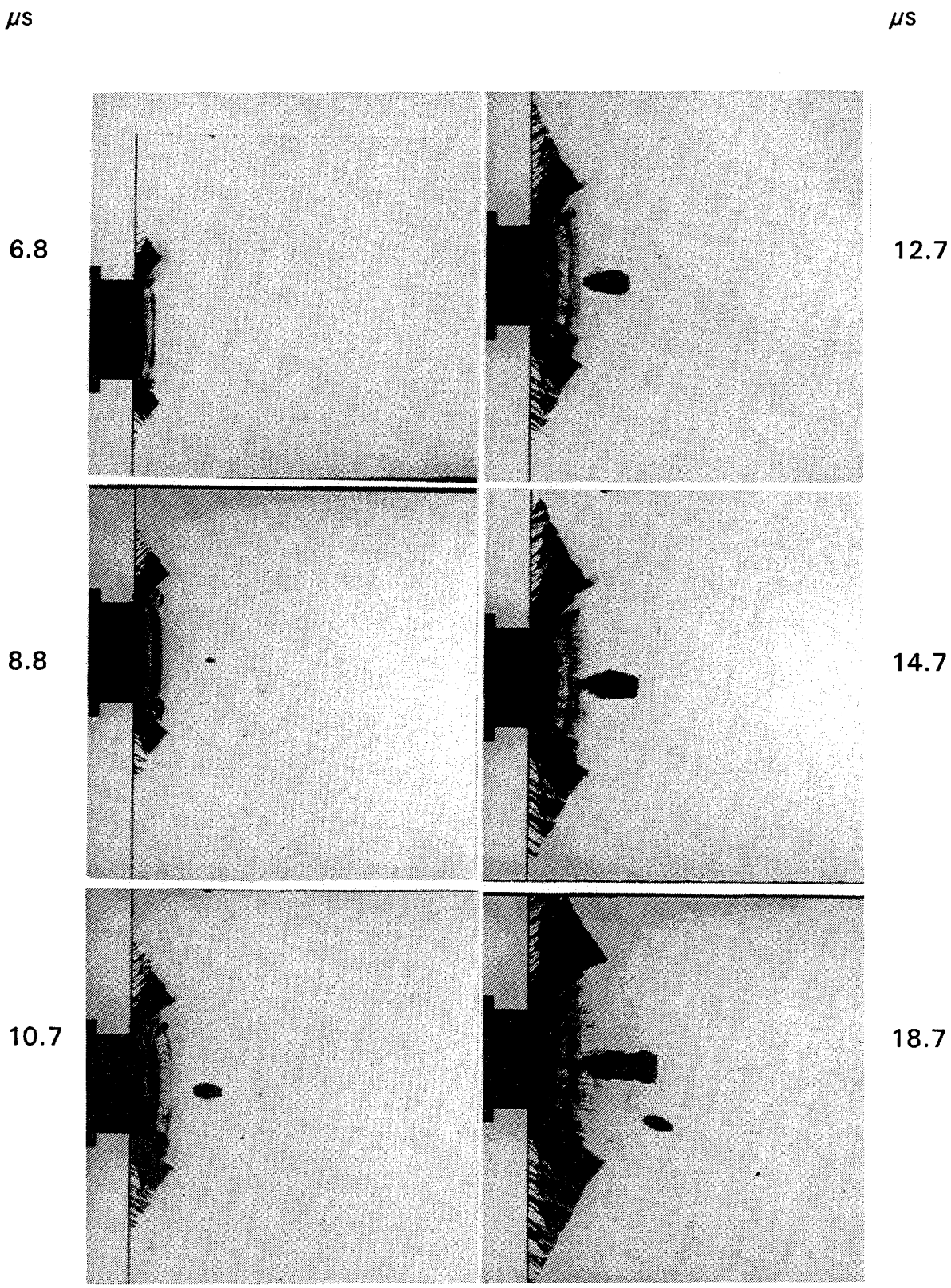


Figure 4.3 Photographs of a float glass plate after impact at v_P = 48 m/s (shot no. 10286)

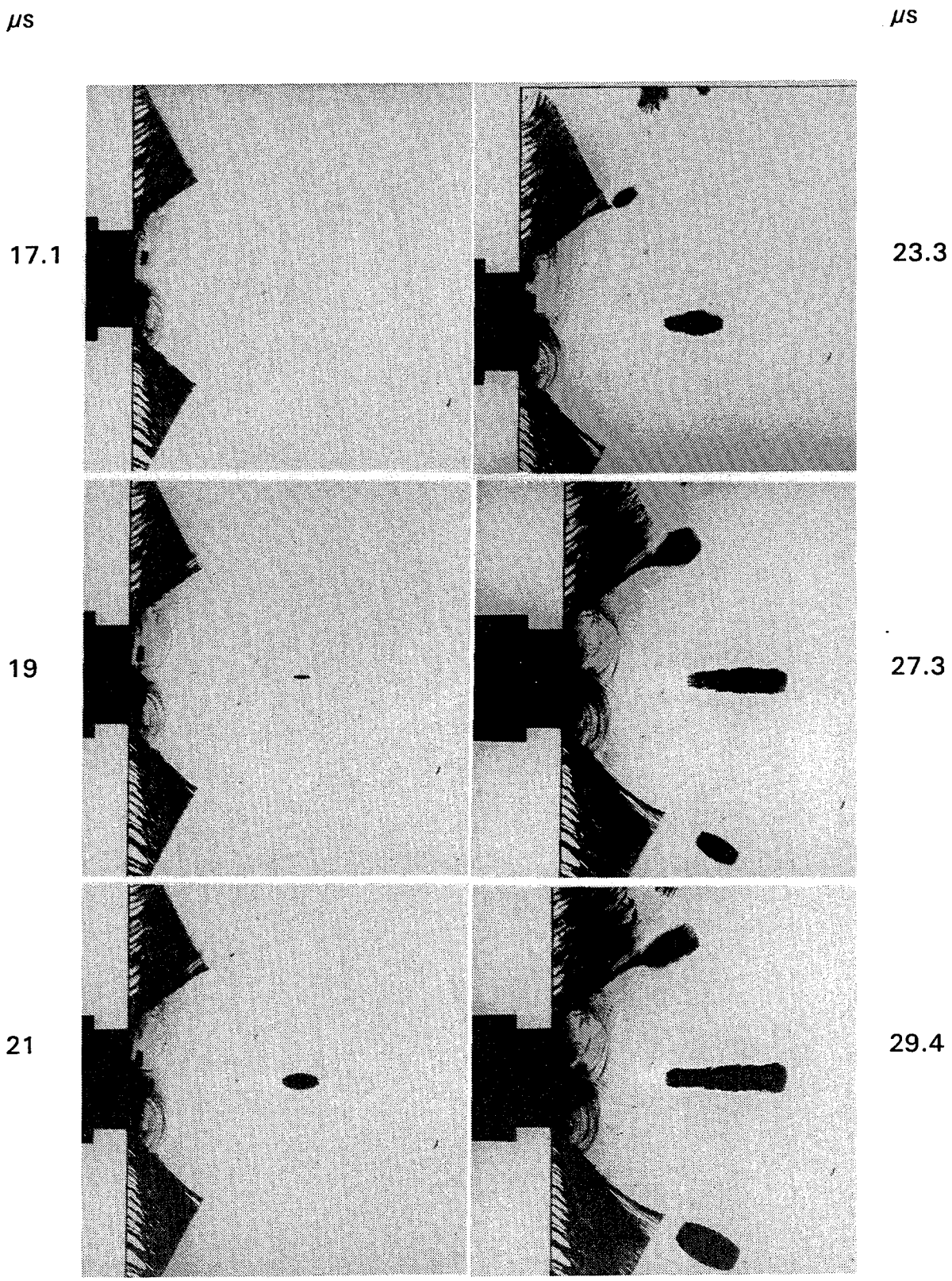


Figure 4.4 Photographs of a float glass plate impacted at v_P = 40 m/s (shot no. 10266)

μs

μs

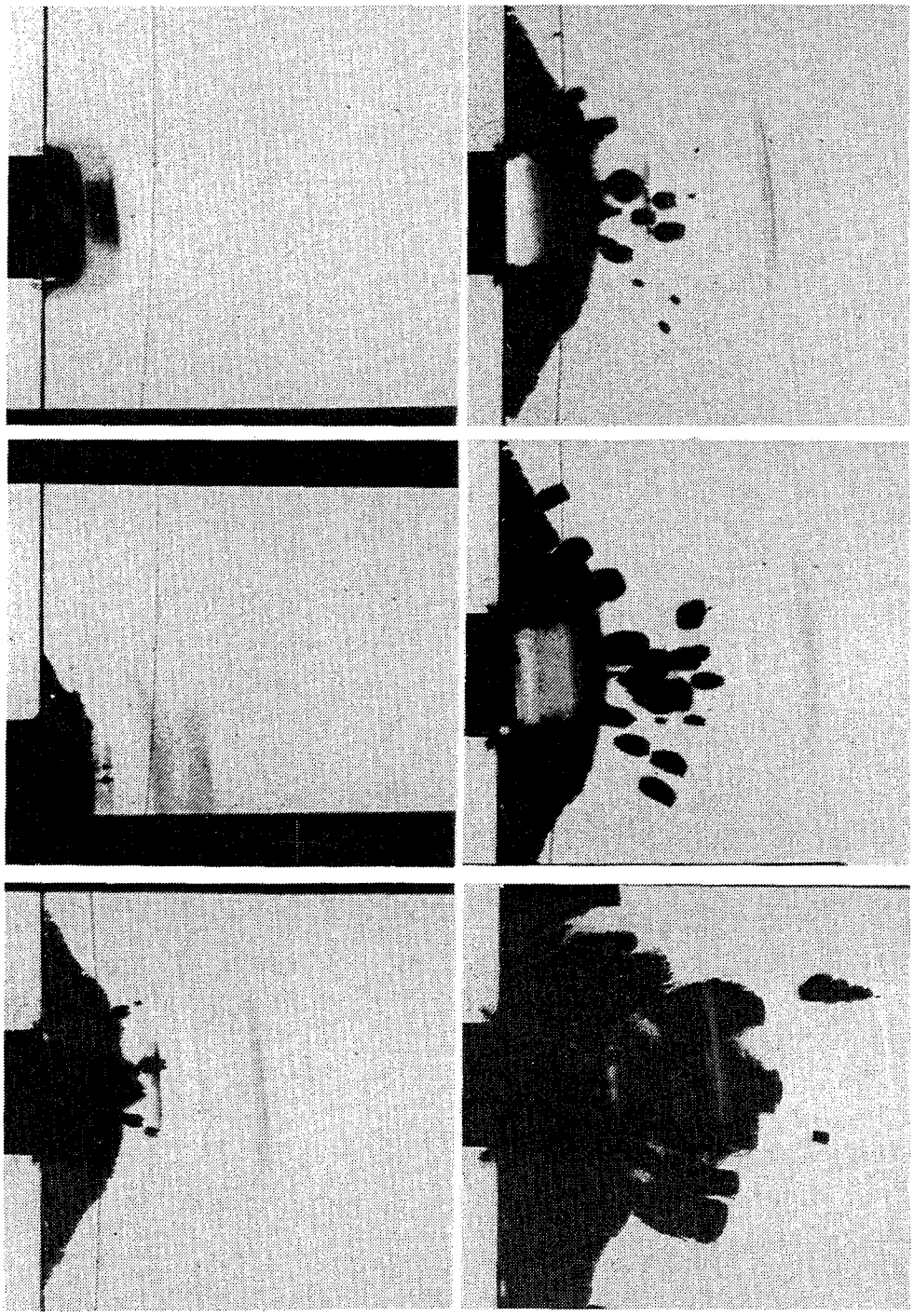


Figure 4.5 Photographs of a float glass plate impacted at v_P = 220 m/s (shot no. 10013)

5. Wave Propagation in Plates

Figure 5.1 shows a schematic representation of the wave and crack propagation in a glass plate after impact of a pointed projectile. The longitudinal wave which propagates at the velocity c_L is followed by the transversal wave (shear wave) at the velocity c_T, which is about 60 % of c_L with glasses. Another transversal wave is generated by the reflection of the longitudinal wave at the impacted edge. This wave includes an angle

$$\alpha = \arcsin \frac{c_T}{c_L}$$

with the edge of the plate. The primary fracture front forms a semicircle with radius $v_C \cdot t$ whereas the tips of the secondary crack zones are situated at $c_T \cdot t$. The secondary fracture fronts include an angle

$$\beta \approx \arcsin \frac{v_C}{c_T}$$

with the edge of the plate. To establish this relation we neglect that the secondary cracks start normal to the edge and it is assumed that the cracks grow nearly perpendicular to the fronts CJ and KB.

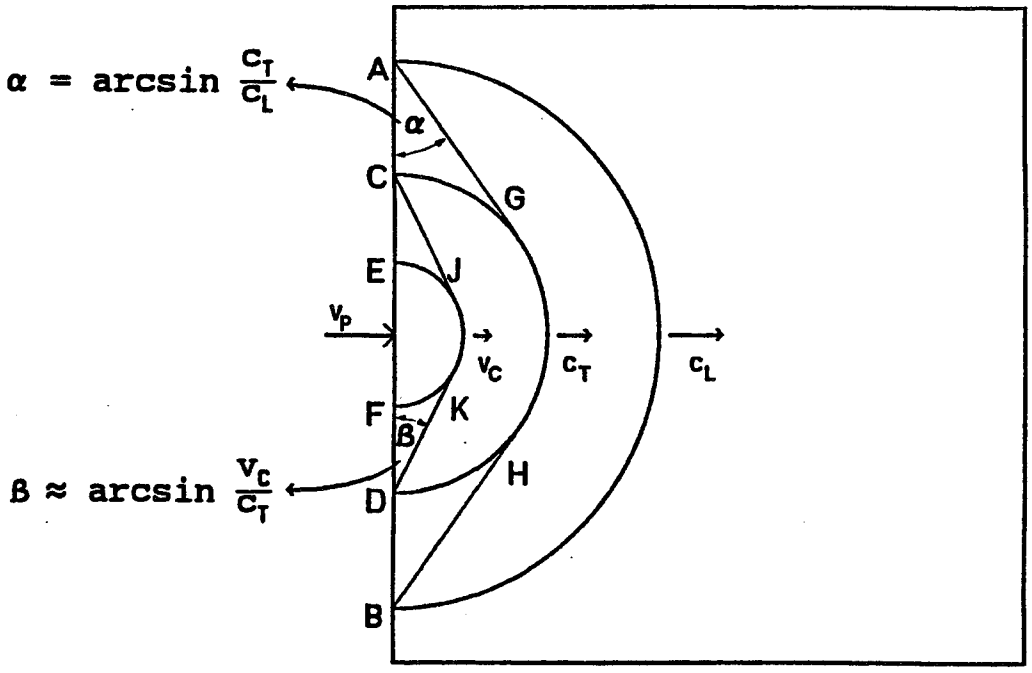


Figure 5.1 Schematic of wave and crack propagation in a plate caused by edge-on impact (side view)

When the specimen is impacted by a blunt cylinder, two shear waves are generated, one at the upper edge and one at the lower edge of the projectile. Planar wave fronts are formed ahead of the projectile. The fracture propagation in this case was described in Chapter 4.

Many of the high-speed photographs (see for example Fig. 4.5) show that several wave fronts propagate in the specimens which succeed one another at the same distance D. This effect is due to the finite thickness d of the plates and was described by Schardin [8] and quantitatively analyzed by means of the Schlieren-optical technique by Vollkommer [9] and Beinert [10]. Figure 5.2 shows a schematic representation of the impact situation and the generated waves in a top view.

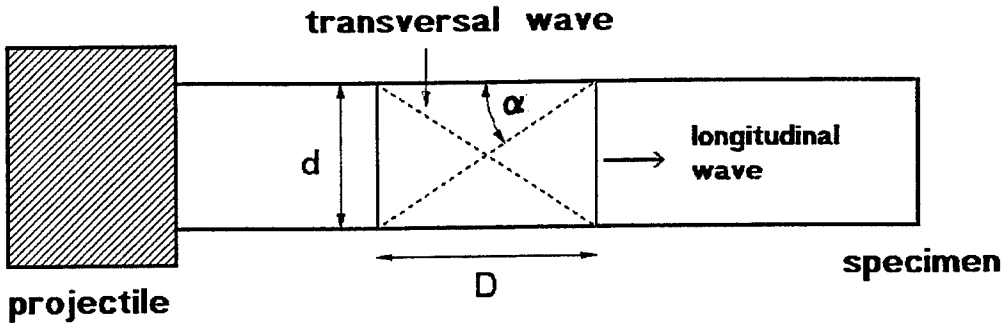


Figure 5.2 Schematic of wave propagation in a plate caused by edge-on impact (top view)

The compressive wave also displaces the particles at the surfaces of the plate perpendicular to its direction of propagation so that a transversal wave is generated which includes an angle $\alpha = \arcsin(c_T/c_L)$ with the surface. When this transversal wave is reflected at the opposite surface of the plate a transversal and again a longitudinal wave are generated. In this way a sequence of equidistant pressure pulses is formed by a sequence of reflections. It can be recognized from Figure 5.2 that $\tan\alpha = d/D$. From this follows the relation between the thickness of the plate d and the distance between the pressure pulse D.

$$D = d\sqrt{\left(\frac{c_L}{c_T}\right)^2 - 1} = \frac{d}{\sqrt{1-2\mu}}$$

The mean values of the measured wave velocities c_L and the measured distances D are listed in Table 5.1 together with the calculated values of the Poisson ratios and the transversal wave velocities. c_T was calculated according to the equation

$$c_T = c_L \sqrt{\frac{1-2\mu}{2(1-\mu)}} \quad .$$

Table 5.1 List of the measured values of c_L and D and calculated data (on the basis of c_L and D) of μ and c_T

Material	c_L [m/s]	D [mm]	μ	c_T [m/s]
Float glass	5890	13.1	0.210	3570
K5	5750	10.8	0.226	3420
F6	4230	14.3	0.255	2430
SF6	3590	14.2	0.253	2060

6. The Damage Velocity Concept

The concept of damage velocity is introduced to describe the different damage processes quantitatively. The path-time curves of the primary crack front and of the cracks, which start from the nuclei in and against the direction of the shock wave, are determined. At the high dynamic loadings considered in these investigations all cracks propagate with their maximum (terminal) velocity v_C, which is a characteristic quantity for each type of glass (see Chapter 7.2). Therefore, the path-time curves are all straight lines. The intersection points of those straight lines, which describe the cracks starting from the nucleation points, determine the places "s" and times "t" of nucleation. The slope of the line through the nucleation points (s,t) is defined as the damage velocity v_D.

Figure 6.1 shows the evaluation of the experiment presented in Figure 4.3. The filled triangles represent the position of the tip of the upper secondary fracture zone. The open triangles and squares represent the fore and rear front of the observed crack centers. One recognizes that the first point of nucleation is localized on the line which describes the lateral expansion of the secondary crack zone. That means, the damage velocity v_D equals the velocity v_{SR} = 3030 m/s at which the secondary cracks are initiated along the edge of the specimen.

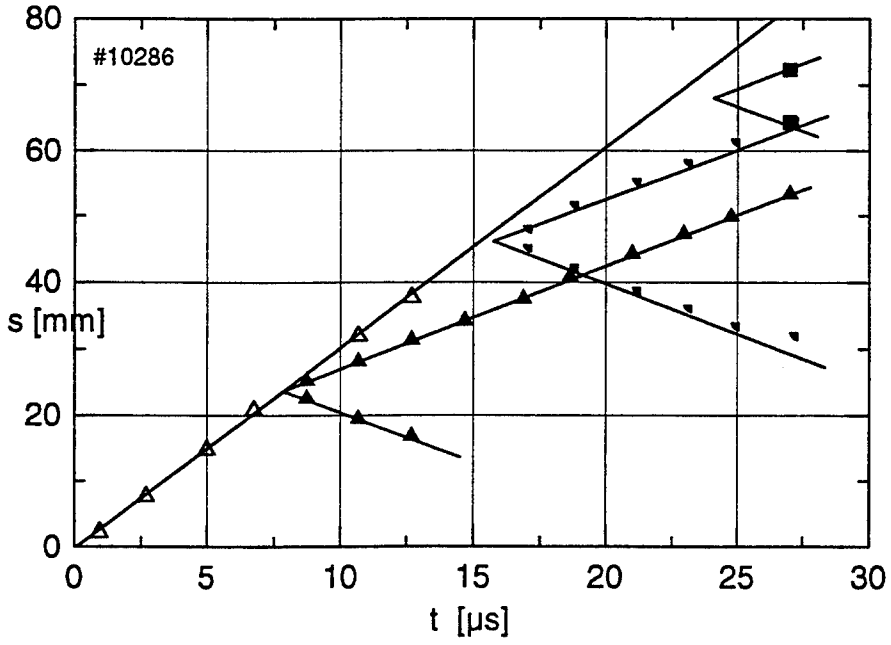


Figure 6.1 Path-time plot of shot no. 10286 (see Fig. 4.3)

7. Damage Velocities and Nucleation Thresholds

All specimens of the optical glasses used in the experiments described in this Chapter had the dimensions 100 mm x 100 mm x 10 mm. The lateral dimensions of the float glass specimen ranged from 100 mm x 100 mm to 180 mm x 180 mm, their thickness was 10 mm, too. In order to establish the same impact conditions and to be able to compare the results directly, only steel cylinders with 30 mm diameter and 23 mm length were used as projectiles.

7.1 Experimental Results

The measured crack, damage and wave velocities of the different glasses are listed in Tables 7.1 to 7.4 together with the corresponding impact velocities. The tables also include the values of the product E·A, where E is the energy density (energy per unit volume that is transferred to the target material by the shock wave) and A is the area of contact between the target and the projectile. The physical unit of this quantity is Newton. Therefore, E·A is interpreted as momentum flux (momentum that is transferred to the target by the shock wave per unit time via the contact area). The energy density E is determined by the acoustic impedances $Z_T = \rho_T \cdot c_{L,T}$ of the target material and the projectile material $Z_P = \rho_P \cdot c_{L,P}$.

$$E = \frac{Z_T \cdot Z_P^2}{(Z_T + Z_P)^2} \cdot \frac{v_P^2}{c_{L,T}}$$

ρ_T and ρ_P are the densities, $c_{L,T}$ and $c_{L,P}$ the longitudinal wave velocities of the target and projectile material.

A representation of the experimental results which is independent of the caliber is achieved when the crack and damage velocities are plotted versus the momentum flux E·A. This was demonstrated in [11].

The damage velocities observed with the four glasses are plotted in v_D-E·A curves in Figure 7.1.

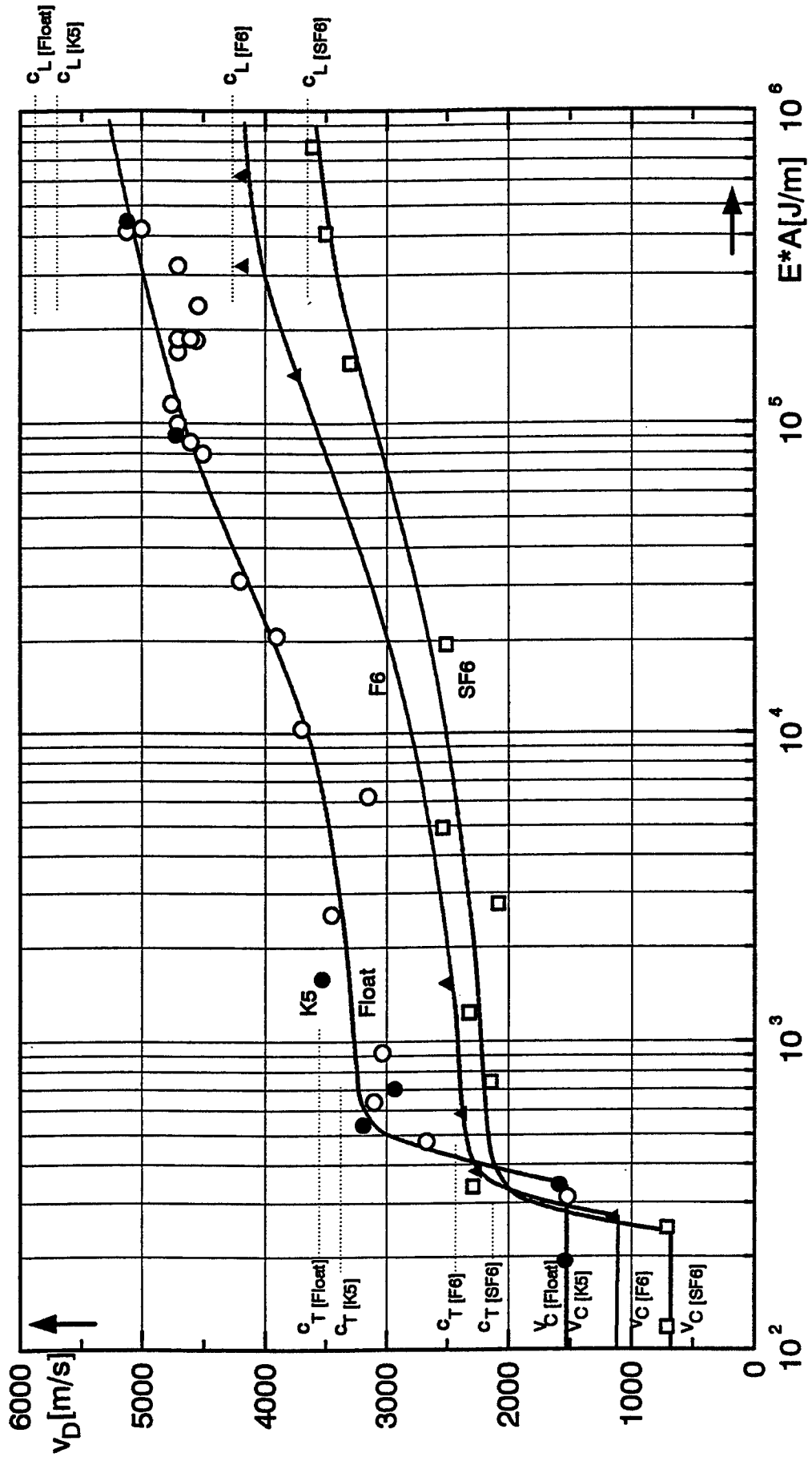


Figure 7.1 Damage velocities v_D versus momentum flux E·A for float glass and the optical glasses K5, F6 and SF6

Table 7.1 Experiments with float glass

Shot No.	v_P [m/s]	E·A [N]	c_L [m/s]	v_C [m/s]	v_D [m/s]
10033	28	314		1520	
10285	34	478		1540	2670
				1550	
10266	40	640	5870	1520	3100
				1570	
10286	48	922		1550	3030
				1610	
10018	122	6252			3070
10014	157	10353			3700
10013	222	20700			3900
10047	455	86950	5790		4600
10049	755	239411	5820		4540
10029	990	411642	5970		5120
10031	1000	420000	6000		

Table 7.2 Experiments with K5

Shot No.	v_P [m/s]	E·A [N]	c_L [m/s]	v_C [m/s]	v_D [m/s]
10050	21	194		1544	
				1543	
10101	28	345		1590	
10061	35	539		1530	3190
				1560	
10282	40	704			2930
10062	60	1584			3530
10051	456	91492	5700		4720
10036	1005	444411	5800		5120

Table 7.3 Experiments with F6

Shot No.	v_P [m/s]	E·A [N]	c_L [m/s]	v_C [m/s]	v_D [m/s]
10048	21	269		1162	
				1114	
10059	25	381		1120	2270
10056	31	586			2390
10041	50	1525	4240	1050	2520
				1150	
				1000	
10023	80	3904	4200	1130	2130
				1100	
10055	484	142896	4160		3760
10040	725	320631	4310		4190
10034	1010	622261	4230		4200

Table 7.4 Experiments with SF6

Shot No.	v_P [m/s]	E·A [N]	c_L [m/s]	v_C [m/s]	v_D [m/s]
10102	18	249		710	
10046	21	340		740	2290
				650	
10060	31	740	3480	750	2140
				650	
10057	40	1232	3480		2320
10054	60	2772	3600		2080
10020	80	4928	3560		2540
10016	159	19466	3650		2510
10045	450	155925	3580		3300
10038	727	406967	3740		3500
10032	1006	770000	3640		3610

The experimental curves show similar courses for all types of glass. At low loadings the specimen are destroyed by the primary and secondary cracks which start from the impacted edge. In this case the damage velocity equals the terminal crack velocity v_C, which is a characteristic quantity of the different types of glass. The damage velocity rises to the order of magnitude of the transversal wave velocity c_T when nucleation occurs. At first, a further increase of the loading results in a slow increase of v_D. With very high loadings v_D approaches the longitudinal wave velocity asymptotically. In the loading range where v_D increases slowly, an augmentation of the number of activated nuclei is observed. It is remarkable that the thresholds where nucleation occurs do not differ significantly from one another in spite of the differences in the physical properties. The results with K5 and float glass are represented by one curve only because it was not possible to make a distinction from the values measured. The float glass data in Figure 7.1 are supplemented by the results of experiments at high impact velocities with projectiles of different calibers.

Table 7.5 shows a list of the lowest impact velocities v_P and the corresponding initial intensities P of the pressure waves where nucleation occurred. The pressures are calculated according to the equation

$$P = \frac{Z_P \cdot Z_T}{Z_P + Z_T} v_P \quad .$$

Table 7.5 Impact velocities and initial pressures at the nucleation threshold

Material	v_P [m/s]	p [MPa]
Float glass	34	379
K5	35	388
F6	25	294
SF6	21	278

7.2 Crack Velocities

In all experiments with glasses only constant crack velocities were observed, independent from the loading. The mean values of the measured crack velocities and the standard deviations are listed together with the ratios of the crack velocities v_C to the transversal wave velocities c_T and to the Rayleigh wave velocities c_R in Table 7.6. The Rayleigh wave velocities were determined with the approximate formula

$$c_R = \frac{0.87 + 1.12 \cdot \mu}{1 + \mu} c_T$$

given by Schardin [7]. According to this relation the Rayleigh wave velocities are approximately 90% of the transversal wave velocity.

Table 7.6 Mean values of the measured crack velocities

Material	v_C [m/s]	v_C/c_T	v_C/c_R
Float glass	1550 ± 31	0.43	0.48
K5	1550 ± 23	0.45	0.49
F6	1100 ± 54	0.45	0.49
SF6	700 ± 48	0.34	0.37

It is remarkable that with float glass and the optical glasses K5 and F6 the ratios of the crack velocities to the wave velocities are nearly equal. The measured crack velocities, which are not only constant but also the maximum (terminal) velocities, are about one half of the corresponding Rayleigh wave velocities. Only the heavy flint glass SF6 exhibits a lower crack velocity.

In the case of float glass the terminal crack velocity was already observed by Christie [12] and Schardin [7]. Yoffe [13] and Craggs [14] developed theories to explain the terminal crack velocity. A review of the investigations and theories on terminal crack velocity was given by Kolsky [15].

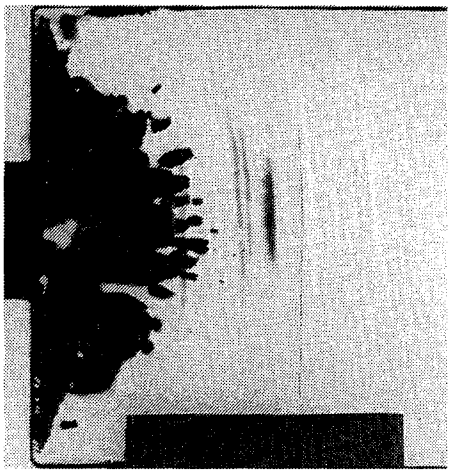
7.3 Discussion of the Damage Velocities

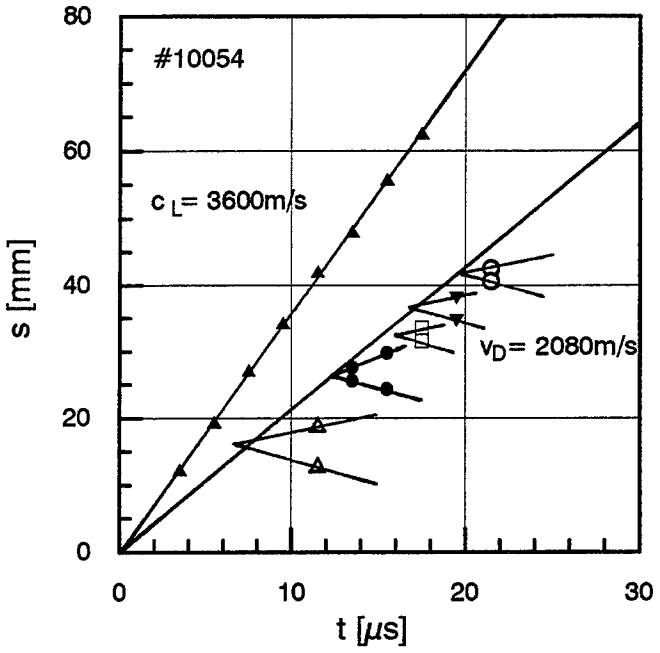
The behavior observed, i. e., the rise of the damage velocity v_D from terminal crack velocity to transversal wave velocity c_T when nucleation occurs and the asymptotic approach of longitudinal wave velocity c_L, can be explained in the following way. All experiments with blunt projectiles have shown that crack formation starts at the impact site of the edge of the projectile. The primary fracture front is always formed with a certain delay compared to the secondary cracks. This can be recognized clearly from the photographs in Figure 4.3. Shear waves are generated at the edge of the projectile whereas the material in front of the projectile is compressed by the longitudinal wave. Cracks are generated first under the influence of shear stresses, i. e., the glasses are more sensitive to shear loading than to compressive loading.

A similar behavior is observed with the crack generation by nucleation. That means nucleation occurs when the intensity of the shear wave exceeds a certain level. The loading range, where on the one hand the amplitude of the transversal wave is high enough to stimulate all the potential nuclei, but on the other hand the intensity of the compressive wave is not sufficiently high to nucleate cracks, corresponds to the plateau in the v_D - E·A diagram with $v_D = c_T$. The high-speed photographs of impacts in this loading range demonstrate that nucleation only occurs in the region which was already passed by the transversal waves.

Figure 7.2 sets an example of an experiment with $v_C \approx c_T$. Figure 7.2a shows an SF6 plate 21.5 μs after impact at $v_P = 60$ m/s. The specimen is destroyed mainly by nucleation. The photograph reveals that the front of the crack centers clearly lags behind the first pressure wave (appears bright in this case). Figure 7.2b shows the corresponding path-time curve. The filled triangles represent the position of the pressure wave, the other symbols indicate the fore and rear fronts of the crack centers. The nucleation points were extrapolated. The slope of the straight line through the nucleation points is 2.08 mm/μs, that means the damage velocity equals transversal wave velocity and crack formation from the nucleation points starts with the arrival of the transversal wave.

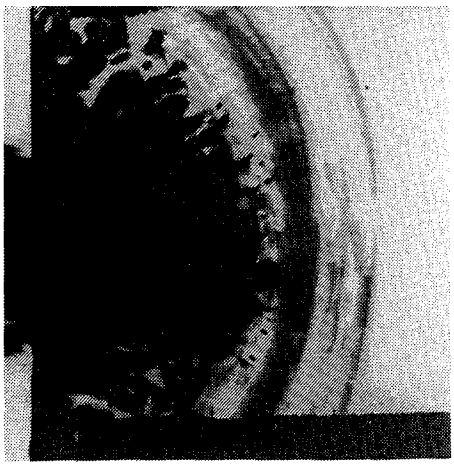
With higher loadings nucleation is already observed in these zones which have only been passed by the pressure wave. Figure 7.3 sets an example of this case. The photograph of an SF6 plate 21.9 μs after impact at $v_P = 450$ m/s is shown in Figure 7.3a, the corresponding path-time curve is plotted in Figure 7.3b. The photograph reveals crack centers close to the second pressure pulse. In the path-time curve the nucleation points range between the two straight lines which represent the pressure wave and the shear wave, i. e., the pressure wave initiates the cracks at the nuclei.

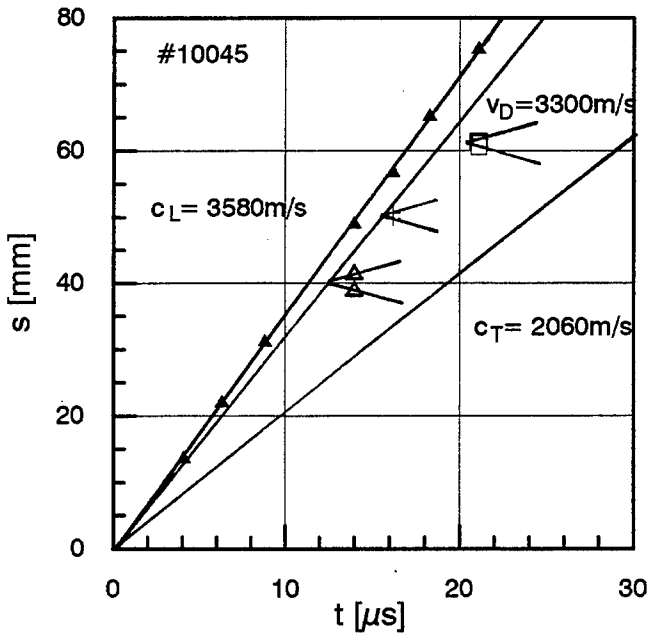




a) b)

Figure 7.2 a) SF6 plate 21.5 μs after impact, v_P = 60 m/s (shot no. 10054)
b) corresponding path-time curve





a) b)

Figure 7.3 a) SF6 plate 21.9 μs after impact, v_P = 450 m/s (shot no. 10045)
b) corresponding path-time curve

8. Influence of Specimen Geometry

8.1 Lateral Dimensions

When the longitudinal wave L is reflected at the upper and lower edge of the target plate a longitudinal wave L' and a transversal wave T' are generated. Figure 8.1 shows a schematic representation of these waves. L is a pressure wave whereas L' is a tensile wave.

The impact experiments have demonstrated that crack centers could be initiated with the arrival of the relief wave L'.

For this reason it is necessary to take into consideration only such nuclei that have been formed under similar or comparable conditions. Therefore, only those crack centers were evaluated which have been generated under the influence of the pressure wave L, the shear waves generated by the impact and the shear waves which lead to the sequence of pressure pulses described in Chapter 5.

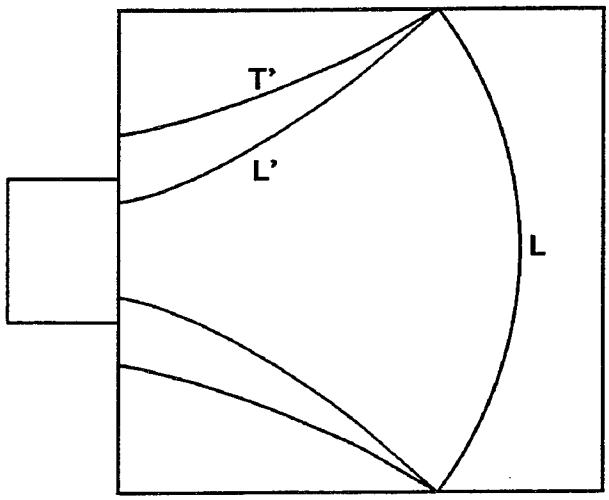


Figure 8.1 Schematic of wave propagation in a plate caused by impact

8.2 Influence of Plate Thickness

The influence of the thickness of the target plates was investigated in impact tests with K5 specimens of the thicknesses d = 8 mm, 17 mm, 28 mm, 40 mm and 100 mm. Steel cylinders with 30 mm diameter and 23 mm length were used in these experiments too. The measured values of the crack, wave, and damage velocities with plate thicknesses up to 40 mm are listed in Tables 8.1 to

8.5. The propagation of the secondary fracture zones could be observed best with the specimens of 8 mm and 17 mm thickness because these plates had the dimensions 200 mm x 150 mm. The results with glass blocks of 100 mm thickness are described in Chapter 9.

The aim of these impact tests was to determine the relationship between the plate thickness and the nucleation threshold. Therefore, most of the experiments were conducted at impact velocities in the range from 20 m/s to 60 m/s.

The impact tests of glass plates of 10 mm thickness with blunt projectiles of different calibers had shown that the nucleation threshold was shifted towards lower impact velocities with increasing caliber [11]. A nucleation threshold could be determined (with respect to the momentum flux E·A) independent of the caliber for one type of glass and one plate thickness. A variation of the plate thickness means also a change of the contact area and therefore of the momentum flux. For this reason we supposed that in case of different calibers a nucleation threshold could be determined which is independent of the plate thickness, too. This hypothesis was not confirmed by the experiments.

The measured damage velocities v_D are plotted versus the impact velocity v_P in Figure 8.2. A correlation between plate thickness and the impact velocity where nucleation occurs cannot be derived from these data. The nucleation thresholds with respect to v_P are close together with plate thicknesses of 20 mm, 28 mm and 40 mm in spite of the different impact geometries in these cases. With plates of 20 mm thickness the diameter of the projectile D is bigger than the plate thickness d, with plates of 40 mm thickness it is vice versa. A big difference between the nucleation thresholds is found with plate thicknesses of 8 mm and 10 mm although the geometry is nearly the same. The v_D-E·A curves (Figure 8.3) show that a representation of the data which is independent of the plate thickness is not achieved this way. An unambiguous relation between the momentum flux where nucleation occurs and the plate thickness could not be recognized.

The results of the experiments with the highest impact velocities v_{PC} where only crack propagation at terminal crack velocity and no nucleation were observed are listed together with the results of the experiments with the lowest impact velocities v_{PD} where nucleation occurred in Table 8.6. The mean velocities and the standard deviations of v_{PC} and v_{PD} are specified below in the columns 2 and 3.

Table 8.1 Results with K5 plates of the thickness d = 8 mm

Shot No.	v_P [m/s]	E·A [N]	c_L [m/s]	c_T [m/s]	v_C [m/s]	v_D [m/s]
10247	40	526	--	3220 3360	1540	--
10281	48	757	--	3170 3180	1570	--
10251	54	958	5630	3150 3250	1580	3070
10250	70	1610	5830	3200 3140	1550	3360
10248	80	2102	5680	3110 3240	1640	3310

Table 8.2 Results with K5 plates of the thickness d = 17 mm

Shot No.	v_P [m/s]	E·A [N]	c_L [m/s]	c_T [m/s]	v_C [m/s]	v_D [m/s]
10298	48	1705	--	--	1520	--
10261	54	2158	5450	3080 3150	1570	--
10299	60	2664	5660	3040 3020	--	3500
10255	80	4736	5470	3310	1570	3460

Table 8.3 Results with K5 plates of the thickness d = 20 mm

Shot No.	v_P [m/s]	E·A [N]	c_L [m/s]	c_T [m/s]	v_C [m/s]	v_D [m/s]
10185	21.5	383	--	--	1520	--
10187	29	696	--	--	1470	--
10292	34	957	--	--	1620	--
10186	40	1325	5510	3080 3144	1550	--
10283	54	2414	--	--	--	3310

Table 8.4 Results with K5 plates of the thickness d = 28 mm

Shot No.	v_P [m/s]	E·A [N]	c_L [m/s]	c_T [m/s]	v_C [m/s]	v_D [m/s]
10207	29	875	--	--	1520	--
10206	40	1664	--	3340	1610	--
10209	48	2396	5710	3210 3350	--	3060
10294	54	3033	5660	3180 3090	1595	3380

Table 8.5 Results with K5 plates of the thickness d = 40 mm

Shot No.	v_P [m/s]	E·A [N]	c_L [m/s]	c_T [m/s]	v_C [m/s]	v_D [m/s]
10193	40	1696	--	--	1520	--
10293	48	2442	--	3010 3030	1550	3400
10199	54	3091	--	--	--	--
10194	80	6784	5680	--	--	3510

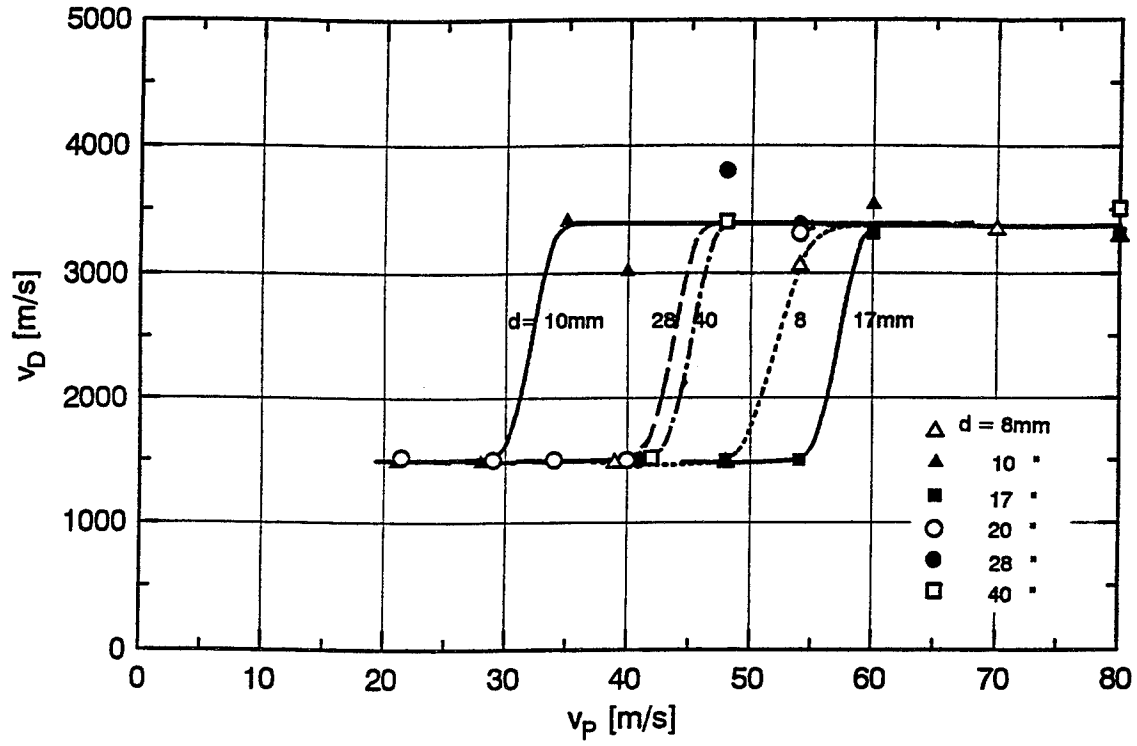


Figure 8.2 v_D versus v_P around the nucleation threshold for K5 plates of different thicknesses

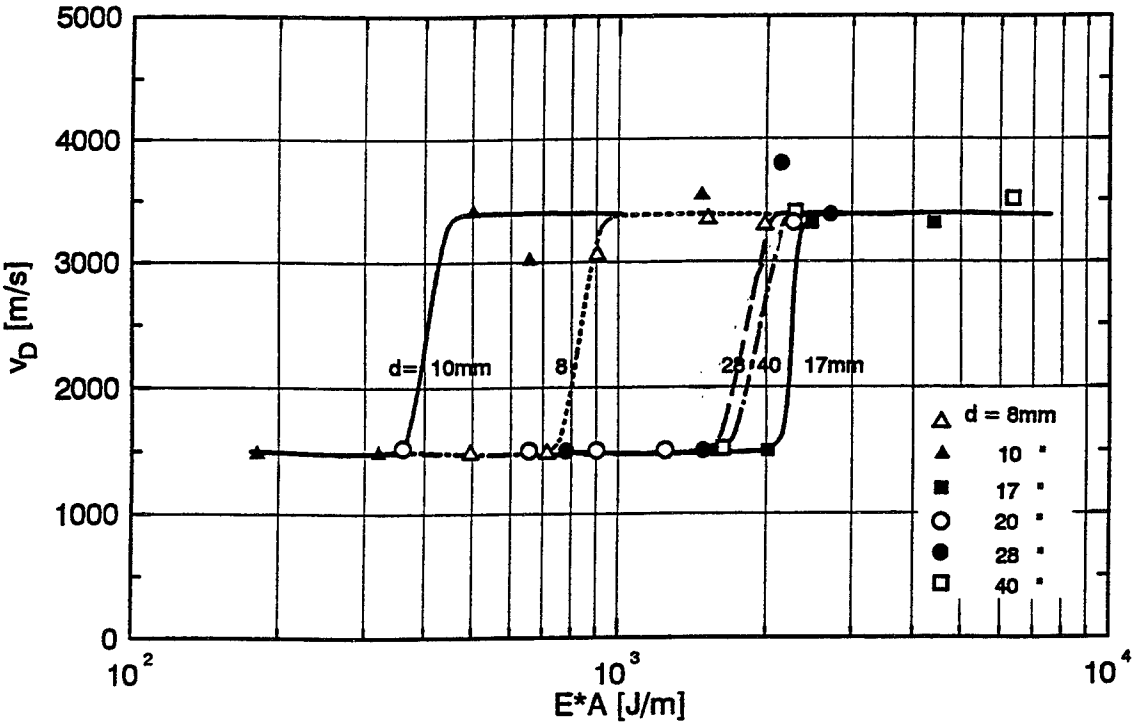


Figure 8.3 v_D - E·A curves around the nucleation threshold for K5 plates of different thicknesses

Table 8.6 Crack and damage velocities at the nucleation threshold with K5 plates of different thicknesses

d [mm]	v_{PC} [m/s]	v_{PD} [m/s]	v_C [m/s]	v_D [m/s]
1	2	3	4	5
8	48	--	1570	--
8	--	54	--	3070
10	28	--	1590	--
10	--	35	--	3420
17	54	--	1570	--
17	--	60	--	3500
20	40	--	1550	--
20	--	54	--	3310
28	40	--	1610	--
28	--	48	--	3060
40	40	--	1520	--
40	--	48	--	3400
	$\overline{v_{PC}}$ = 41.7 m/s ± 8.8 m/s	$\overline{v_{PD}}$ = 49.8 m/s ± 8.5 m/s		

A specific result of the experiments is that nucleation occurs with high probability in the impact velocity range from 41.7 m/s to 49.8 m/s when K5 plates (8 mm $\leq$ d $\leq$ 40 mm) are impacted with steel cylinders (D = 30 mm, L = 23 mm). In the case of constant caliber and different plate thicknesses the nucleation threshold ranges in a certain interval not only with respect to the impact velocity but also with respect to the momentum flux. An order of the nucleation threshold with respect to the plate thickness was not found.

9. Experiments with Blocks of K5

Three blocks of K5 glass of the dimensions 200 mm x 150 mm x 100 mm were available for impact experiments. The specimen were impacted on the sides with lengths of 200 mm x 150 mm with the same type of projectile used in the experiments with thin specimen. The tests were conducted at impact velocities of v_P = 90 m/s, 416 m/s and 1040 m/s. Figure 9.1 shows six selected photographs of shot no. 10259 (v_P = 90 m/s). The crack centers on the first photograph (17.9 μs) have a nearly circular contour. Single cracks can be recognized which emerge from the centers in all directions like prickles. However, the next photographs show that these cracks mainly grow in and against the direction of fire.

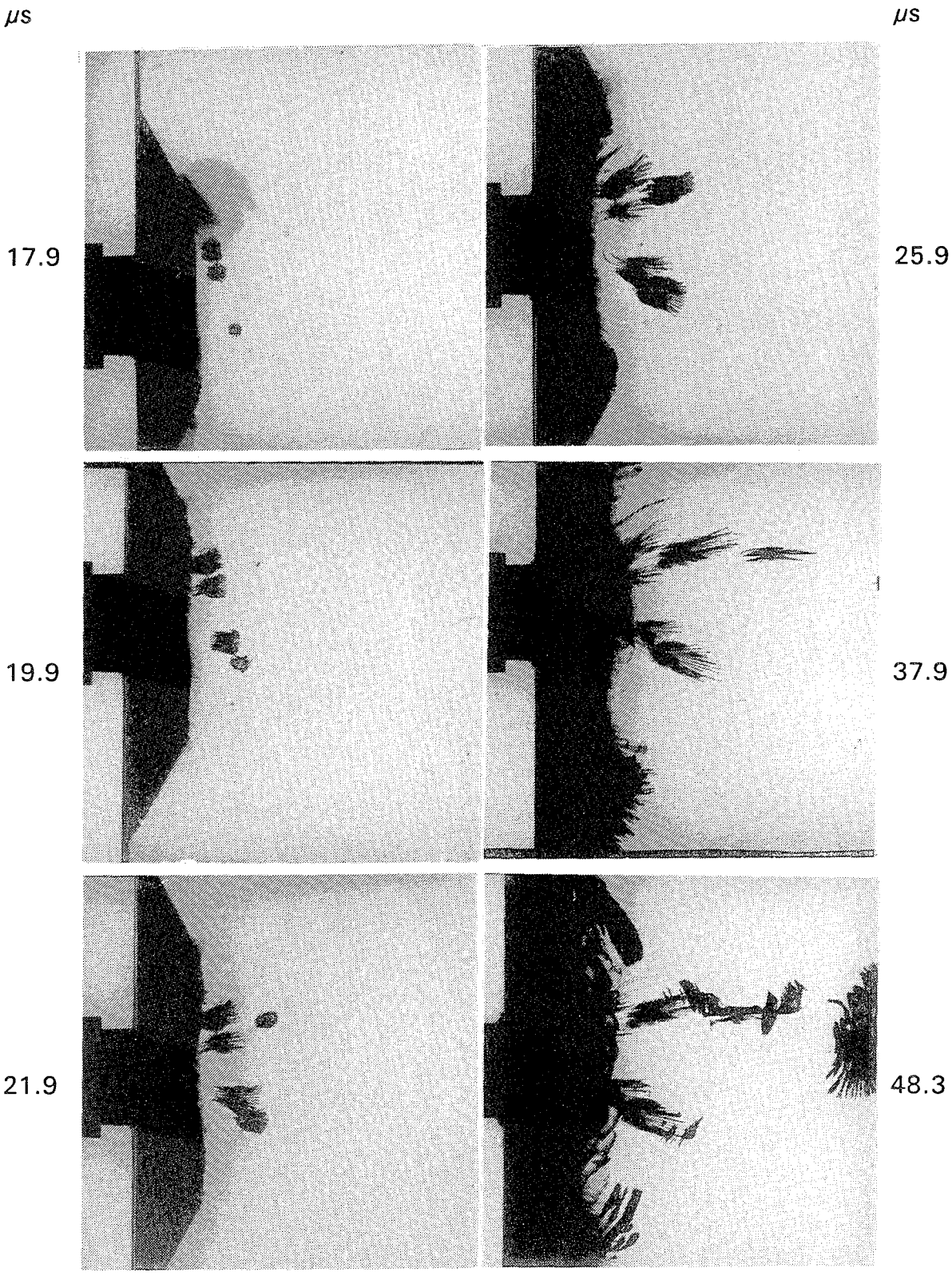
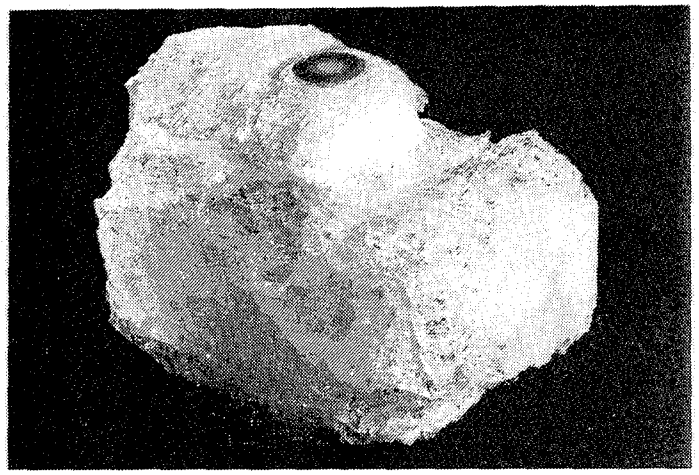
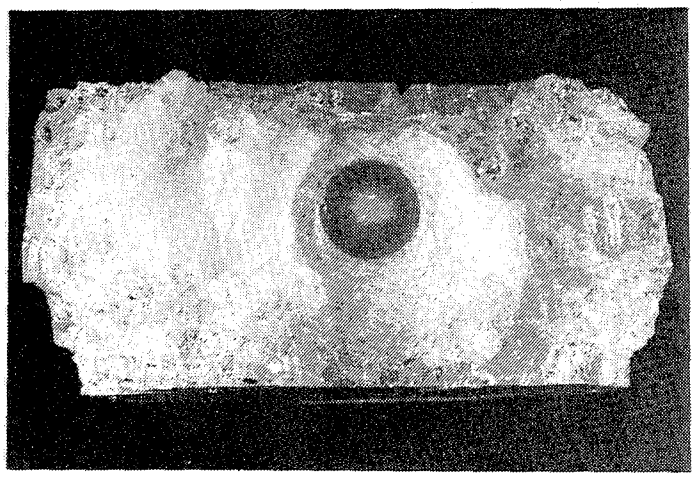


Figure 9.1 High-speed photographs of a K5 block of 100 mm thickness, v_P = 90 m/s, shot no. 10259

a)



b)



c)

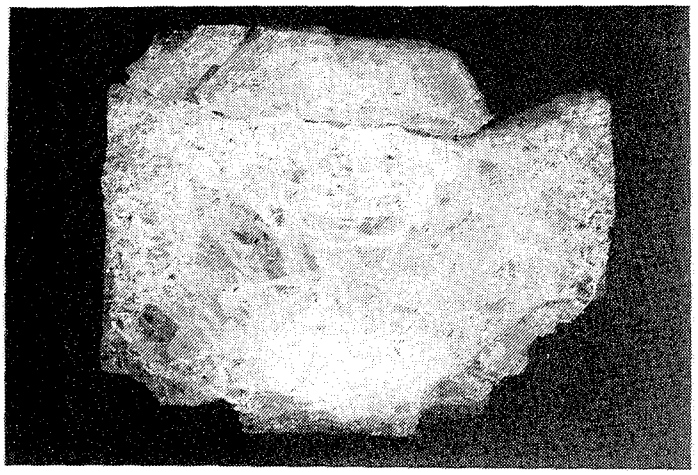


Figure 9.2 Different views of the impacted K5 block (shot no. 10259)
a) overview; b) top view; c) side view

Figures 9.2a, 9.2b and 9.2c show photographs of the recovered glass block. Especially the photographs 9.2a and 9.2b clearly show that the specimen was not disintegrated in the impact zone. The impact area is the center of a sequence of circular concentric fractures. These fractures include an angle of about 60° with the line of fire and form a sequence of conical shells. The front surface of the conical fragment in the center is just the impact area. When looking at the crack formation from the side, i. e., the perspective of the Cranz-Schardin camera, one recognizes that these cone cracks are identical with the secondary cracks. A cross section through the middle of a thick plate would reveal a fracture pattern similar to those observed with thin plates. The last photograph of the series shown in Figure 9.1 also reveals cracks that propagate perpendicular to the direction of fire. These cracks separate the front part of the glass block, which is interspersed among the secondary cracks, from the rest at a distance of about 30 mm from the impacted surface. This can be clearly seen in the side view of the specimen shown in Figure 9.2c.

The complete series of 20 photographs of a glass block impacted at 1040 m/s (shot no. 10327) is shown in Figure 9.3. The time interval between the photographs is about 1 μs. On the first five photographs no details can be recognized in the loaded zone behind the wave front. Damage of the glass and changes of the refractive index in the loaded region cause the deflection of the light so that this zone appears black. On the photographs 7 to 15 damage can be recognized directly behind the longitudinal wave. The enlargements of the photographs no. 10 and no. 15 shown in Figure 9.4 clearly reveal spherical crack centers ahead of the projectile close to the compressive wave front. In contrast to the crack centers observed at the low impact velocity or with thin plates no single crack tips can be seen here. But the evaluation of such centers demonstrated that they grow at the terminal crack velocity of K5 glass. This shows that the centers consist of cracks although single cracks cannot be distinguished on the photographs.

In the zones above and below the projectile crack centers are only observed in these parts of the specimen which have been passed by the transversal waves. In the schematic representation of the wave propagation (Figure 5.1) this corresponds to the region which is surrounded by the lines that connect the points A, G, H and B.

It is remarkable that the transversal waves are visible in thick glass specimen at high loadings. On the photographs 16 to 20 no more crack centers are generated between the longitudinal wave and the transversal wave. It is assumed that in this phase the amplitude of the longitudinal wave has decreased so far that the intensity is no longer sufficient for nucleation. As long as the intensity of the compressive wave is sufficiently high for nucleation, the damage velocity is approximately equal to c_L. This is confirmed by the path-time curve of this

experiment which is shown in Figure 9.5. This experiment also demonstrates that damage propagation at longitudinal wave velocity is possible in thick plates. The experiment proves furthermore that nucleation is possible without the influence of the shear waves generated at the surfaces of the target plate. The distance D between the pressure pulses is 135 mm with a plate thickness of 100 mm and a Poisson ratio $\mu = 0.227$.

The third glass block was impacted at 416 m/s. In this experiment a second camera was added to the equipment in order to observe the damage propagation from the side and from the top simultaneously. Figure 9.6 shows a schematic drawing of the experimental set-up. A mirror was positioned below the specimen which was placed on a polycarbonate plate so that the light from the sparks could pass through the target fixing and the target. A lens focuses the light above the specimen and a mirror reflects it towards the camera. The optical arrangement for the observation from the side is the same as in all the experiments with thin plates. Figure 9.7a shows the complete series of photographs in the side view, the top view photographs are shown in Figure 9.7b. The frame rate was 500 kHz.

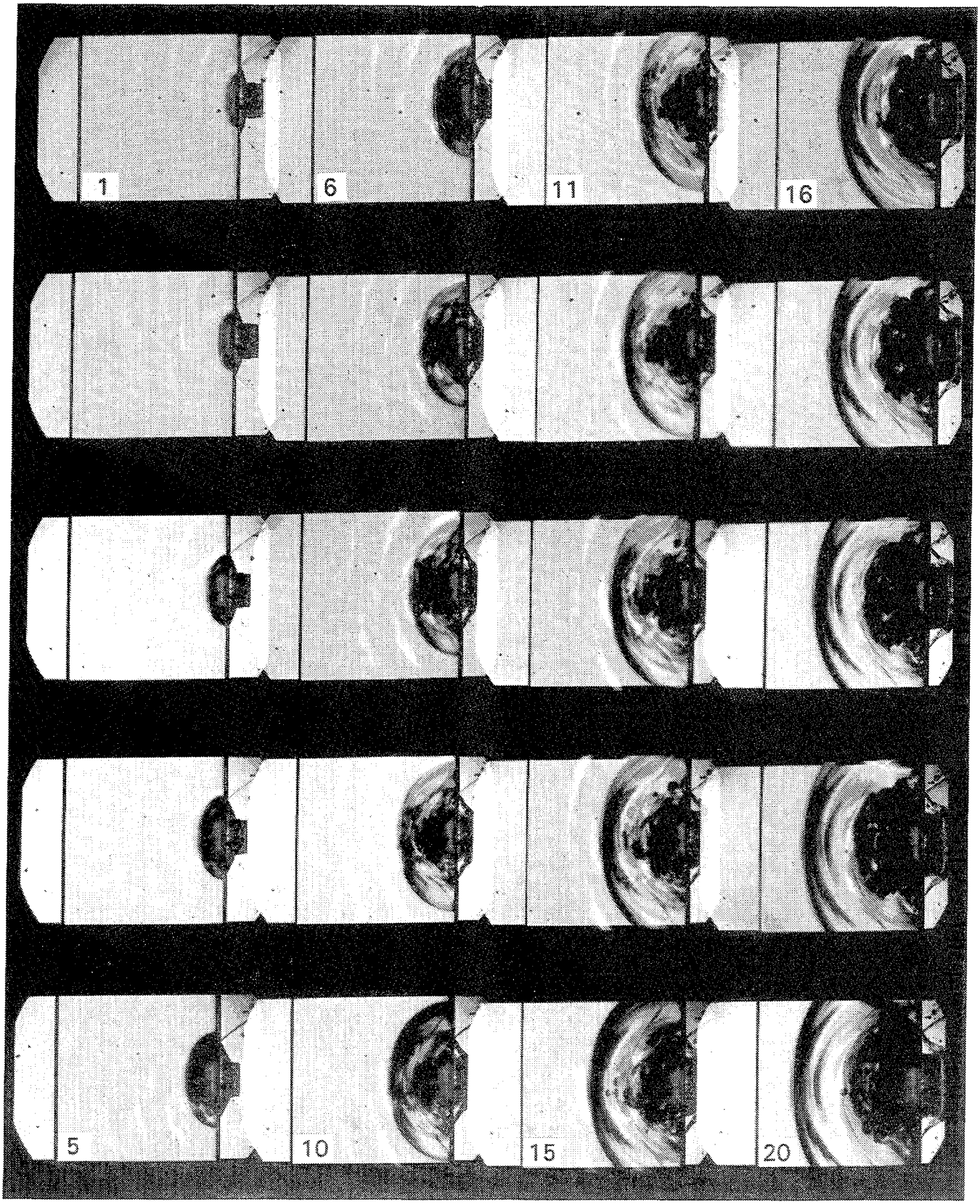


Figure 9.3 Complete series of high-speed photographs of a 100 mm thick K5 block impacted at v_P = 1040 m/s (shot no. 10327); frame rate 1 MHz (impact direction from right to left)

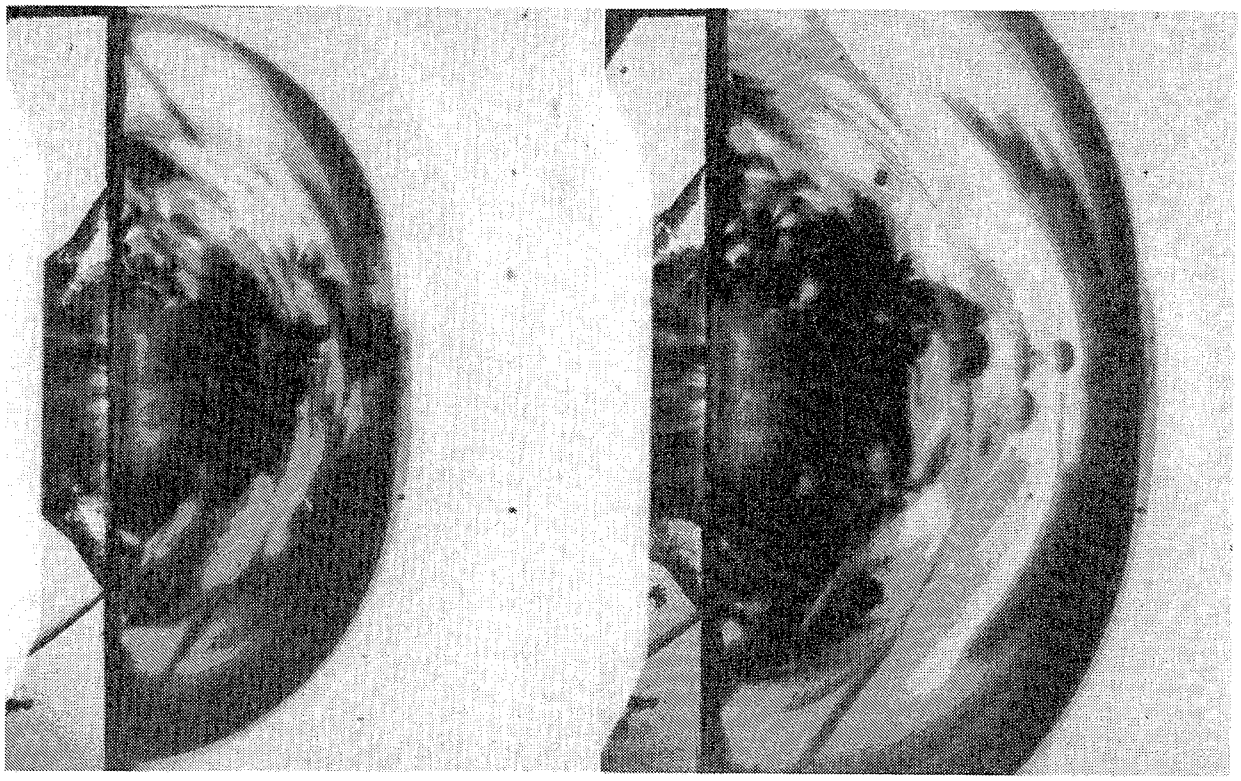


Figure 9.4 Enlargements of the photographs no. 10 and no. 15 of shot no. 10327 (impact direction from left to right)

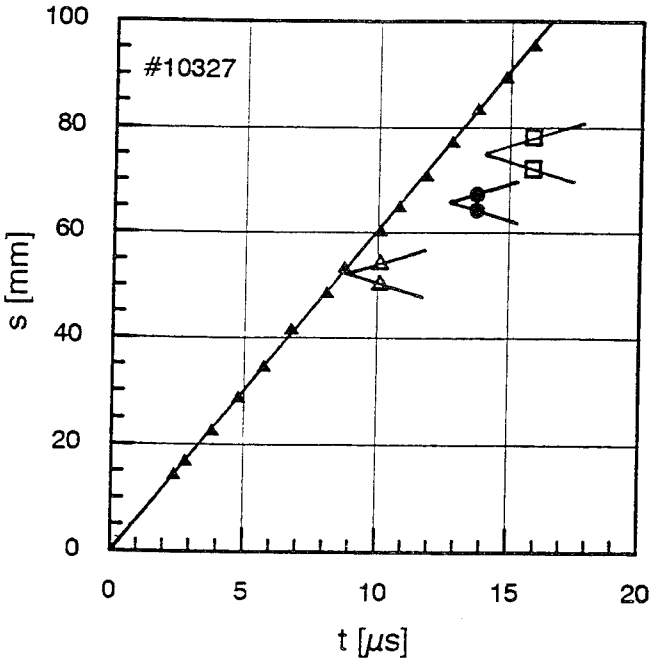


Figure 9.5 Path-time plot of shot no. 10327

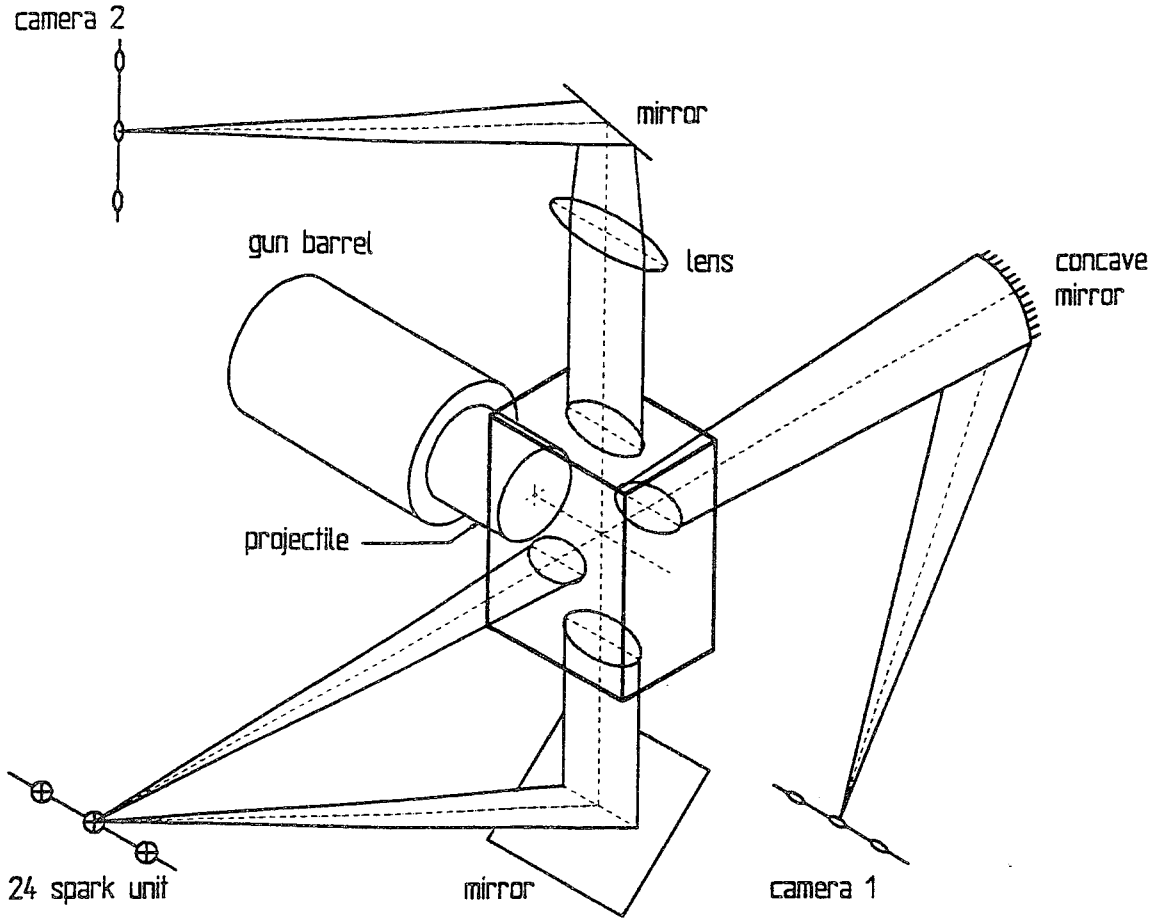


Figure 9.6 Schematic of the experimental configuration for simultaneous side view and top view high-speed photography

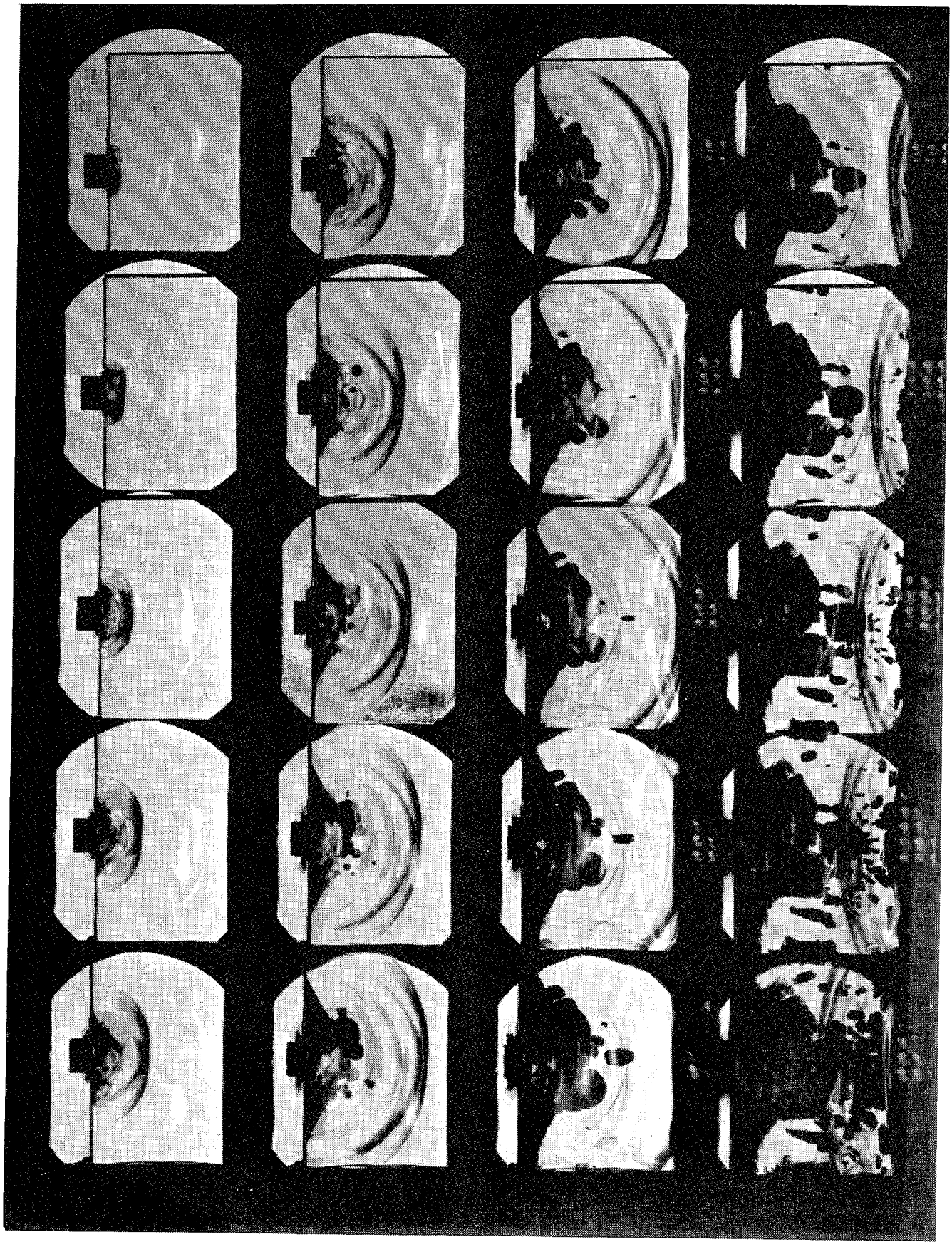


Figure 9.7a Complete series of high-speed photographs of a K5 block (200 mm x 150 mm x 100 mm) impacted at 416 m/s; side view (shot no. 10697)

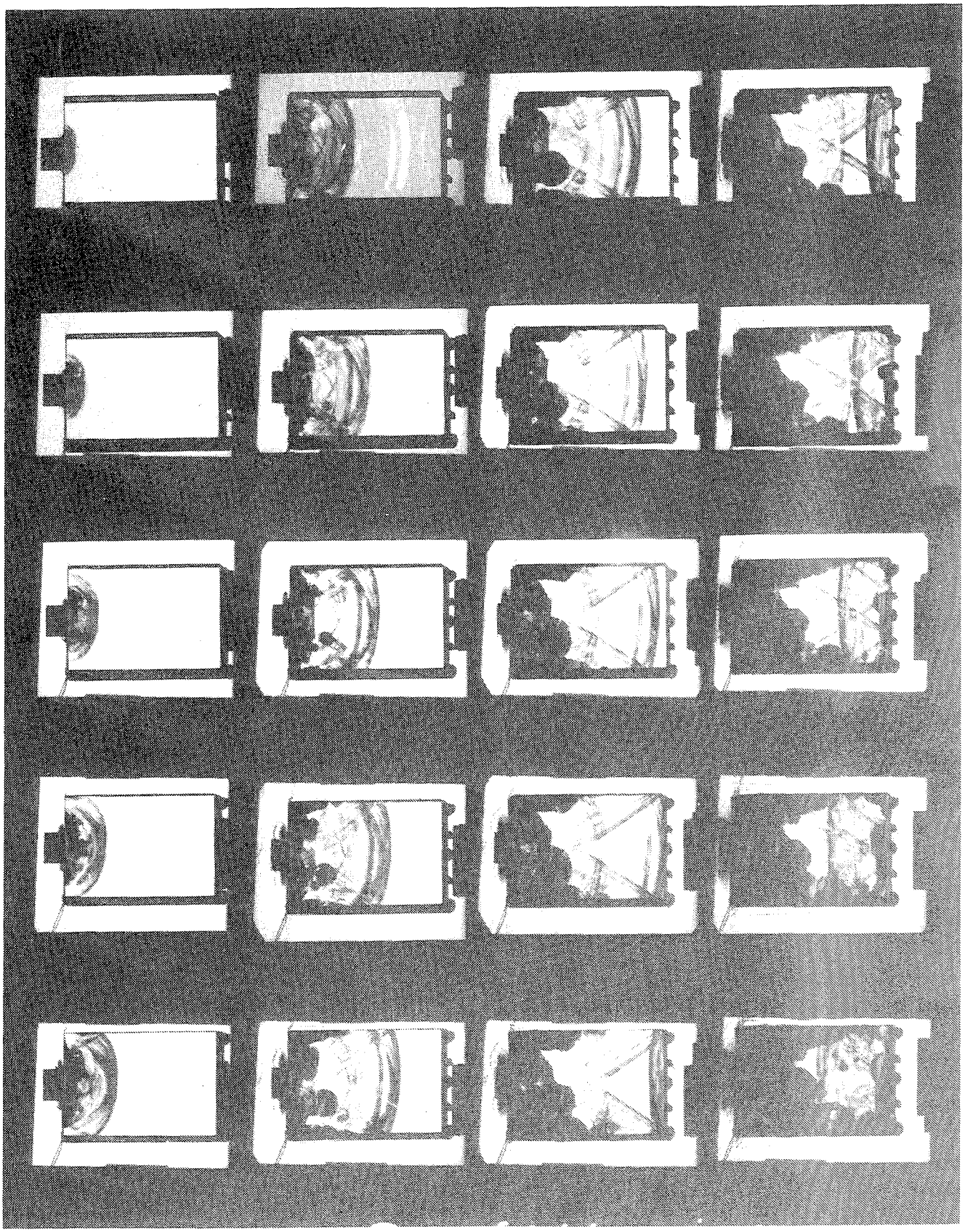


Figure 9.7b Complete series of top view photographs of shot no. 10697

The wave propagation is very clearly visible in both directions of observation. Two transversal waves are observed which are generated at the edge of the projectile. The development of spherical crack centers is visible most clearly from photographs 6 to 10. The first crack center is to be seen close behind the upper transversal wave on photograph 6. Only the development of this first crack center can be observed in the top view because it covers the other ones. The path-time curves (Figure 9.8) reveal that the first three leading crack centers are generated by the transversal wave. The fourth crack center which is observed first on photograph 12 seems to be generated by the longitudinal wave. Its position in the path-time curve is between the two straight lines which represent the longitudinal and the transversal waves. This crack center exhibits the same ellipsoidal shape as it was found with most of the crack centers observed in thin plates. A comparison of the side and top view photographs shows that this crack center is placed on the surface of the specimen. Figure 9.9 shows enlargements of photograph 13 in both directions of observation. The crack center considered is marked with an arrow. The series of the top view photographs also shows that cracks are continuously generated along the surfaces. It is not possible to make a clear distinction between the cracks that started from the surface and those cracks which started from the impacted edge of the specimen in the side view. But the combination of both directions of observation has demonstrated that the spherical crack centers are generated in the interior of the glass block. From this result it is concluded that the spherical crack centers observed close behind the longitudinal wave in shot no. 10327 (v_P = 1040 m/s) were in the interior of the specimen, too.

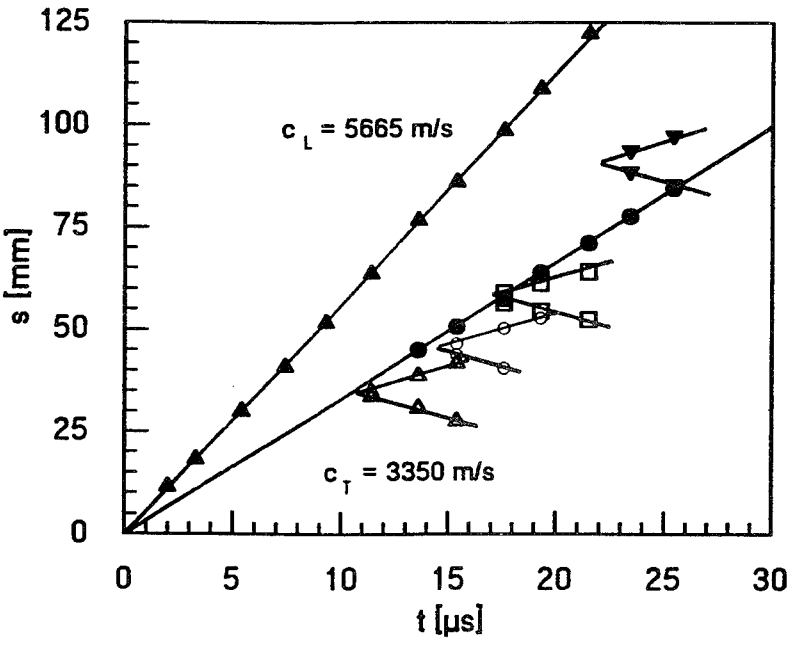


Figure 9.8 Path-time plot of shot no. 10697

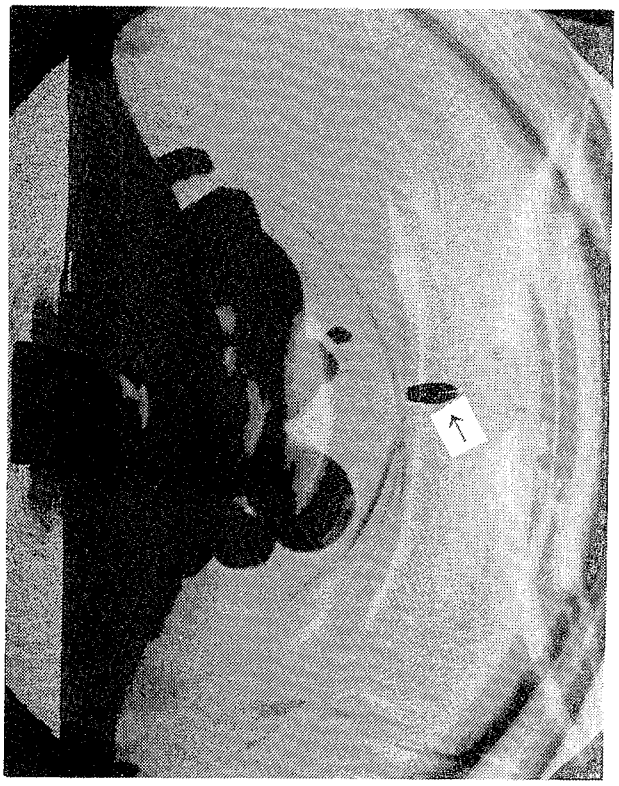


Figure 9.9a Shot no. 10697, photograph no. 13, side view, 25 μs after impact



Figure 9.9b Shot no. 10697, photograph no. 13, top view, 25 μs after impact

10. Failure Waves

10.1 Review of Work on Failure Waves

An alternative approach to the description of fracture and damage propagation in glasses instead of the damage velocity concept was chosen by several investigators during the last four years. The concept of failure waves was introduced first by Rasorenov, Kanel, Fortov and Abasehov in 1991 [16]. They performed planar shock wave experiments with fused quartz and the optical glass K19. The free surface velocity was measured and from the wave profiles it was inferred that a zone of failed material expanded into the specimens from the impacted surface. This process was described and interpreted as the propagation of a failure wave. Failure wave velocities $\leq$ 1.5 km/s were observed. Spallation was not found when the impact conditions were chosen such that the expected spall plane was located in the zone which had been passed by the failure wave. From this the authors concluded that the failed layer had zero resistance to tension and a reduced impedance was inferred from the increase of the surface velocity in the wave profile.

Kanel et al. [17] obtained similar wave profiles in experiments with K8 glass where the longitudinal and lateral stresses were measured with manganin gauges.

In order to examine the existence of failure waves in glass Brar et al. [18] performed plate impact experiments (uniaxial strain) on soda-lime glass and pyrex. The stress profiles were measured at the interface of the rear side of the target plate and a PMMA backing by means of manganin gauges. Brar et al. interpreted the results of the plate impact experiments in terms of failure waves and concluded that "the spall strength of soda lime glass depends on the location of the spall plane with respect to the propagating failure wave". The failure wave velocity observed was 1.7 km/s.

Additionally, bar-impact experiments (uniaxial stress) were performed on these materials (Brar and Bless [19]) and the fracture propagation was observed with a high-speed Imacon framing camera. Brar and Bless observed failure front velocities in pyrex bars between 2300 m/s and 5200 m/s. The failure front velocity increased with increasing loading.

Recently, Raiser and Clifton [20] examined the influence of surface roughness on the formation of failure waves. They conducted plate impact experiments on aluminosilicate glass specimens and the free surface velocity-time-profiles were measured. The experiments delivered no evidence to suggest a significant influence of surface roughness on the formation of a failure wave. On the basis of these experiments Clifton [21] proposed a micromechanical explanation of the

failure wave phenomenon and developed an analytical model for the interpretation of failure waves as propagating phase transitions.

10.2 Plate Impact Tests of K5 Glass

The optical glass K5 (ρ = 2.59 g/cm^3, c_L = 5750 m/s) used in the investigations of fracture and damage is very similar to the K19 glass (ρ = 2.62 g/cm^3, c_L = 5600 m/s) used by Kanel. Therefore, it was expected that plate impact tests with K5 glass could provide a link between the failure wave concept and the damage velocity concept.

Two experiments on K5 were performed by H. Nahme and his coworkers at EMI, Freiburg. Steel plates of three millimeters thickness were used as impactors. The thickness of the target plates was 10 mm. In the first experiment, which was conducted at an impact velocity of v_P = 765 m/s the signal was cut after 2.5 μs and no statement could be made about failure wave propagation or spallation. The second experiment was conducted at v_P = 839 m/s. The corresponding free surface velocity-time plot is shown in Figure 10.1, the distance-time-plot in Figure 10.2. The wave profile (Fig. 10.1) exhibits no typical pull back signal as it is found when spallation occurs. The late rise of the free surface velocity at about 2.6 μs does not seem to indicate spall because in case of spallation the rise in velocity should occur earlier (Fig. 10.2). Additionally, a reflection of the waves at the spall plane would have lead to another decrease of the free surface velocity. When the rise at 2.6 μs is interpreted as the arrival of a compression wave, caused by reflection of the release wave at a layer of failed material with a lower impedance, a failure wave velocity can be derived of about 1000 m/s. We suppose that the increase of pressure could have prevented the formation of spall in this case [22].

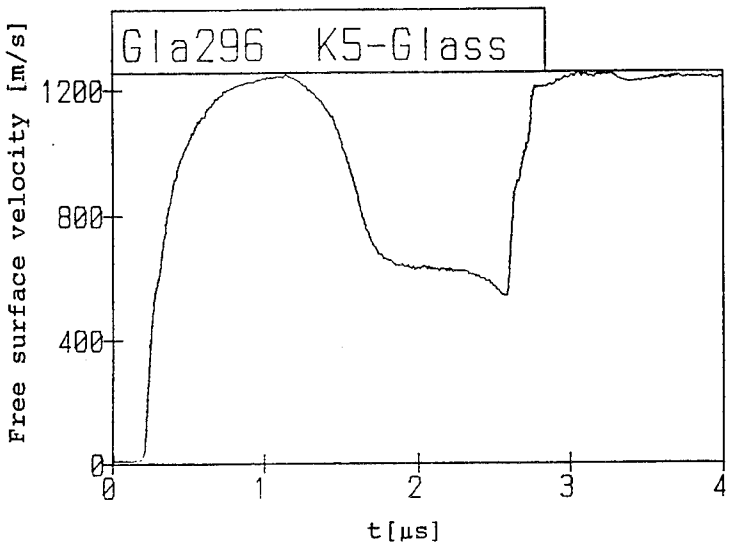


Figure 10.1 Free surface velocity versus time from plate impact experiment Gla296 on K5 glass, performed by H. Nahme and coworkers (EMI, Freiburg)

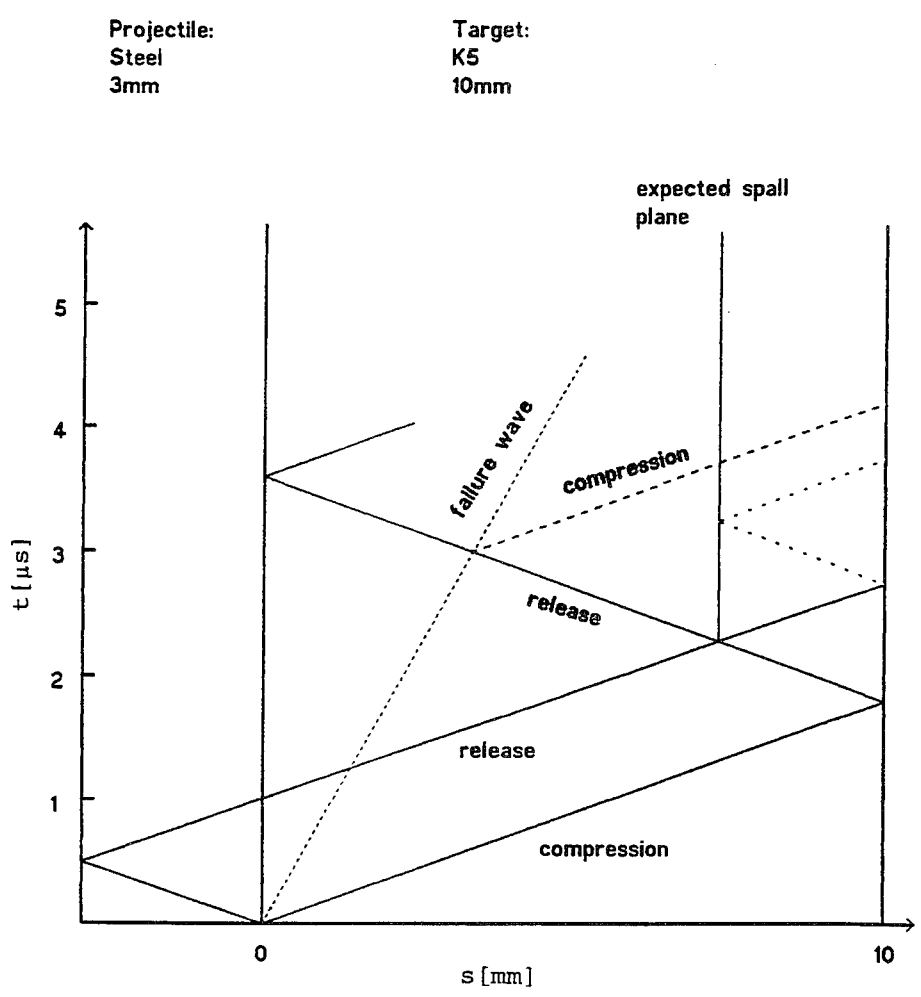


Figure 10.2 Distance-time plot of the plate impact experiment Gla296

10.3 Discussion

On one hand, the failure wave velocity of 1000 m/s, which was derived from our plate impact experiment on K5 glass, corresponds to the velocities of failure waves observed by Kanel in the K19 glass. On the other hand, these velocities are low compared to the damage velocities that were observed at similar impact velocities with edge-on impact experiments. Nevertheless, we think that there is no contradiction between these results. In the plate impact experiments the specimen is submitted to uniaxial strain whereas the loading situation is very complex in the edge-on tests. Furthermore there are big differences in the dimensions of the specimens and the time intervals of observation. In the plate impacts only the damage is probed that propagates from the impacted surface into the specimen over a period of a few microseconds. In the edge-on experiments the damage is considered up to distances of 100 mm or more (experiments with blocks of K5) from the impact surface over time intervals of about 30 μs. When comparing the results of the two different types of experiments one has to be aware of the fact that in the damage velocity concept the damage velocity is determined by the formation of several crack centers which have been initiated by the stress waves. This means that the damage in the zone which has been passed by the stress waves is restricted to the crack centers first. (The crack centers themselves expand at terminal crack velocity in all directions.) For example a damage velocity equal to transversal wave velocity c_T does not mean that the specimen is totally destroyed in the region which has been passed by the transversal waves. This is clearly demonstrated by the experiments on the thick blocks of K5 glass (see for example Fig. 9.7a and 9.7b). The damage is localized in the crack centers at the front. If in such an experiment the wave propagation were probed in the same way as in the plate impact tests, the results for failure wave velocities would be different from the observed damage velocity. The release wave would probably not be reflected from the few crack centers which are advanced most. Probably the wave would be reflected only when the density of crack centers and fracture is high enough.

11. Summary of the Results with Glasses

- The propagation of waves and damage at impact of cylindrical steel projectiles was investigated qualitatively and quantitatively for four different types of glass (K5, F6, SF6 and float glass).

- The damage velocities were measured as a function of impact velocity and the thresholds for the nucleation of cracks were determined.

- All four glasses reveal a similar behaviour. The damage velocity equals terminal crack velocity at low loadings, rises to transversal wave velocity when nucleation occurs and approaches longitudinal wave velocity with very high loadings. The behaviour was observed independent of the thickness of the target plates.

- Three experiments with thick blocks of the optical glass K5 were performed. Simultaneous side view and top view high-speed photography was applied in one of these experiments. This technique allows to distinguish between surface damage and damage in the interior of the specimen.

- The experiments demonstrated that nucleation is induced in the interior of the specimen when the intensity of the stress waves exceeds a certain threshold. The spherical shape of the crack centers indicates that the cracks grow in all directions at the same speed.

INTENTIONALLY LEFT BLANK.

Part II.

Experiments with Ceramics

INTENTIONALLY LEFT BLANK.

12. Compilation of the Experiments

Three types of ceramics were tested: "PAD" - SiC-B (PAD = Pressure Assisted Densified) and "PAD" - TiB_2 from CERCOM Company and the CeramTech A 1898 Al_2O_3 from HOECHST Company. The experiments were conducted in a similar way to the experiments with glasses. The specimens were impacted edge-on with steel cylinders of 30 mm diameter and 23 mm length. The dimensions of the specimens were also 100 mm x 100 mm x 10 mm. Fracture propagation was observed on the surfaces of the specimens by means of a Cranz-Schardin camera during the first 20 μs after impact. In order to visualize the cracks the surface of the ceramics has to be polished mirror-like. Otherwise the intensity of the reflected light would not be sufficiently high to observe details. With the Al_2O_3 specimens a mirror-like surface cannot be achieved. Therefore, they were coated with a thin layer of silver or aluminium.

It is not possible to summarize the fracture phenomena observed with ceramics as it was done with the glasses, where a few types of damage could be distinguished clearly. Therefore, the single experiments are described in detail in Chapter 14. An attempt to classify the different fracture phenomena is made in Chapter 15. The experiments performed are listed in the Tables 12.1 (SiC), 12.2 (TiB_2) and 12.3 (Al_2O_3). The damage velocities denote either the mean velocity of the fastest fracture observed or the mean velocity of a fracture front. This is explained in the description of each experiment. Two SiC specimens were tested at impact velocities below 30 m/s. With the impact velocity v_P = 20 m/s no cracks were generated during the time interval of observation. However, the impacted specimen exhibits one single, visible crack which started from the impacted edge and has a length of about 1.5 cm. The fracture propagation at v_P = 25 m/s could not be observed because of a trigger failure. The specimen was separated into several big fragments in this experiment.

Table 12.1 Experiments with SiC

Shot No.	v_P [m/s]	E·A [N]	v_D [m/s]
10105	31	227	4860
10111	54	688	5660
10107	85	1705	5900
10118	150	5310	(7950)
10137	175	7228	6620
10325	185	8077	8270
10116	220	11422	9400
10359	369	32134	9250
10358	446	46944	-*m
10362	513	62108	10090
10142	671	106257	10260
10145	1033	251833	-*m
10146	1033	251833	-*f
10147	1040	255258	11150

*m misalignment of the specimen
*f trigger failure

Table 12.2 Experiments with TiB_2

Shot No.	v_P [m/s]	E·A [N]	v_D [m/s]
10108	31	256	4850
10110	54	776	5600
10130	62	1023	6680
10119	70	1303	7290
10109	85	1922	7470
10326	108	3103	8370
10136	150	5985	8760
10117	210	11731	9250
10360	353	33146	8390*m
10367	564	84614	10420
10144	683	124086	-*f
10143	784	163540	11195
10366	1000	266000	11510

Table 12.3 Experiments with Al_2O_3 (CeramTech A 1898)

Shot No.	v_P [m/s]	E·A [N]	v_D [m/s]
10131	31	311	3090
10132	85	2337	5310
10134	150	7277	5635
10135	220	15653	9630
5570	707	104968	9400
5542	1062	139200	9500

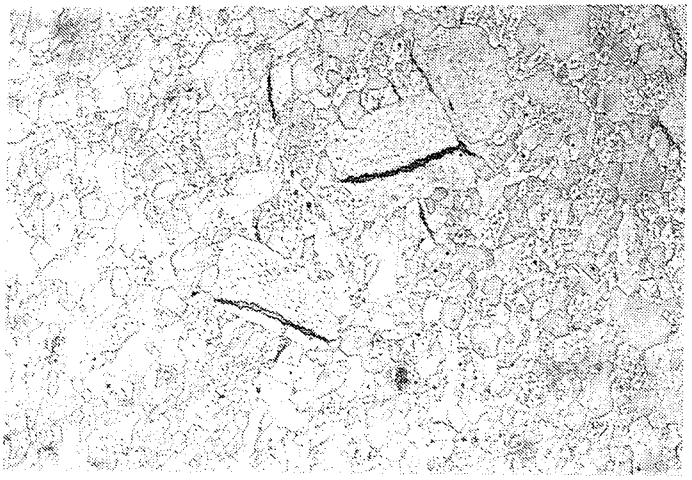
13. Material Properties

Physical and mechanical properties of the ceramics as given by the manufacturer are listed in Table 13.1.

Table 13.1 Physical and mechanical properties of the ceramics

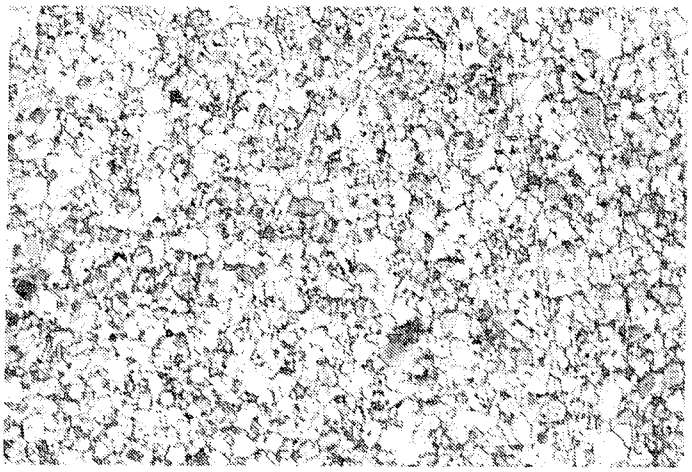
Material	SiC	TiB_2	Al_2O_3 (98 %)
Density ρ [g/cm^3]	3.23	4.52	3.79
Young's Modulus [GPa]	427	537	360
Compressive Strength [GPa]	3.41	4.82	4
Bulk Modulus [GPa]	223	233	---
Shear Modulus [GPa]	195	249	---
Poisson's Ratio	0.14	0.11	---
c_L [m/s]	12250	11285	10440
c_T [m/s]	7765	7431	---

The structure of the three types of ceramics is very different which can be recognized from the three micrographs shown in Figure 13.1. The SiC is a very fine grained material with an average grain size of 2 μm, whereas the average grain size in the alumina is 9 μm. The maximum grain length observed with these two ceramics is about 30 μm. Much bigger differences in the size of the grains occur in the TiB_2, where the dimensions of the smallest grains are a few micrometers and the largest grains attain lengths of about 180 μm. However, the most important feature of this material is, that it exhibits cracks already in the initial state. These cracks predominantly occur along the boundaries of the large grains or they cleave large grains over their full length.



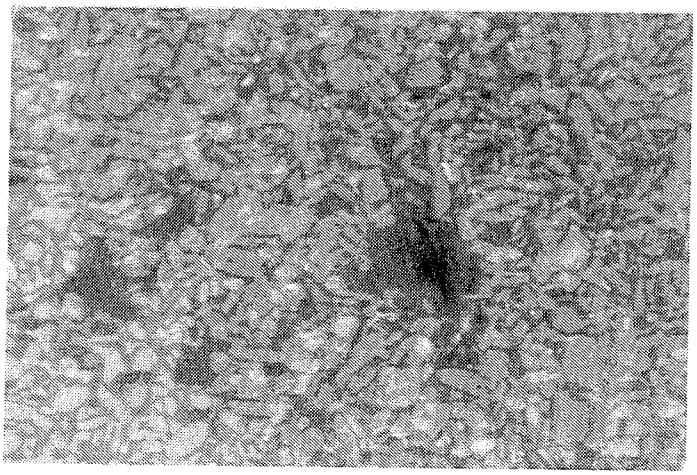
50 μm

a) TiB_2



20 μm

b) SiC



20 μm

c) Al_2O_3

Figure 13.1 Micrographs of the different ceramics in the initial state

14. Description and Evaluation of Damage

14.1 Experiments with SiC

Shot No. 10105 (SiC, v_p = 31 m/s)

A selection of six high-speed photographs shows the specimen between 4 μs and 20 μs after impact in Figure 14.1 (direction of loading from left to right). On some of the photographs concentric rings can be seen on the surface of the ceramic plate which are caused by the polishing process. Several cracks start from the impacted edge. The crack that is opened most widely starts from the impact site of the lower edge of the projectile. Above this crack two other cracks (R1, R2) propagate nearly parallel on a curve into the specimen. Branching occurs frequently with the lower crack. The mean velocities of the two cracks R1 and R2 are v_{C1} = 3690 m/s and v_{C2} = 4860 m/s. The corresponding path-time curves are shown in Figure 14.2. All the cracks that could be seen on the high-speed photographs were found in the specimen which could be rebuilt from the recovered fragments (Fig. 14.3). The fine cracks that branch off R2 can be recognized, too, but they do not reach to the back side of the plate. Only the main fracture pierces the plate completely.

When comparing the high-speed photographs to the photographs of the reassembled specimens one has to take into consideration that all the photographs of the specimens are flipped over with respect to the impact axis.

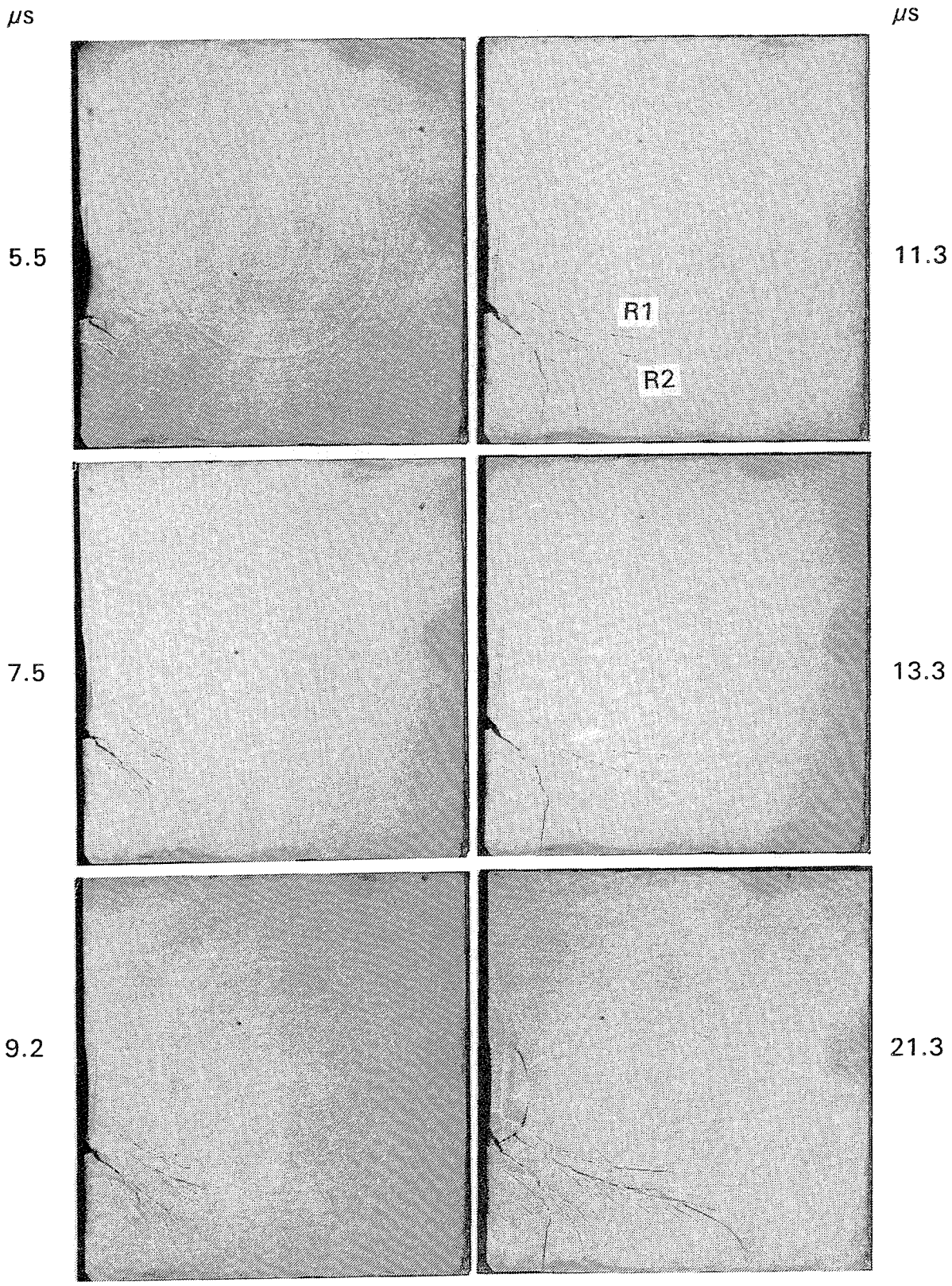


Figure 14.1 High-speed photographs of shot no. 10105

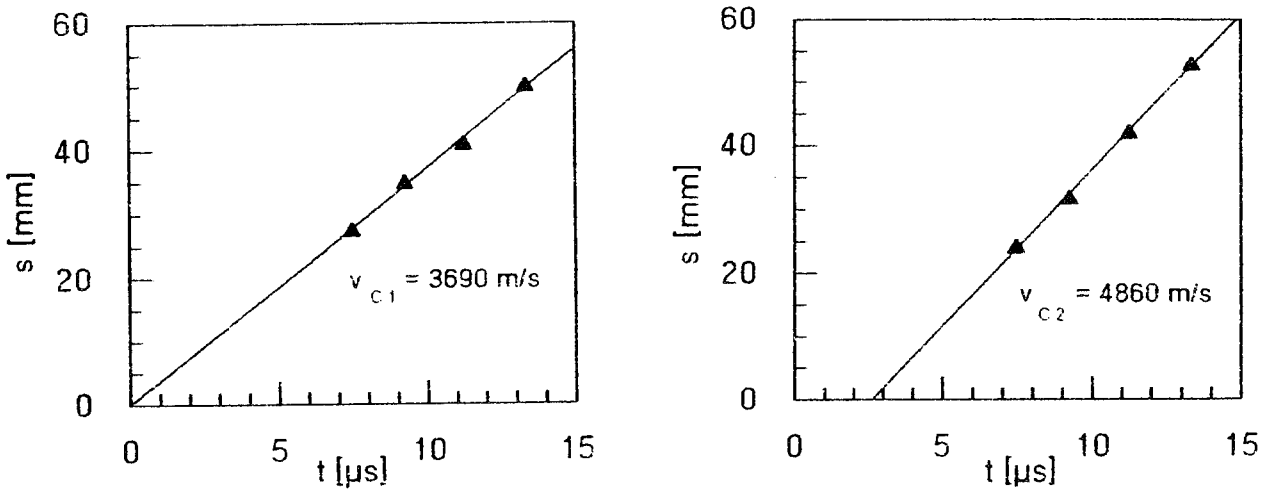


Figure 14.2 Path-time plots of shot no. 10105

Impact site →

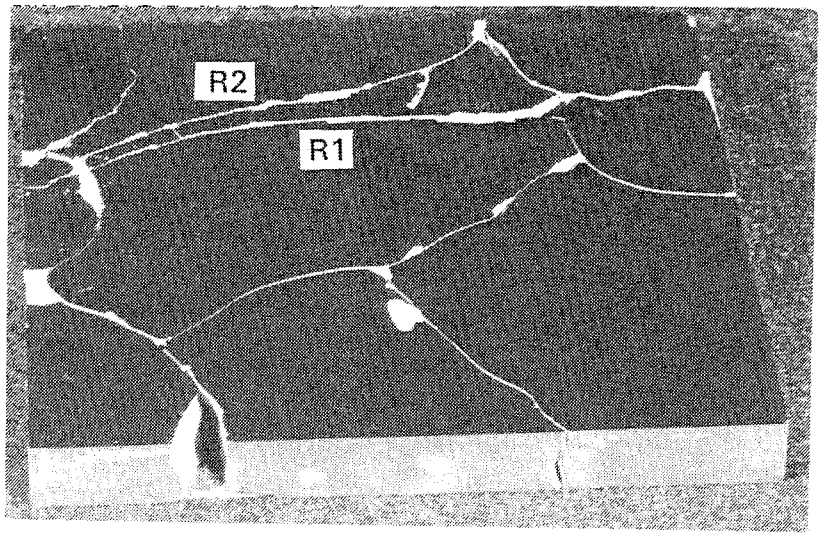


Figure 14.3 Reassembled specimen of shot no. 10105

Shot No. 10111 (SiC, v_p = 54 m/s)

The first one of the high speed photographs (Fig. 14.6) shows that crack formation starts at the impact of the upper edge of the projectile. Several cracks which propagate nearly parallel form a triangular fracture zone, similar to the secondary fracture zones observed with glasses. This can be recognized most clearly from photograph No. 4 8 μs after impact (Fig. 14.6). The crack which starts from the impact site of the upper edge of the projectile divides into three main branches. The velocity of the three branches is in the range from 4670 m/s (Fig. 14.7a) to 5230 m/s (Fig. 14.7b). From the 4th photograph on, two other, frequently branching cracks are observed which propagate with a mean velocity of 5660 m/s (Fig. 14.7c). The last photograph shows clearly that the upper one of these two cracks has a sharp edge first. Figure 14.4 shows the impacted specimen rebuilt from the recovered fragments. The arrow points to the place of the transition between the two fracture types. An inspection of the crack surfaces (Fig. 14.5) exhibits the place where the transition from a crack with sharp edges to a crack with fuzzy edges occurs. The fracture surfaces are smooth from the impacted edge on. Then, several grooves radiate from a place on the back surface of the plate can be seen. The further crack propagation generates rough crack surfaces where no directed structure can be recognized.

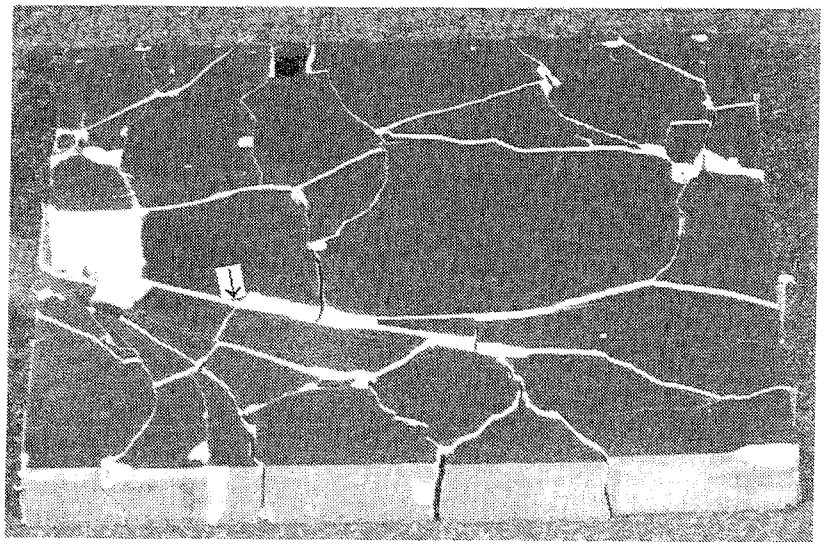


Figure 14.4 Reassembled specimen of shot no. 10111

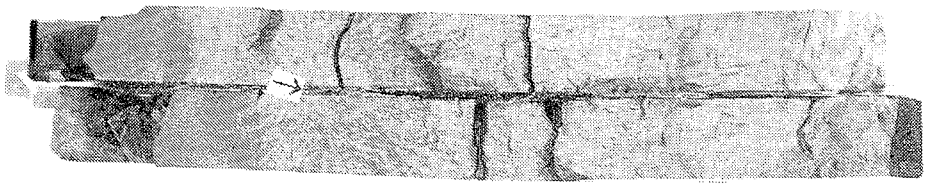


Figure 14.5 Fracture surface which changes from smooth (sharp edges) to rough (fuzzy edges) of shot no. 10111

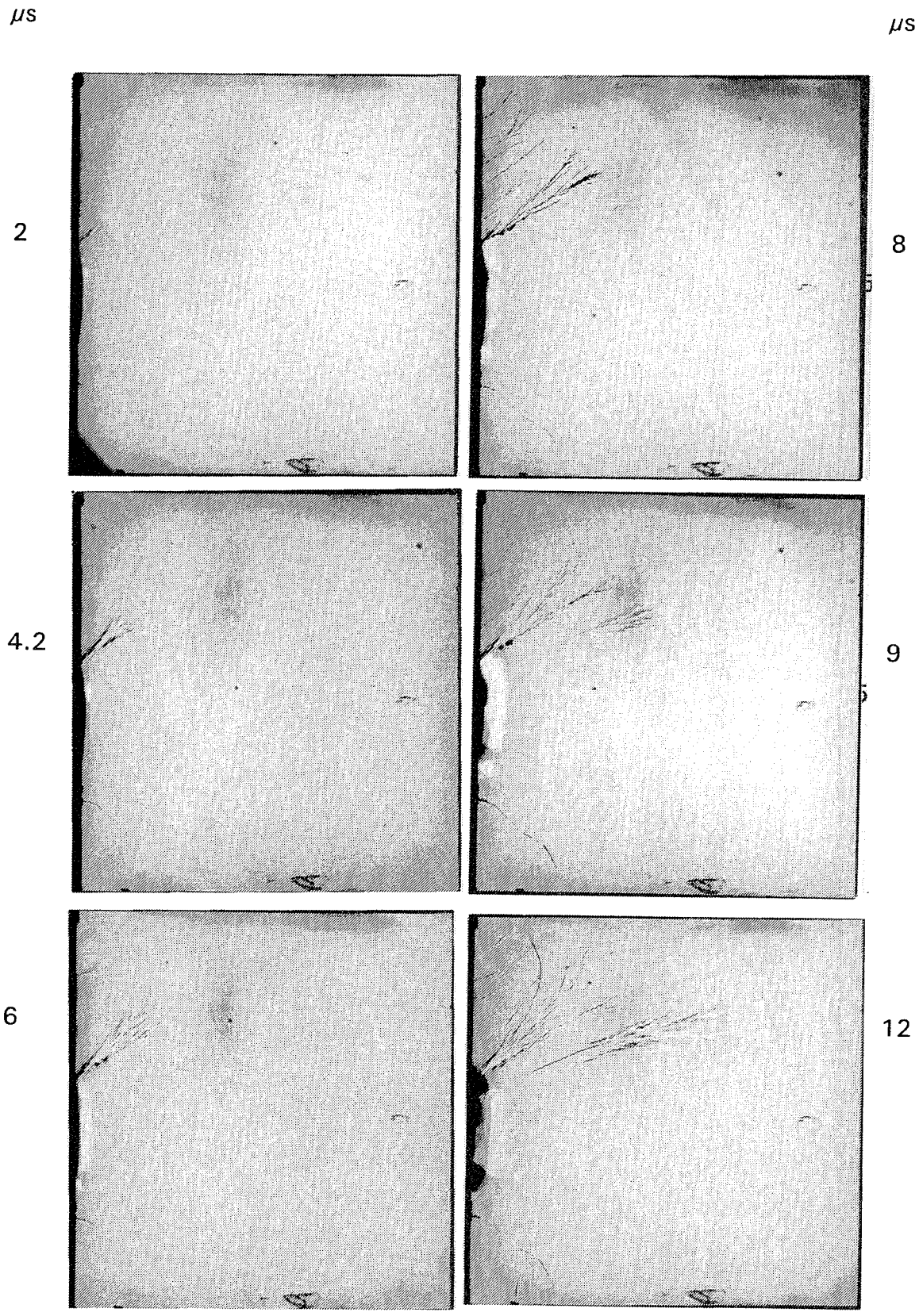


Figure 14.6 High-speed photographs of shot no. 10111

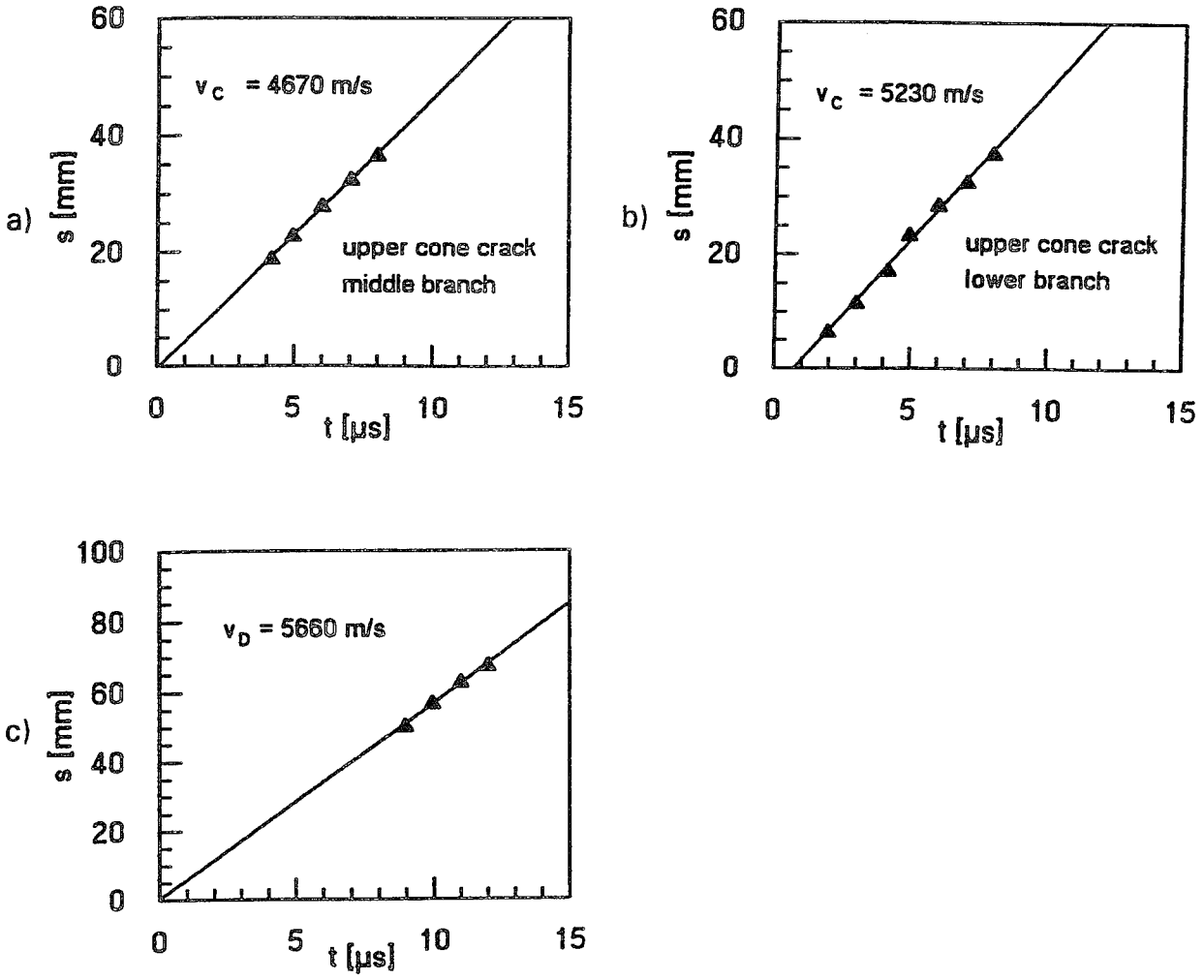


Figure 14.7 Path-time plots of shot no. 10111

Shot No. 10107 (SiC, v_P = 85 m/s)

The high-speed photographs (Fig. 14.8) show the specimen during the interval of time from 4 μs to 18 μs after impact. Many cracks radiate from the impacted edge. The cracks that start from the impact site of the edge of the projectile have opened most widely in the beginning (photographs 1 - 3). These cracks will be denoted cone cracks in the following. The designations for the different types of cracks are chosen analogous to the designations of the fracture types in glass. The cracks which are generated in the region between the cone cracks are called primary cracks. The cracks above and below the cone cracks are denoted secondary cracks. The secondary cracks start in a direction perpendicular to the impacted edge, change their direction of propagation after a very short time and then grow nearly parallel to the cone cracks. This can be recognized most clearly on photograph 1.

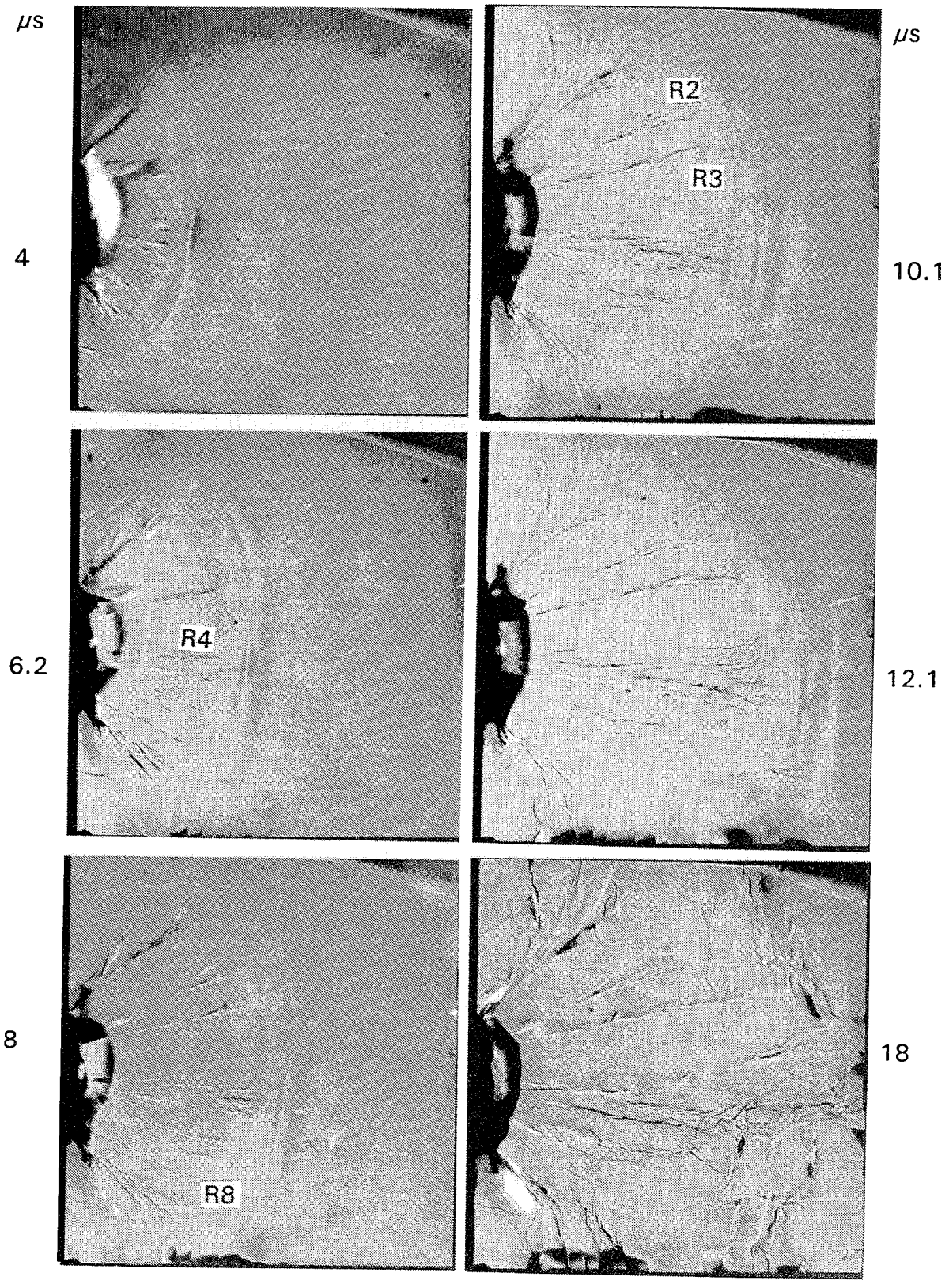


Figure 14.8 High-speed photographs of shot no 10107

A wave front precedes the fracture front. The mean velocity of the wave is 7180 m/s (Fig. 14.10 a), which means that it is a transversal wave. The damage which can be seen at the lower edge of the specimen, in front of the observed wave, is generated during the reflection of the longitudinal wave. Photograph 5 shows that the cracks which branch off the main fracture suddenly include a bigger angle with the main direction of fracture. This is due to the interaction of the crack tips with the relief wave that was generated at the rear edge of the specimen.

The area immediate in front of the projectile appears black on the photographs, which means that no light is reflected to the camera from there. The contour of this area changes with time. Parts of the surface within this area which appear black on one photograph, are again visible at a later time. From this observation it can be concluded that elastic deformation of the ceramics is one of the causes for the deflection of the light. Additionally, shell-shaped fragments are generated in the impact zone. When such a fragment is separated from the ceramic plate it sometimes happens that the polished surface of the fragment is inclined with respect to the surface of the undamaged specimen just at such an angle, that the light from one spark is reflected to another lens of the camera. A part of the film is then exposed twice and the contour of the fragment appears more bright on the photograph. The bright spot in photograph 1 results from such a process, too.

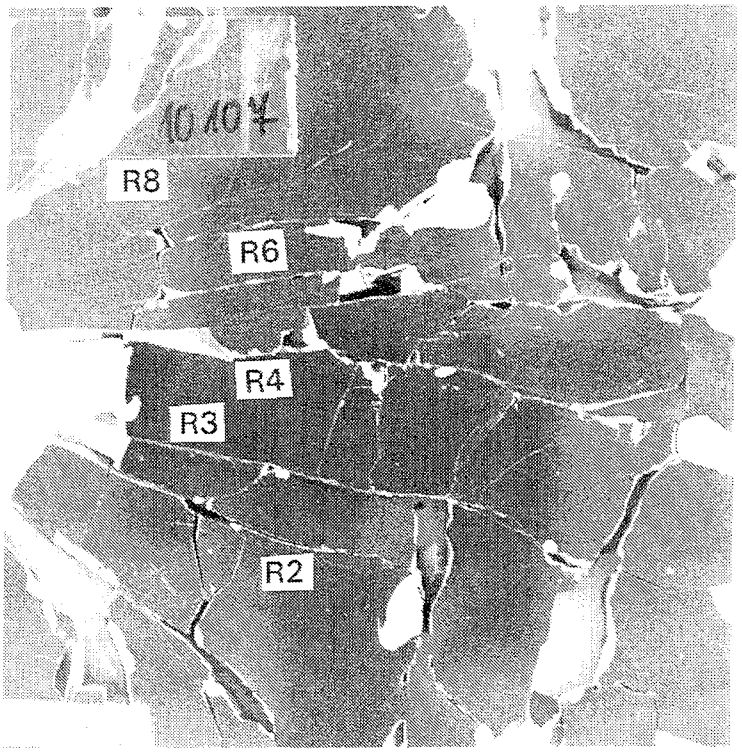


Figure 14.9 Reassembled specimen of shot no. 10107

All the cracks that had been observed during impact were found in the specimen which was rebuilt from the recovered fragments (Fig. 14.9). The surfaces of the radial cracks R2 to R4 are smooth along the first 10 to 15 mm from the impacted edge and become rough then. The cracks R5 and R6 do not pierce the specimen on the first 25 mm from the impacted edge. R7 and R8 do not pierce the ceramic plate over their full length. The mean velocities of the cracks were in the range from v_{C1} = 4900 m/s to v_{C2} = 5220 m/s (Fig. 14.10), the mean velocity of the fracture front was v_D = 5900 m/s.

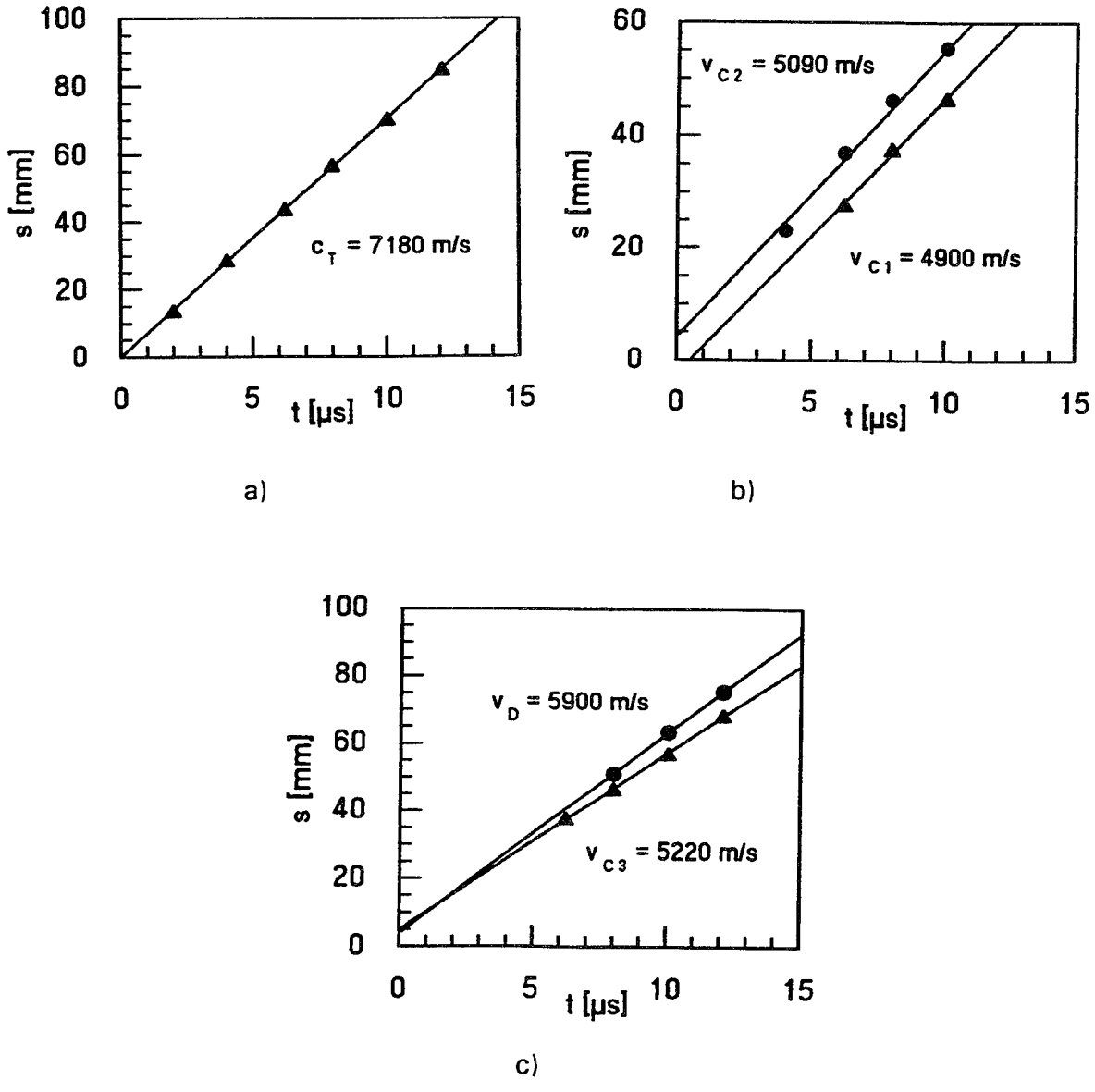


Figure 14.10 Path-time plots of shot no. 10107

Shot No. 10118 (SiC, v_p = 150 m/s)

The high-speed photographs (Fig. 14.11) show the specimen over a period of 11 μs. The fracture pattern consists of cone cracks, about 15 radial cracks and a few secondary cracks. The black area is restricted to the region between the cone cracks. The wave ahead of the fracture front propagates at a mean velocity of 7150 m/s (Fig. 14.12a). The mean velocity of the radial cracks varies in the range from 4960 m/s to 5380 m/s (R6) excepted R8 and R12. (The upper cone crack has the number one. The other cracks are counted clockwise.) R8 grows much faster (v_{C8} = 7950 m/s) than the other cracks whereas R12 propagates much slower (v_{C12} = 4400 m/s). The mean velocity of the upper cone crack is 4110 m/s. A compilation of the corresponding path-time curves is shown in Fig. 14.12b to 14.12e. The measured values of the positions of different crack tips are nearly equal in some cases. Therefore, not all the path-time curves are shown in Fig. 14.12.

One of the secondary cracks could be observed on several photographs. The mean velocity is 4350 m/s.

An inspection of the projectile showed that the specimen had been slightly misaligned with respect to the shot axis. The projectile hit the plate on the back side first. This is probably the reason for the difference of 2 μs between the extrapolated onset of fracture and wave propagation (Fig. 14.12a) and explains the intersection of the straight lines.

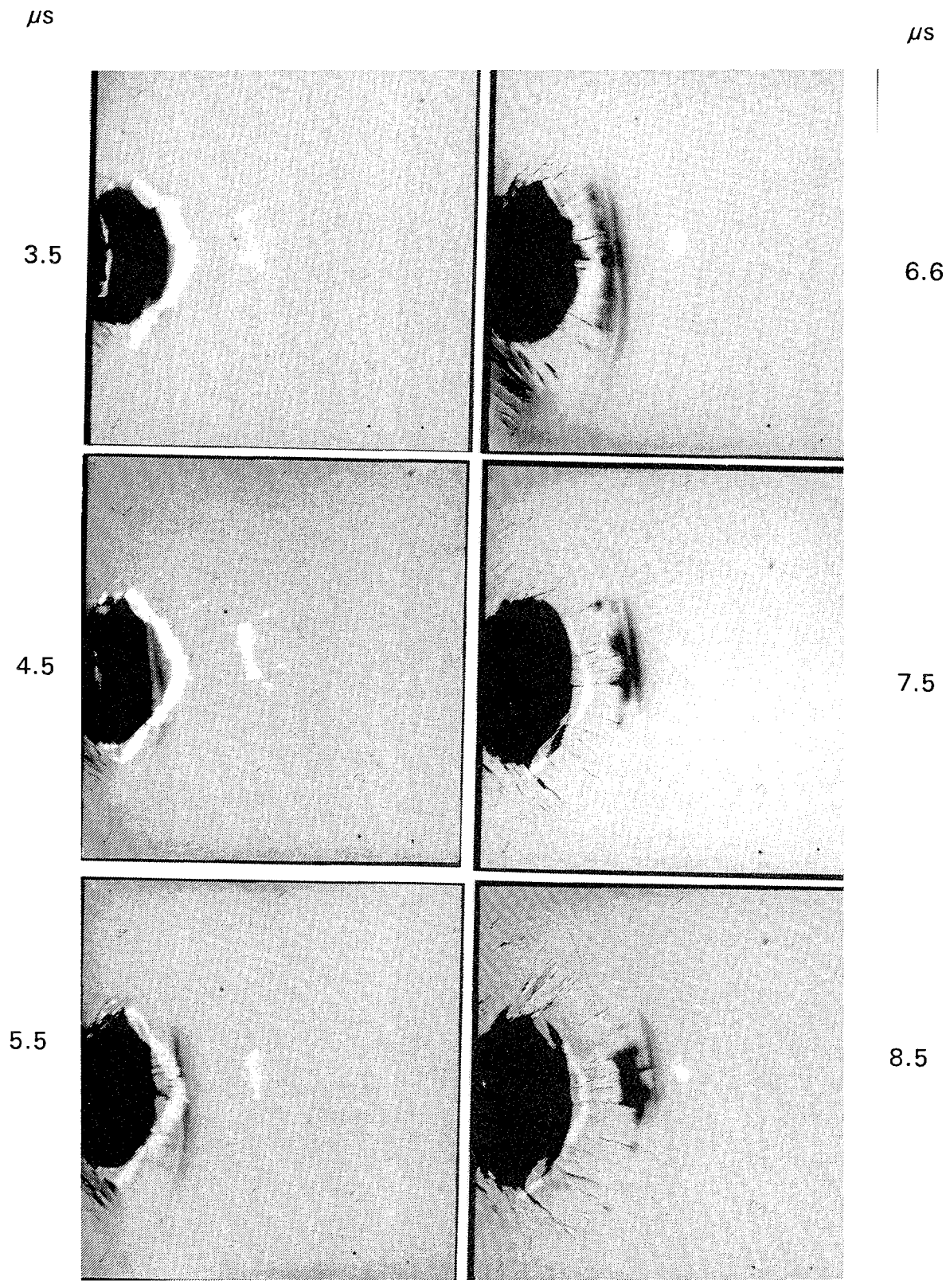


Figure 14.11 High-speed photographs of shot no. 10118

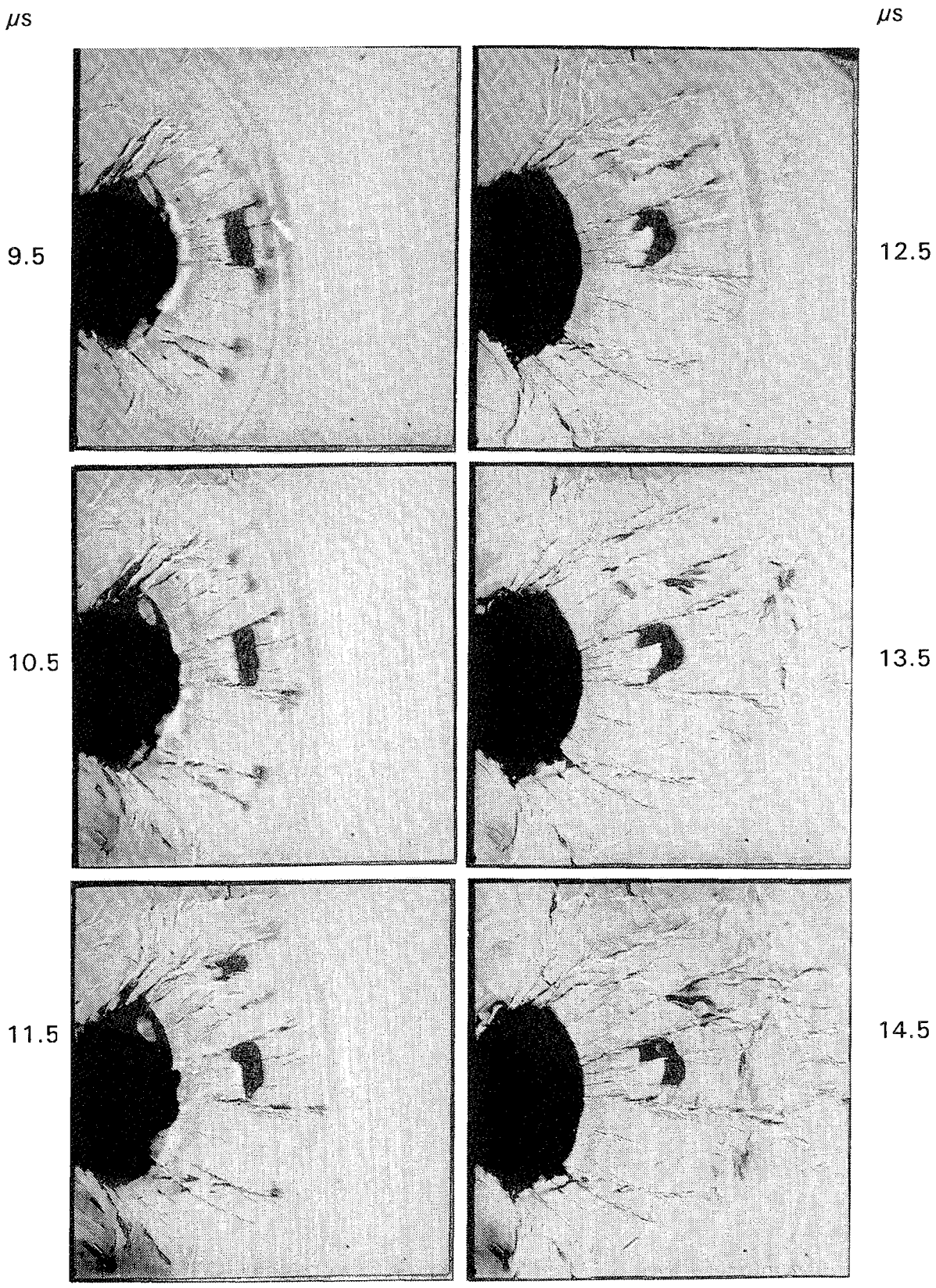


Figure 14.11 High-speed photographs of shot no. 10118

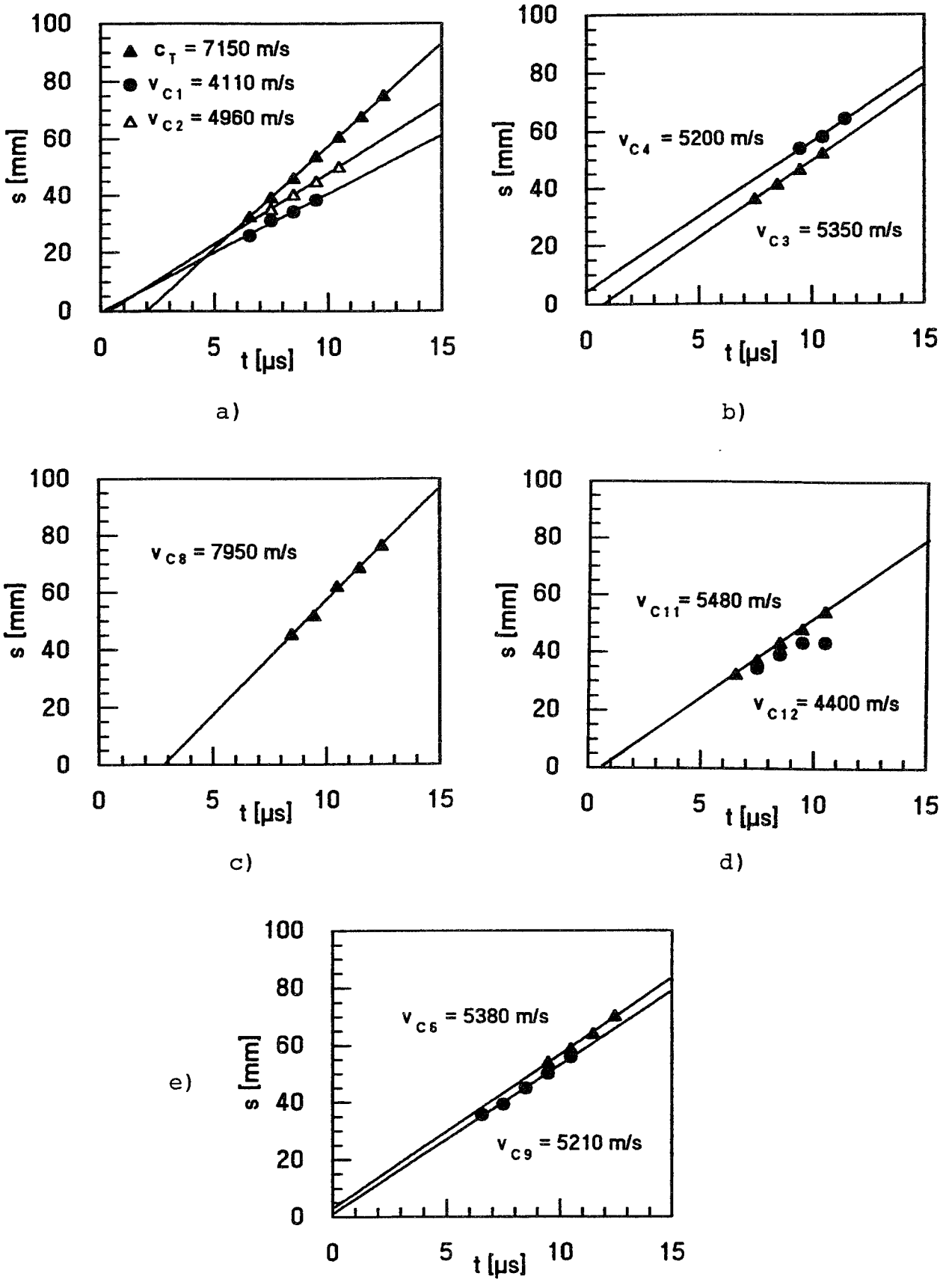


Figure 14.12 Path-time plots of shot no. 10118

Shot No. 10137 (SiC, v_p = 175 m/s)

The photographs in Figure 14.14 show the development of damage in the SiC specimen impacted with 175 m/s. In particular, the photographs 4 to 6 clearly exhibit secondary cracks below the impact zone. The evaluation of the positions of the crack tips resulted in mean velocities of 2910 m/s, 3060 m/s, 3540 m/s and 3980 m/s. Three of the primary cracks could be observed over a period of several microseconds. The mean velocities are v_{C1} = 6050 m/s, v_{C2} = 6620 m/s and v_{C3} = 6500 m/s (Fig. 14.13). The other primary cracks could not be evaluated because of the black area, which was restricted to the region between the cone cracks in this experiment, too.

At a distance of about 1 cm from the rear edge of the specimen a spall zone can be observed on photograph 10. The next photograph shows a second spall zone between the edge of the plate and the first spall zone.

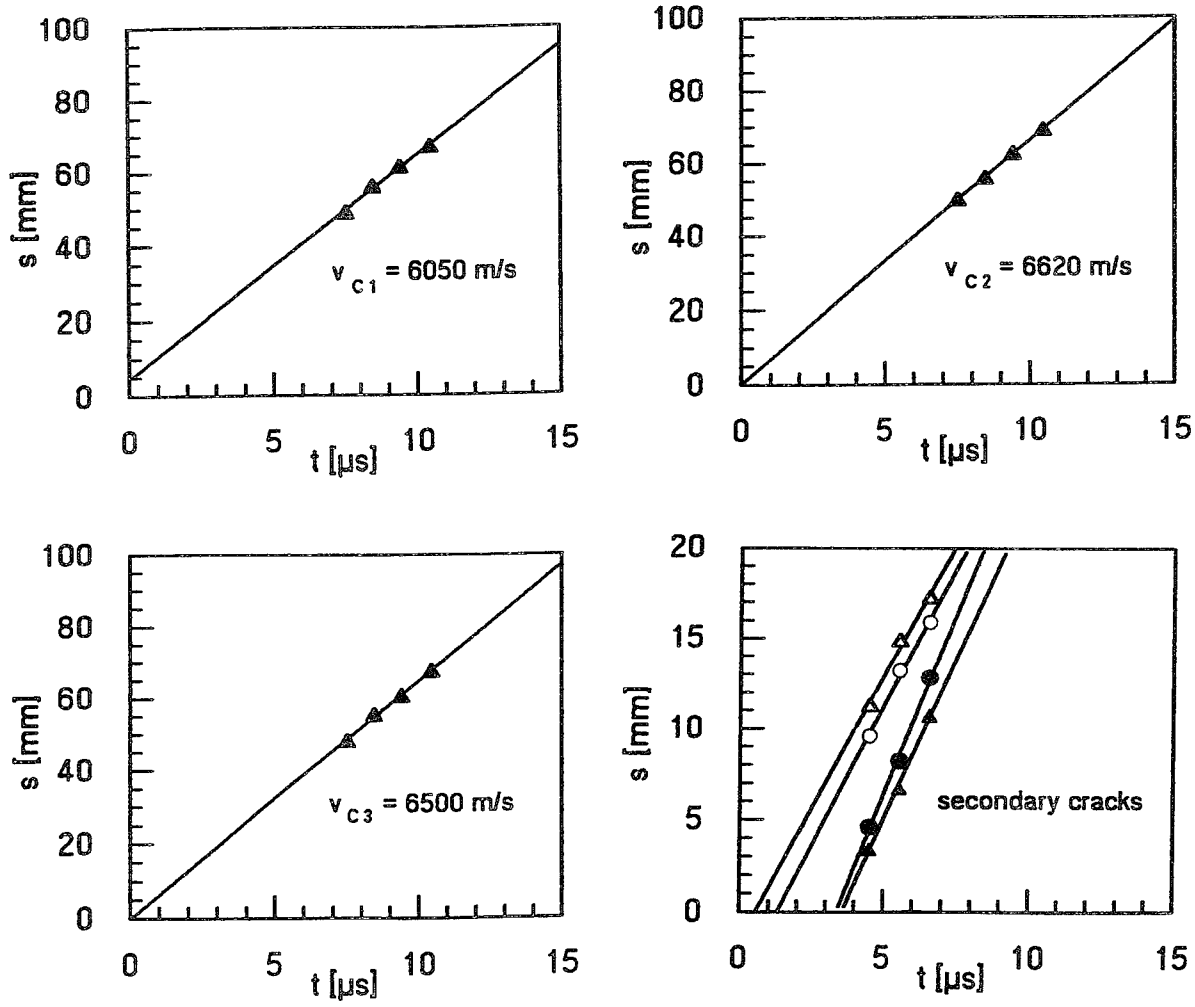


Figure 14.13 Path-time plots of the main fractures R1, R2, R3 and the secondary cracks

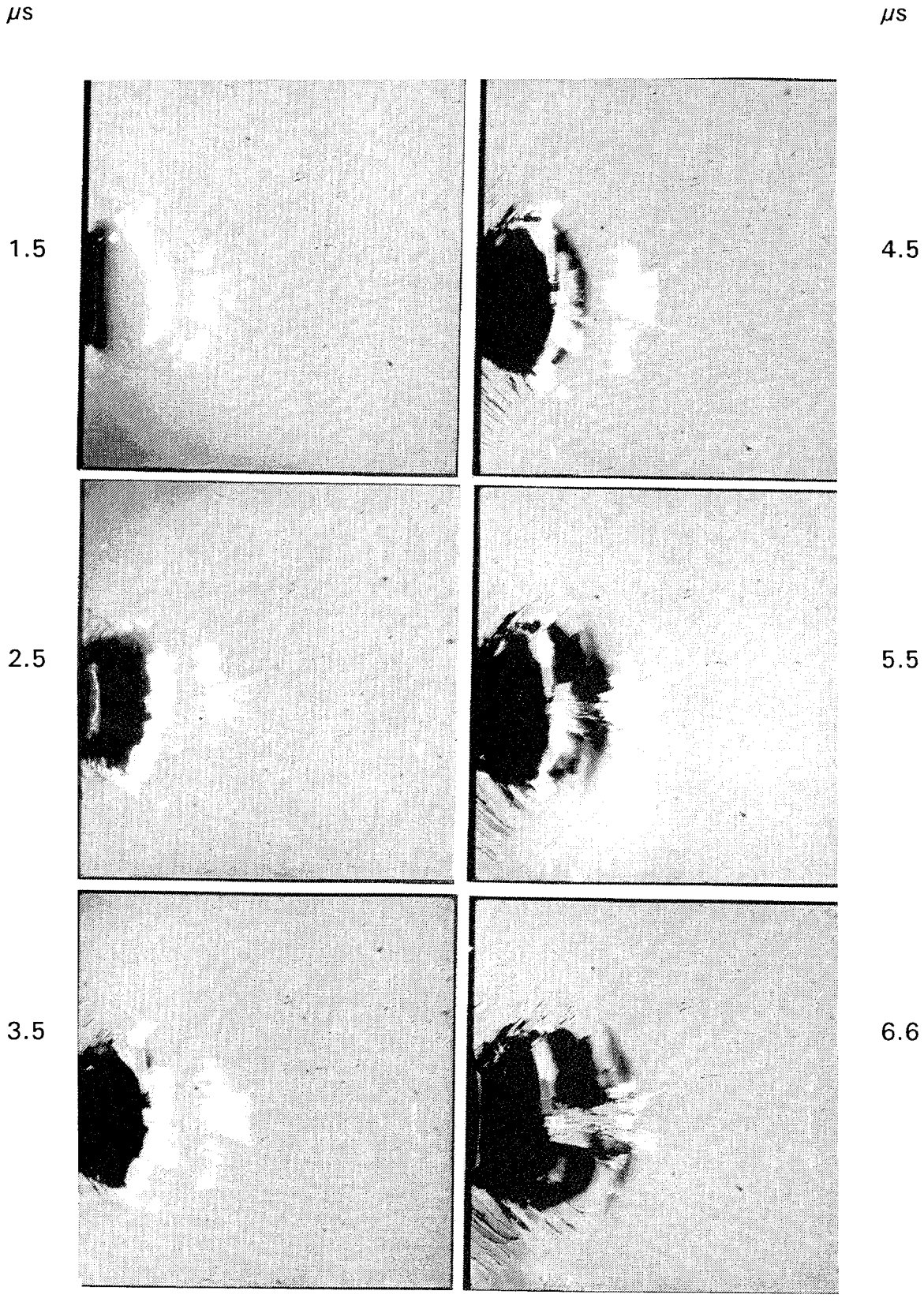


Figure 14.14 High-speed photographs of shot no. 10137

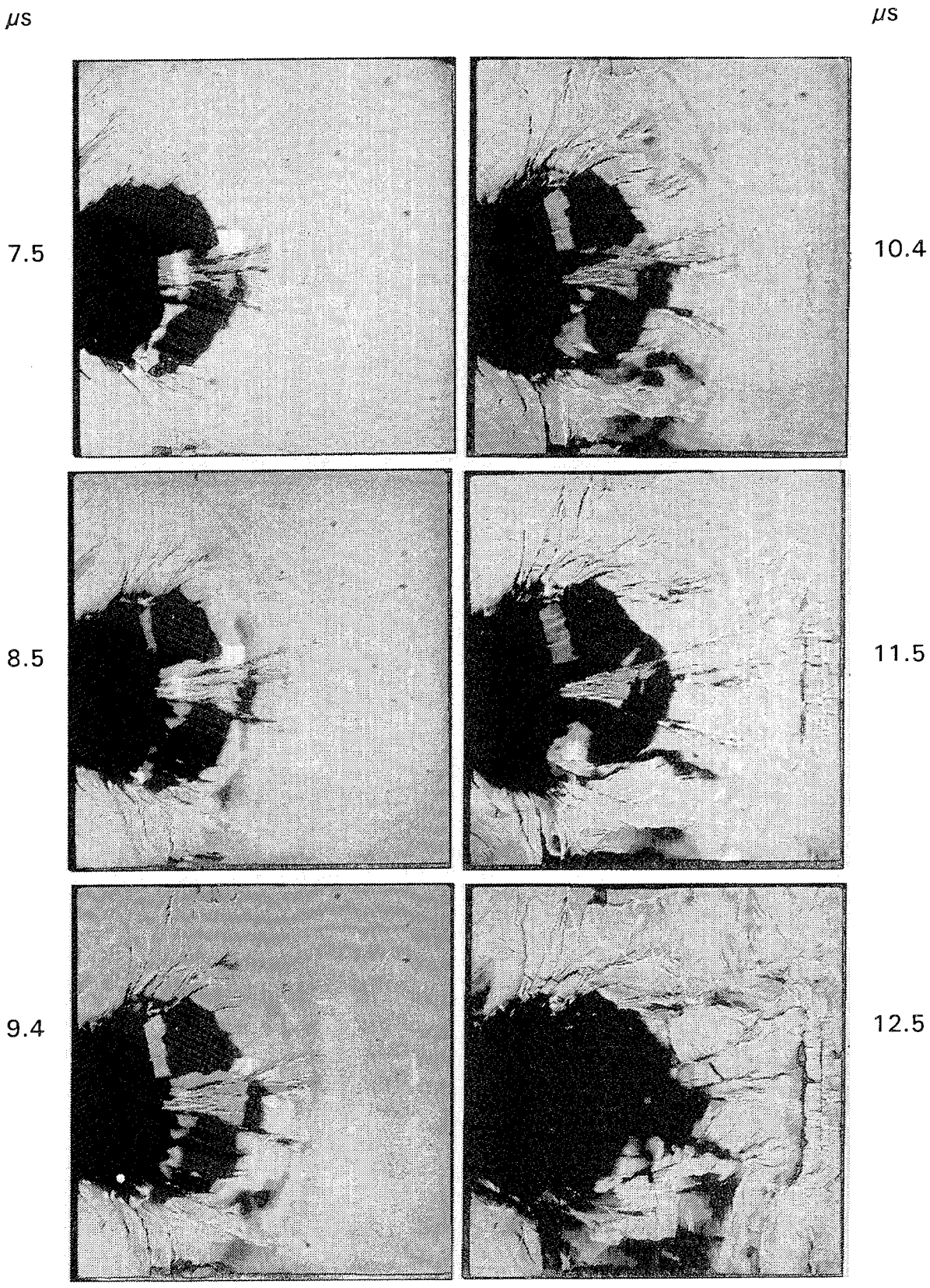


Figure 14.14 High-speed photographs of shot no. 10137

Shot No. 10325 (SiC, v_p = 185 m/s)

The fracture propagation in SiC after impact at 185 m/s is shown in Figure 14.16. In this experiment the specimen exhibits secondary cracks most clearly. The mean velocities of the secondary cracks are in the range from 3240 m/s to 4180 m/s. The cone cracks branch out frequently and grow at mean velocities of 5360 m/s (upper) and 5410 m/s (lower). Three main fractures with fuzzy edges have developed between the cone cracks. The mean propagation velocities are v_{C1} = 5780 m/s, v_{C2} = 8270 m/s and v_{C3} = 8220 m/s (Fig. 14.15). In this case v_{C3} means the propagation velocity of the bundle of cracks in horizontal direction and does not mean the velocity of the single cracks that form the crack bundle. The last three photographs show spall zones near the rear edge of the specimen.

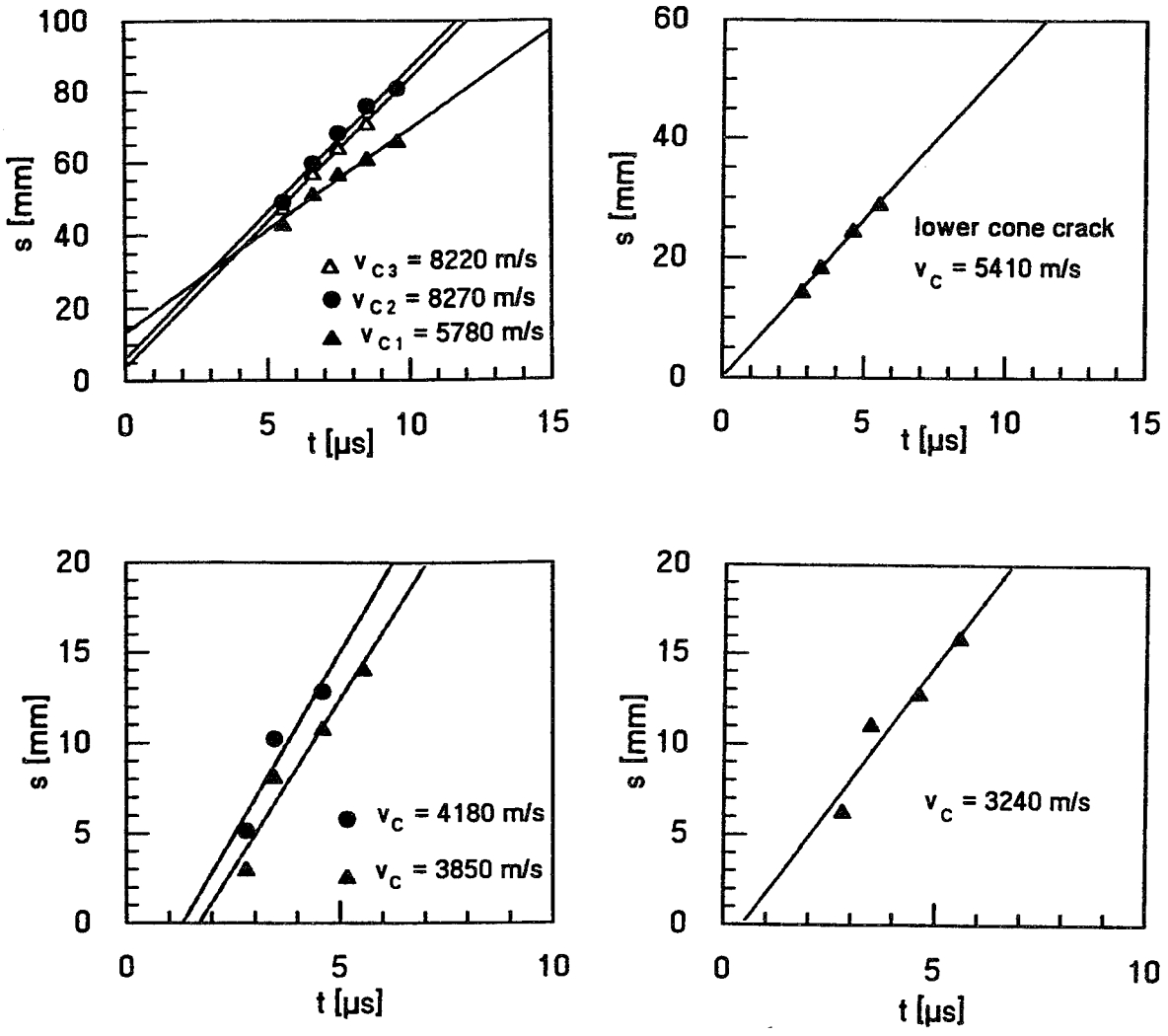


Figure 14.15 Path-time plots of shot no. 10325

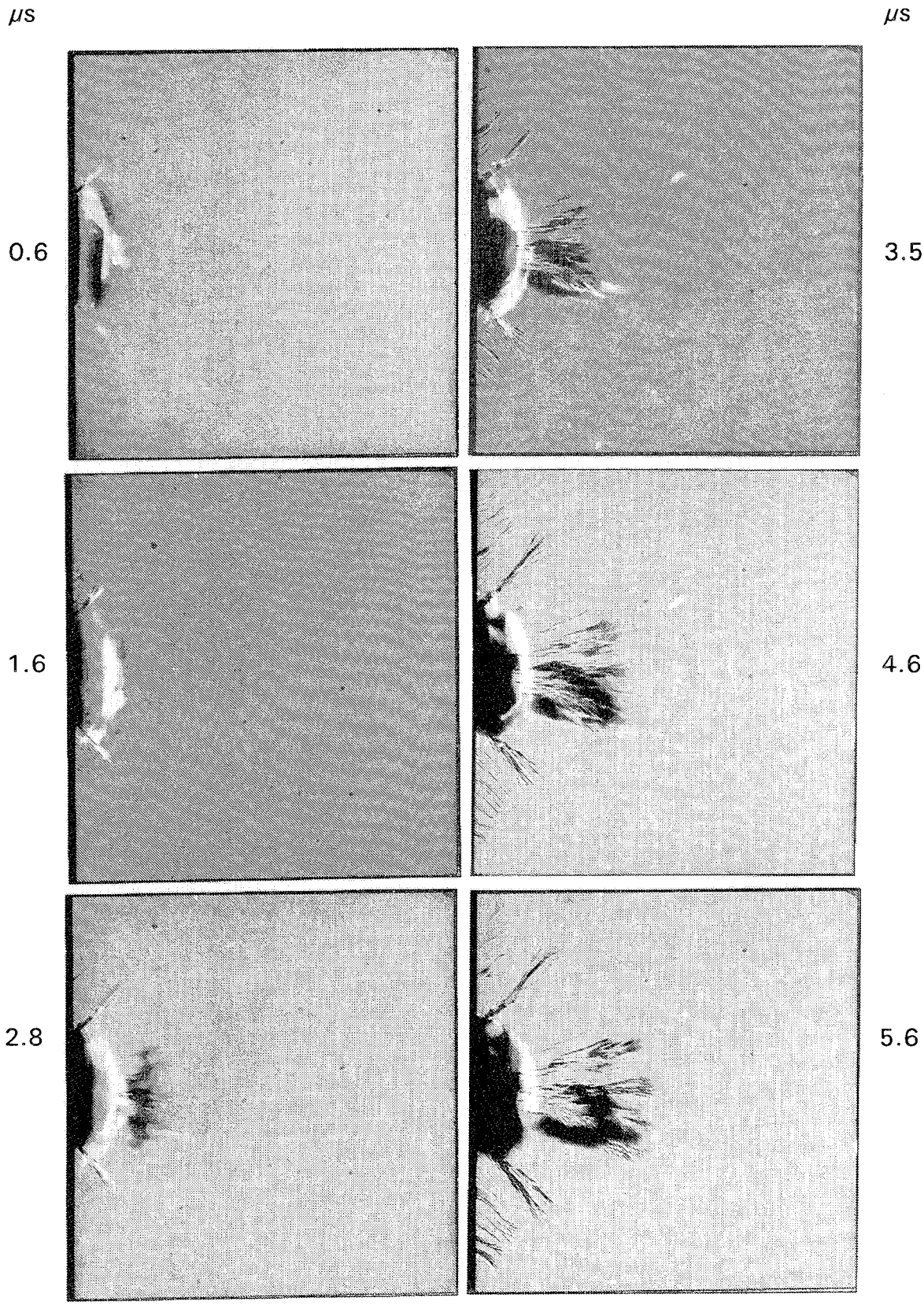


Figure 14.16 High-speed photographs of shot no. 10325

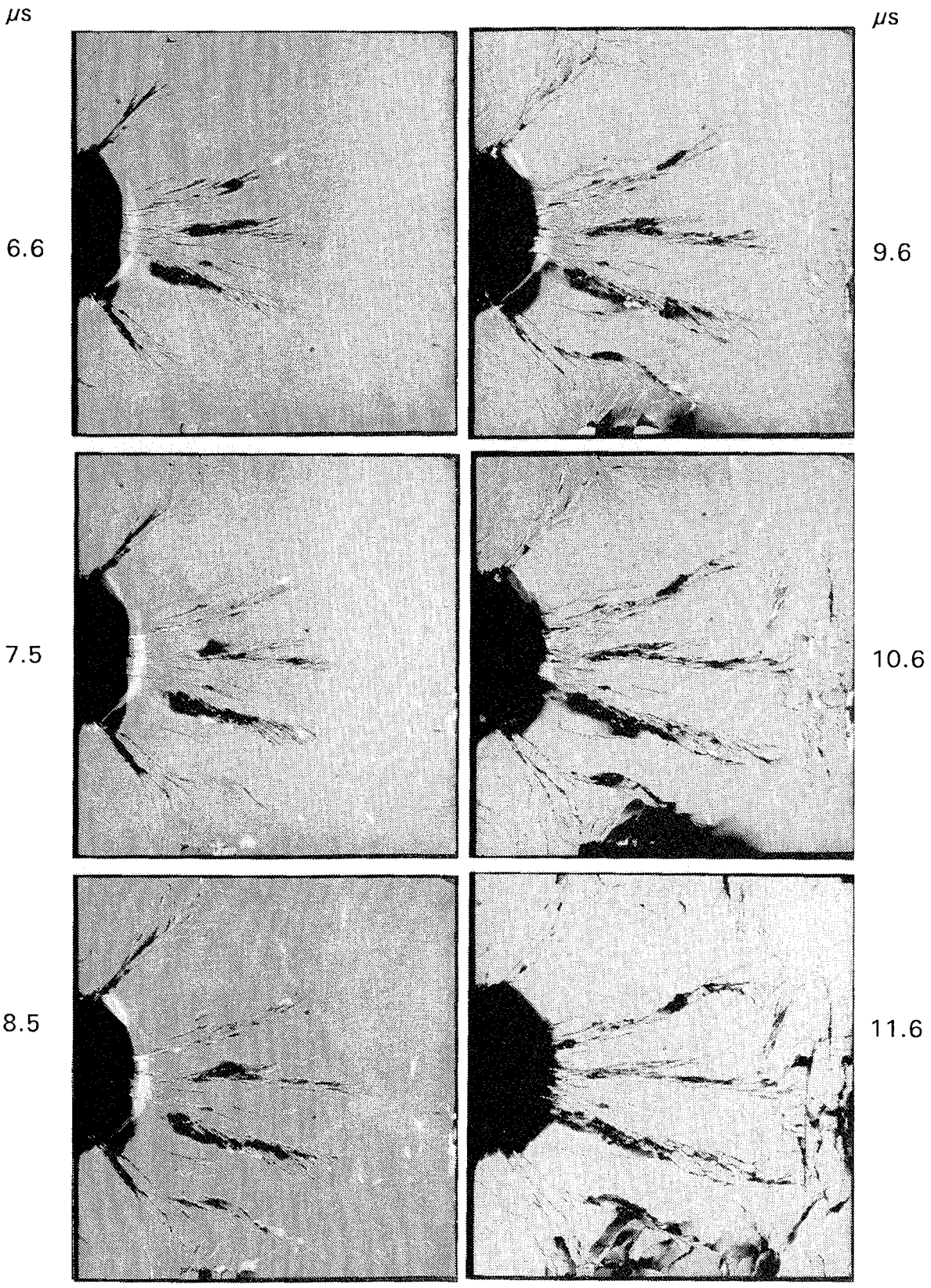


Figure 14.16 High-speed photographs of shot no. 10325

Shot No. 10116 (SiC, v_p = 220 m/s)

The photographs in Figure 14.17 show the destruction of a SiC plate after impact at 220 m/s over a period of 8 μs. Already a few microseconds after impact a dense front of radial cracks can be observed. Two main fractures develop in the course of the next microseconds, which consist of many short cracks with fuzzy edges. These cracks are generated successively and close together. The main fracture path in the center of the specimen propagates at a mean velocity of 9400 m/s and determines the damage velocity in horizontal direction (Fig. 14.20). The term damage velocity is used here, because the velocity of a fracture front is considered and not the velocity of a single, continuously growing crack.

Shot No. 10359 (SiC, v_p = 370 m/s)

The destruction of the SiC specimen after impact at 370 m/s is illustrated in Figure 14.18. A dense fracture front which consists of many short cracks with fuzzy edges is observed during the first microseconds. Single fractures can be distinguished from photograph 4. However, it is hardly possible to measure the propagation velocities of the different fractures because the crack tips can not be recognized clearly. Additionally, the edges of cracks that have been formed during the interval of time between two photographs are shifted with respect to the positions of the crack edges on the previous photograph. From the observation of the surface it is not possible to distinguish whether the crack surface has turned in the interior of the plate or whether a new crack has been generated close to the initial crack. Therefore, the whole fracture propagation is characterized by the damage velocity v_D = 9250 m/s in this case (Fig. 14.21).

Shot No. 10358 (SiC, v_p = 446 m/s)

With this experiment the projectile did not hit the edge of the specimen properly. Therefore, it was not evaluated.

Shot No. 10362 (SiC, v_p = 513 m/s)

Six selected photographs (Figure 14.19) show the damage of the SiC specimen. A front of many radial cracks with fuzzy edges grows at high velocity into the specimen. It is not possible to evaluate single cracks. The mean velocity of the fracture front was v_D = 10090 m/s (Fig. 14.22).

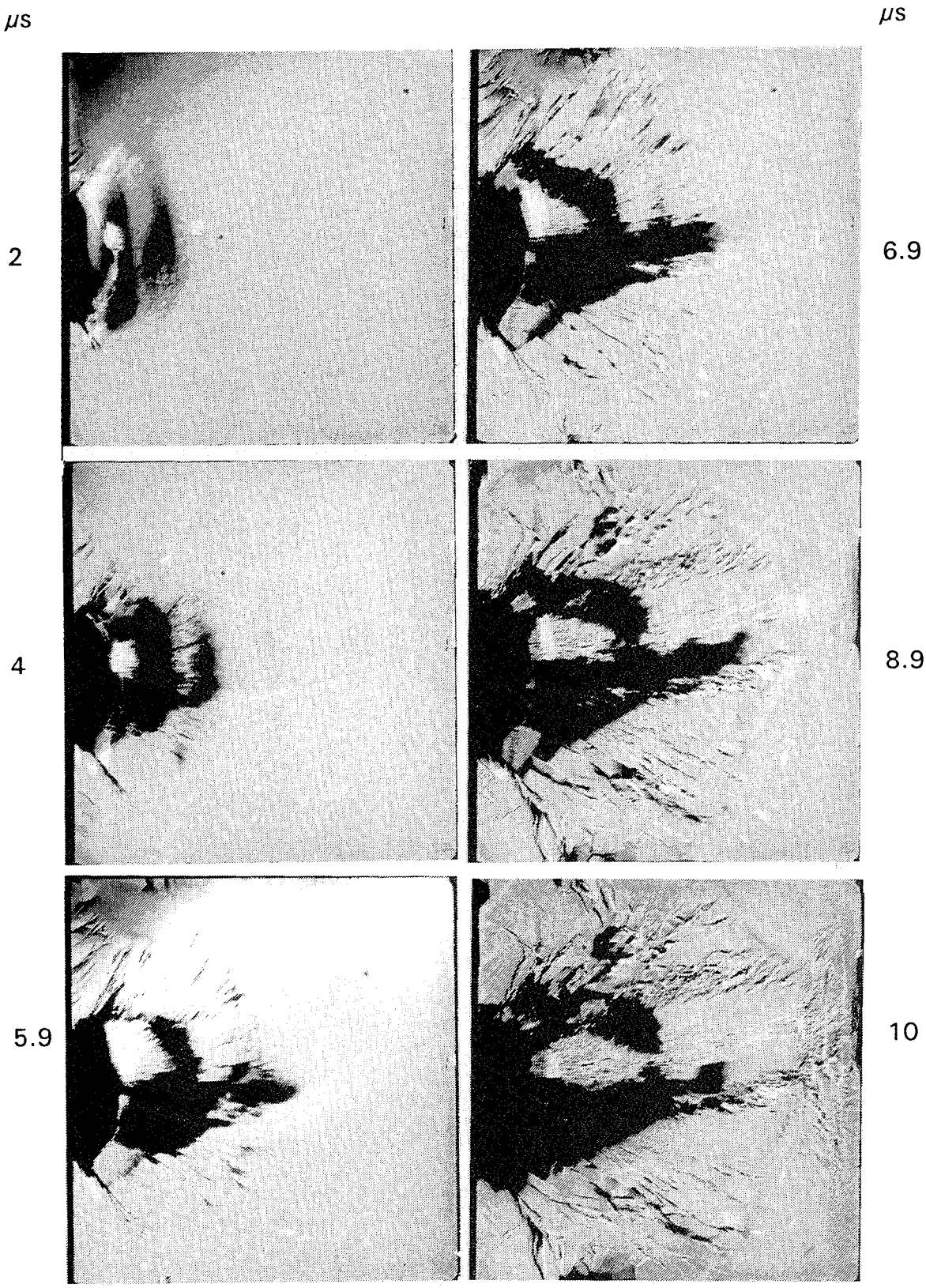


Figure 14.17 High-speed photographs of shot no. 10116

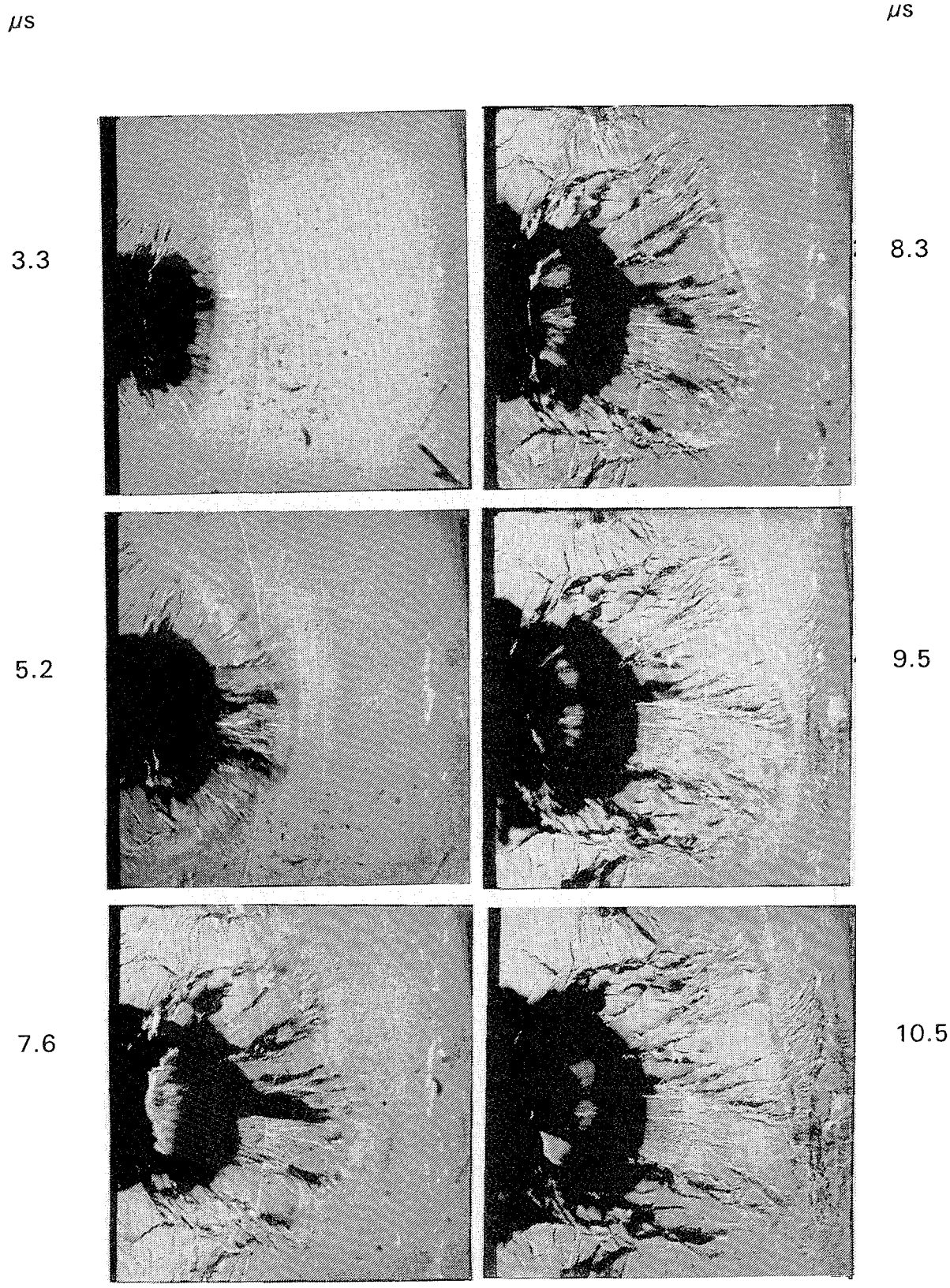


Figure 14.18 High-speed photographs of shot no. 10359

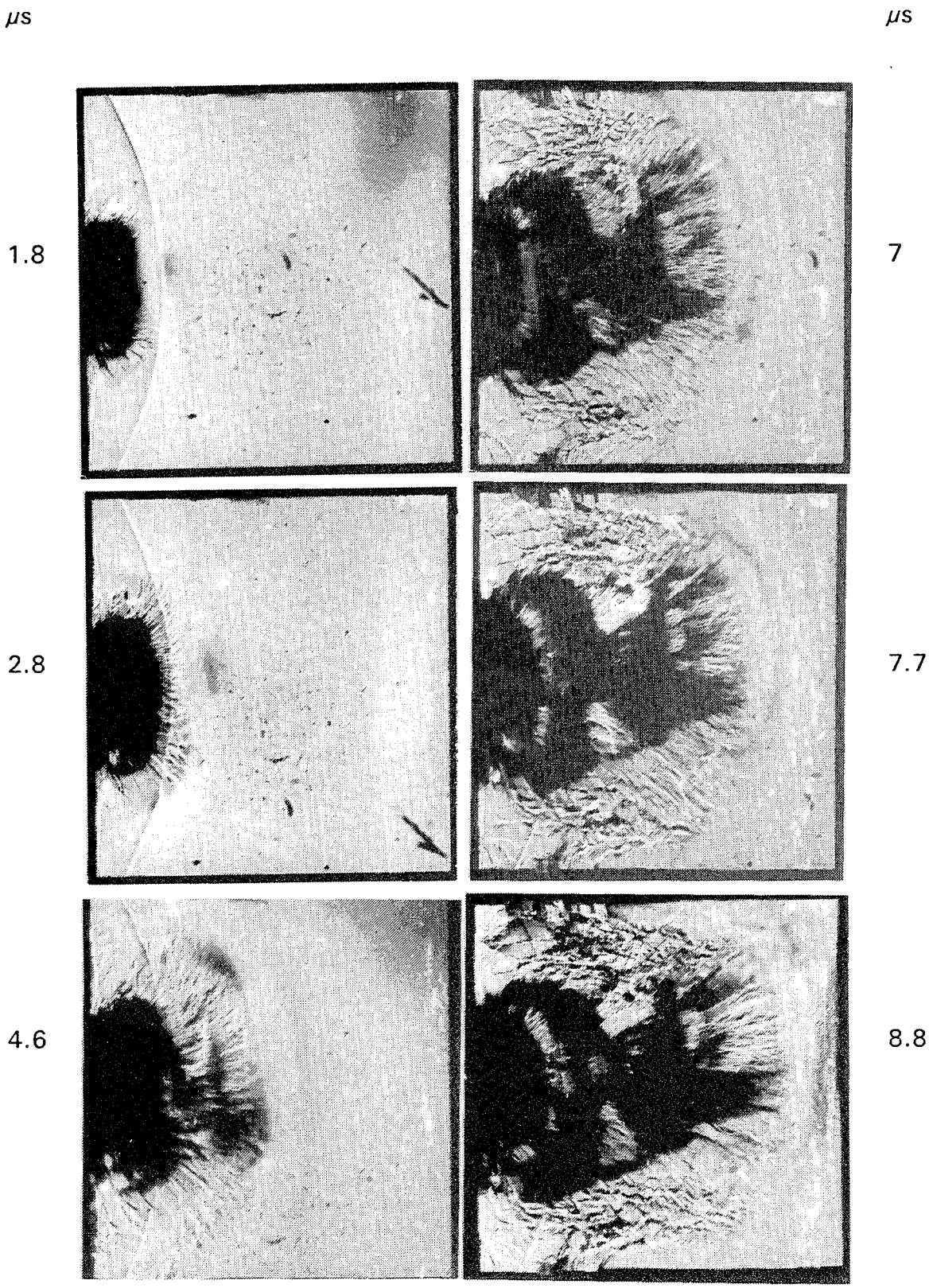


Figure 14.19 High-speed photographs of shot no. 10362

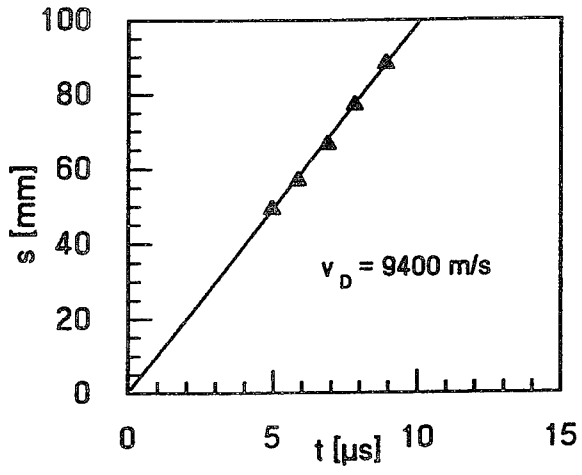


Figure 14.20 Path-time plot of shot no. 10116

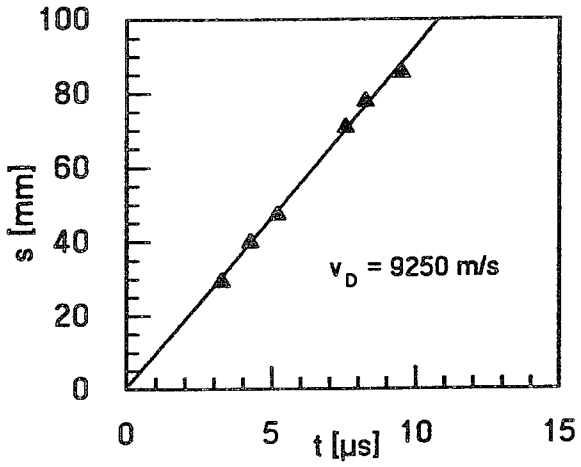


Figure 14.21 Path-time plot of shot no. 10359

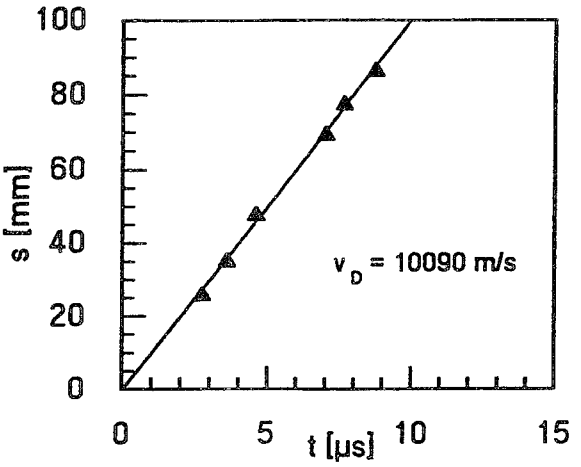


Figure 14.22 Path-time plot of shot no. 10362

Shot No. 10142 (SiC, v_P = 670 m/s)

Figure 14.25 shows the specimen after impact at 670 m/s. The high intensity of the stress waves causes a strong deformation of the surface so that the fracture propagation is vastly superimposed by the black area. With this experiment and all other shots at higher impact velocities sparks were generated at the impacted edge of the specimen. The light from these glowing particles is seen on the photographs in the form of bright, curved stripes. The mean velocity of the damage front was 10260 m/s (Fig. 14.23). The evaluation of the cracks which can be seen in the lower half of the specimen resulted in fracture velocities between 6700 m/s and 6800 m/s.

Shot No. 10147 (SiC, v_P = 1040 m/s)

At the impact velocity of 1040 m/s the fracture propagation is superimposed by the impact flash and the black area first (see Fig. 14.26). After a few microseconds a dense front of cracks with fuzzy edges can be recognized. Single radial cracks occur at big angles against the shotline. The density of the fracture front decreases rapidly. The damage velocity was 11150 m/s (Fig. 14.24).

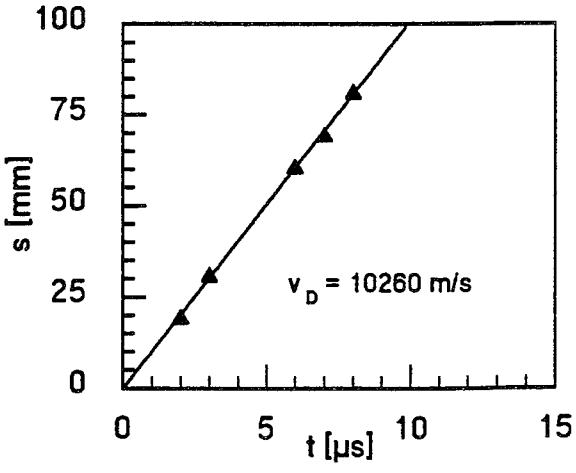


Figure 14.23 Path time plot of shot no. 10142

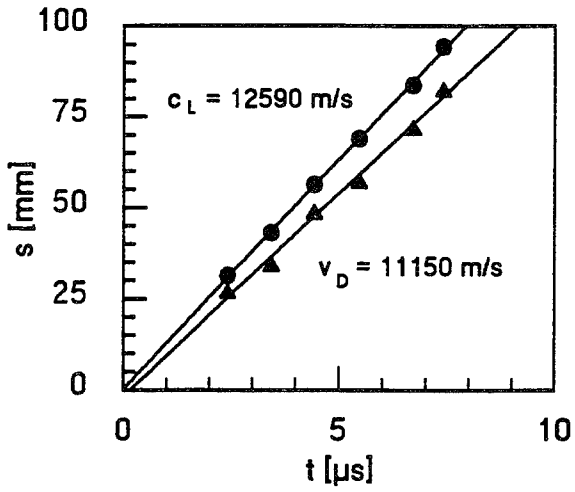


Figure 14.24 Path-time plot of shot no. 10147

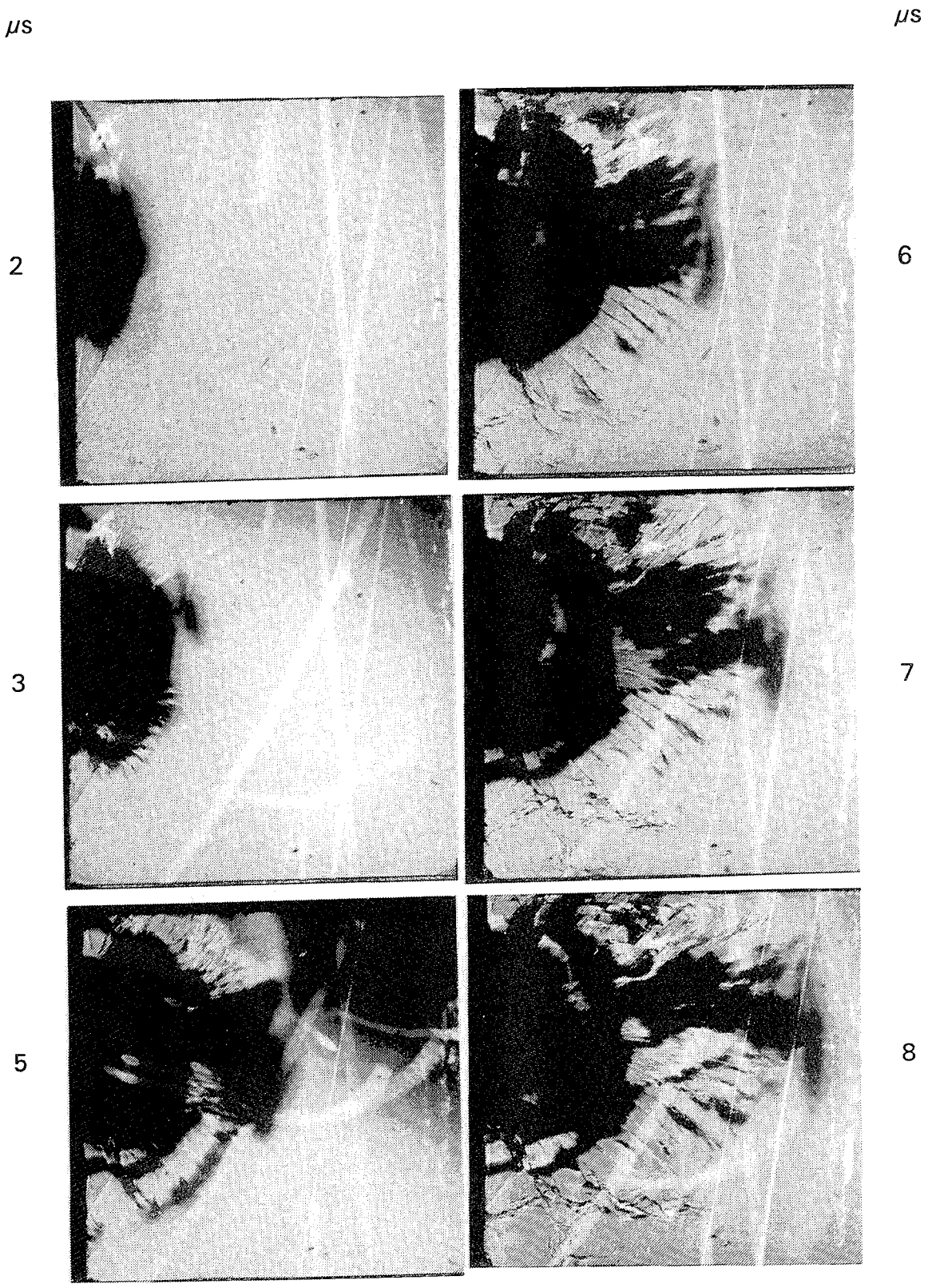


Figure 14.25 High-speed photographs of shot no. 10142

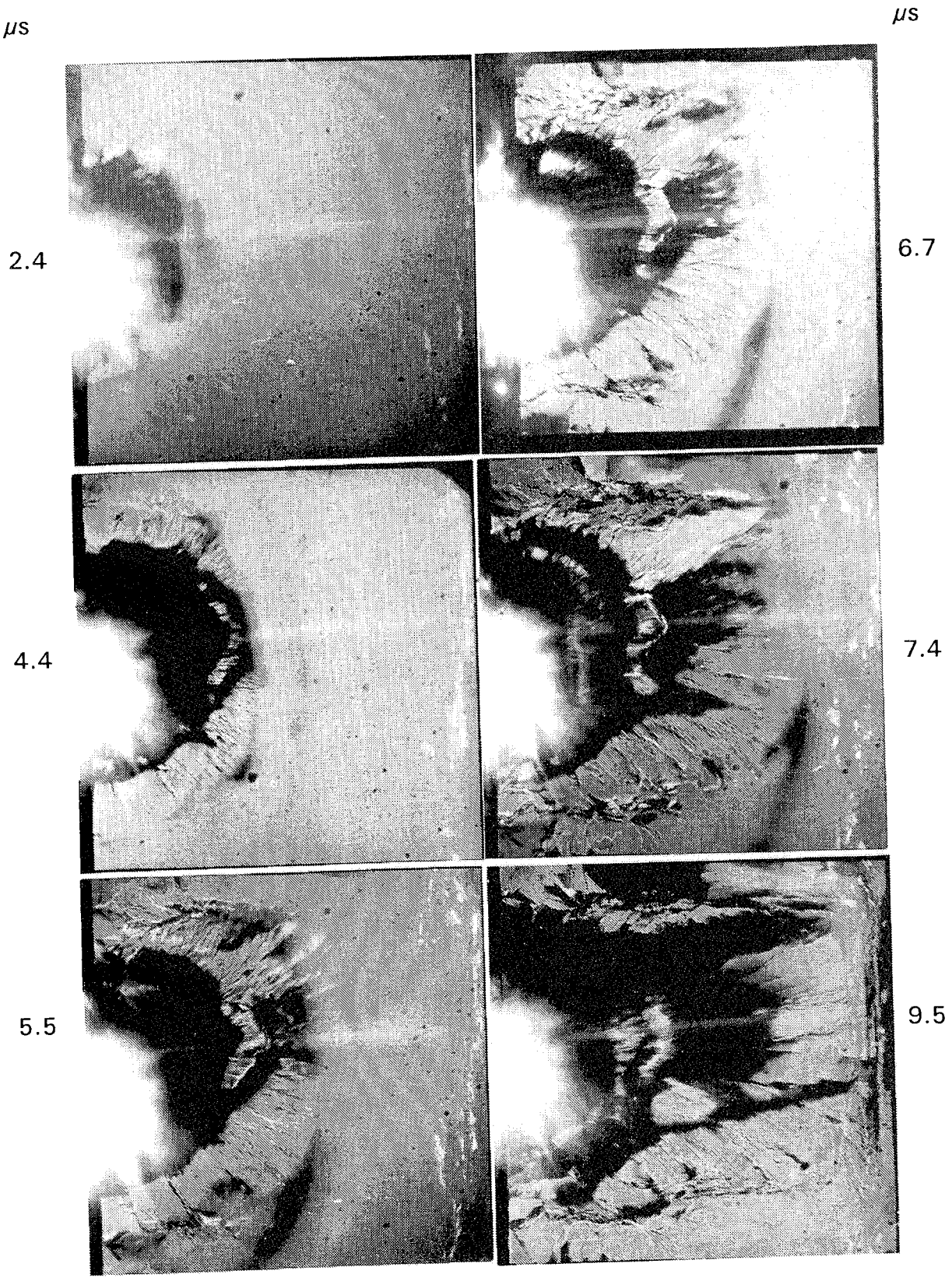


Figure 14.26 High-speed photographs of shot no. 10147

14.2 Experiments with TiB_2

Shot No. 10108 (TiB_2, v_P = 31 m/s)

The fracture propagation in TiB_2 after impact at 31 m/s is illustrated in Figure 14.27. The lower cone crack can be recognized first and evaluated on four photographs. The mean velocity of this crack was v_C = 4850 m/s (Fig. 14.33). The other cracks were only visible when they had reached the edge of the specimen. The concentric rings on the surface are due to the polishing process. Similar to the experiments with SiC, the specimens could be rebuilt from the fragments at impact velocities below 90 m/s. The reassembled ceramic plate of this experiment is shown in Figure 14.30.

Shot No. 10110 (TiB_2, v_P = 54 m/s)

Figure 14.28 shows six high-speed photographs of a TiB_2 specimen which was impacted at 54 m/s. The cone cracks can be seen first and the propagation velocity of the lower cone crack is 4950 m/s. About 10 to 15 radial cracks develop in the primary fracture zone. The edges of the cracks appear as fine sharp lines and a portion of them cannot be seen over their full length. Some of the cracks or visible parts of cracks cannot be associated with cracks that have grown from the impacted edge. The damage velocity is determined by the velocity of the main fracture MF which grows just below the center of the plate (see Fig. 14.34) at a mean velocity of v_D = 5600 m/s. The reassembled specimen (Fig. 14.31) exhibits all the cracks seen on the high-speed photographs. It is remarkable that only a few main cracks pierce the specimen whereas most of the primary cracks observed on the high-speed photographs do not extend to the back side of the ceramic plate.

Shot No. 10130 (TiB_2, v_P = 62 m/s)

A TiB_2 specimen after impact at 62 m/s is shown in Figure 14.29. One crack (R1) with a sharp and smooth edge which includes a big angle with the shot line propagates at v_C = 3840 m/s into the specimen. A second crack (R2) proceeds on a curve first and then straight ahead at a mean velocity of v_C = 6070 m/s (Fig. 14.35). This crack exhibits sharp edges in the beginning and fuzzy edges at a later time. An examination of the crack surfaces did not show any significant difference in the structure of the part where the edge appeared sharp and the part which corresponds to the fuzzy edges. The fracture front in the lower half of the specimen propagated at 6680 m/s. The reassembled specimen is shown in Figure 14.32.

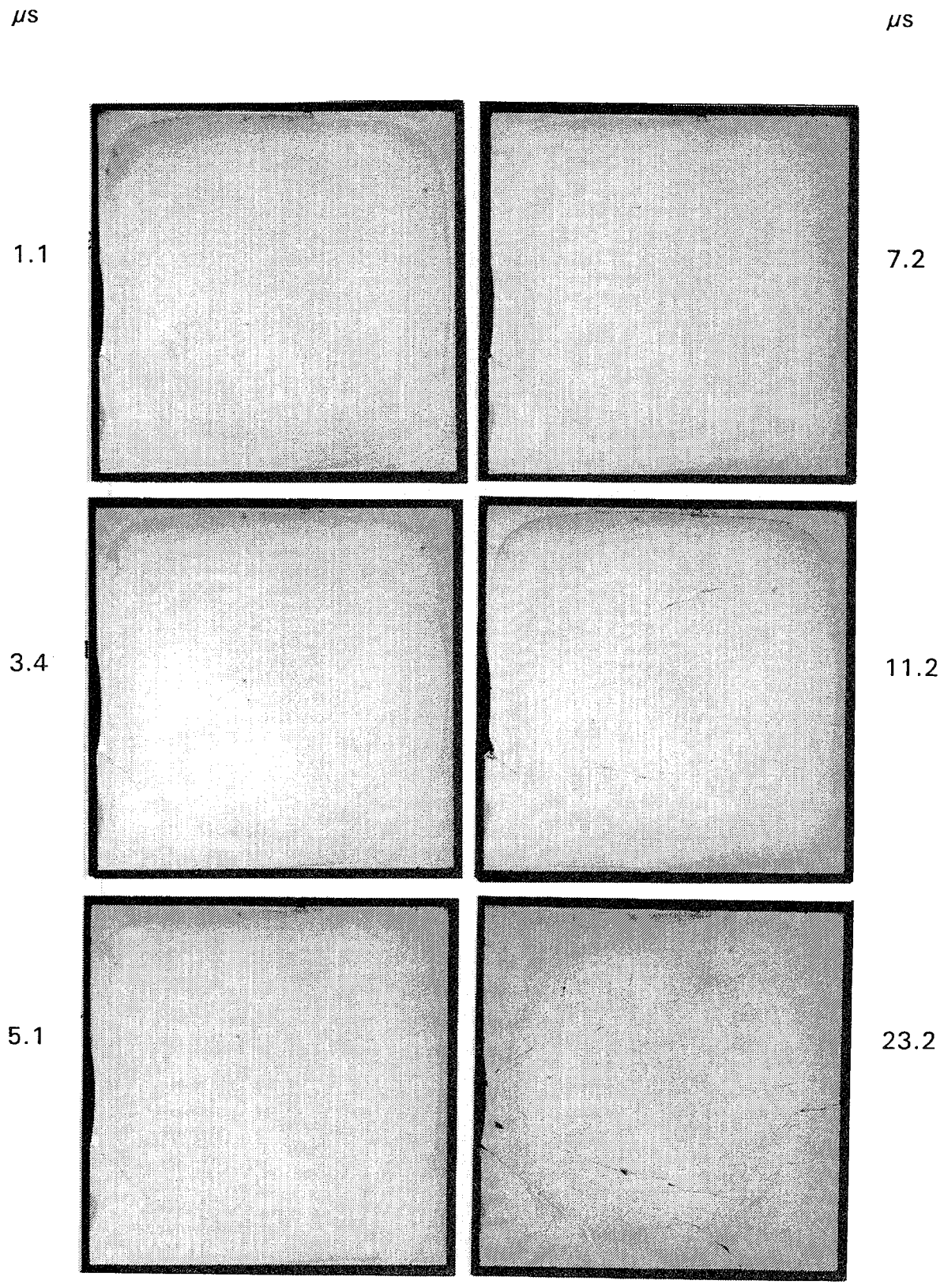


Figure 14.27 High-speed photographs of shot no. 10108

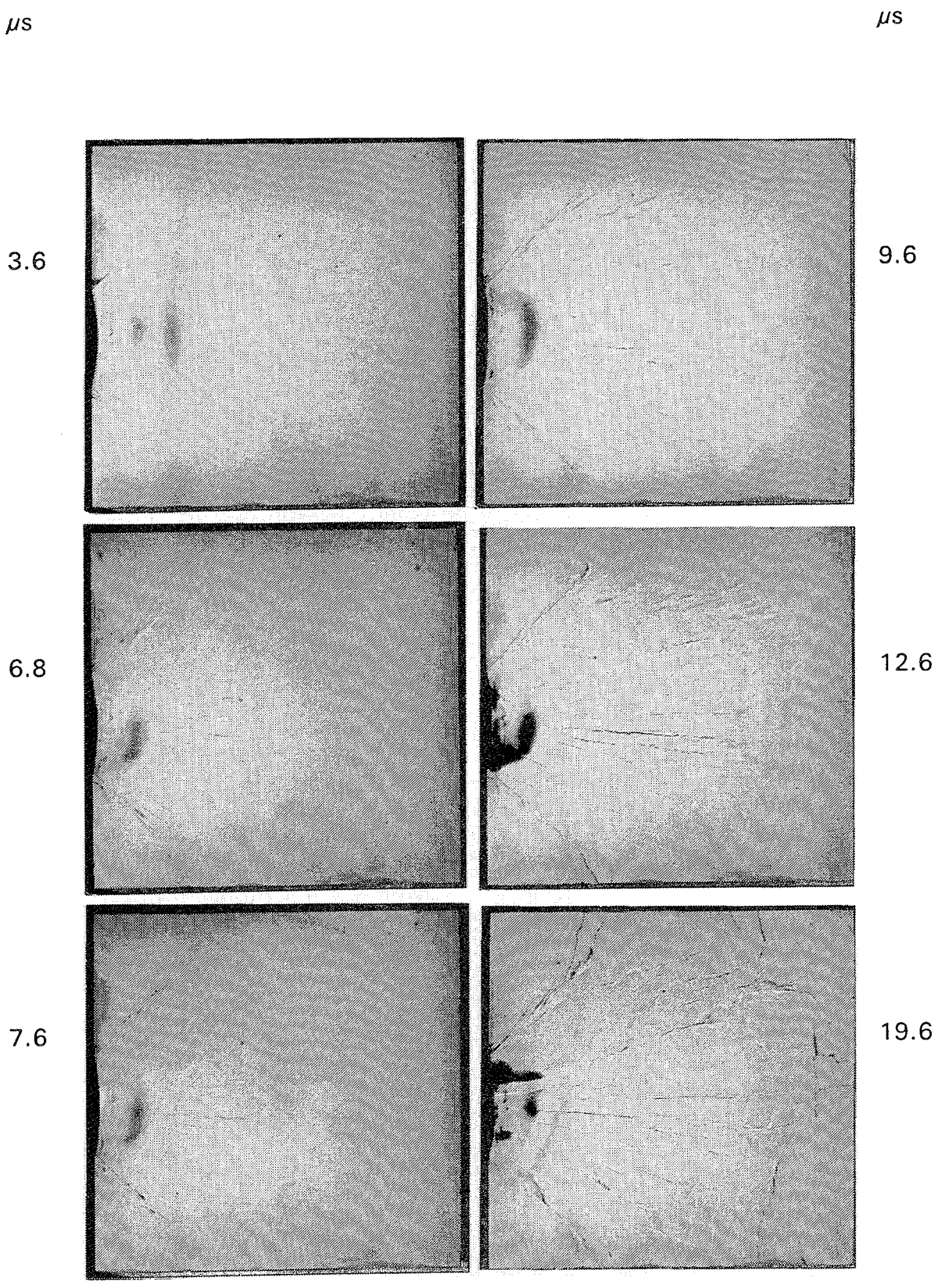


Figure 14.28 High-speed photographs of shot no. 10110

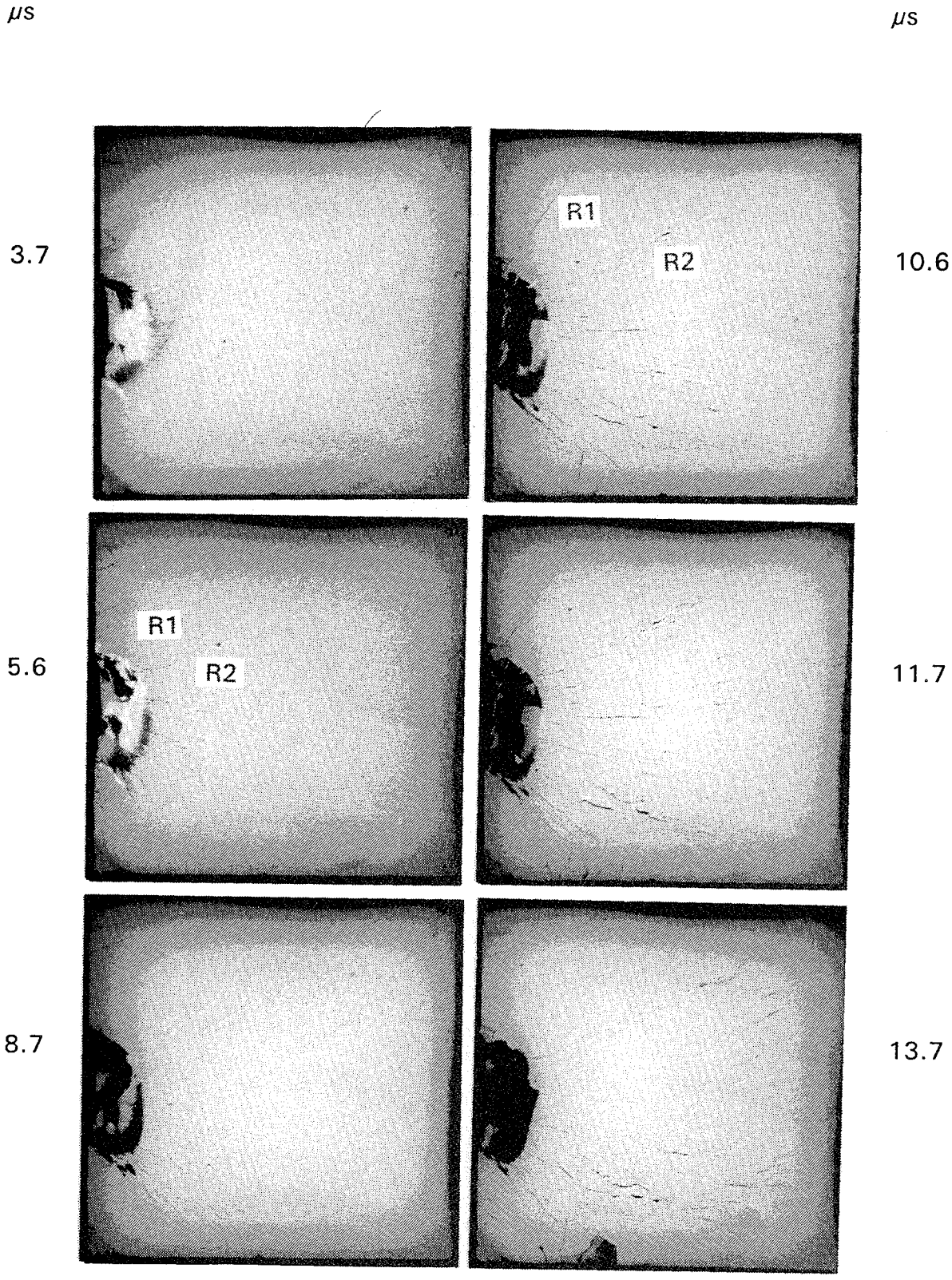


Figure 14.29 High-speed photographs of shot no. 10130

lower
cone crack



Figure 14.30 Reassembled specimen of shot no. 10108

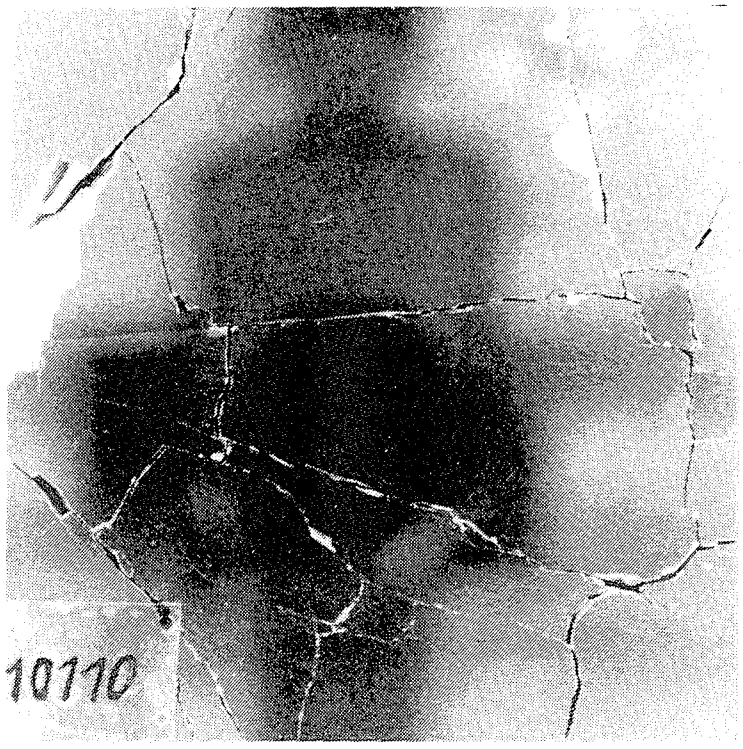


Figure 14.31 Reassembled specimen of shot no. 10110

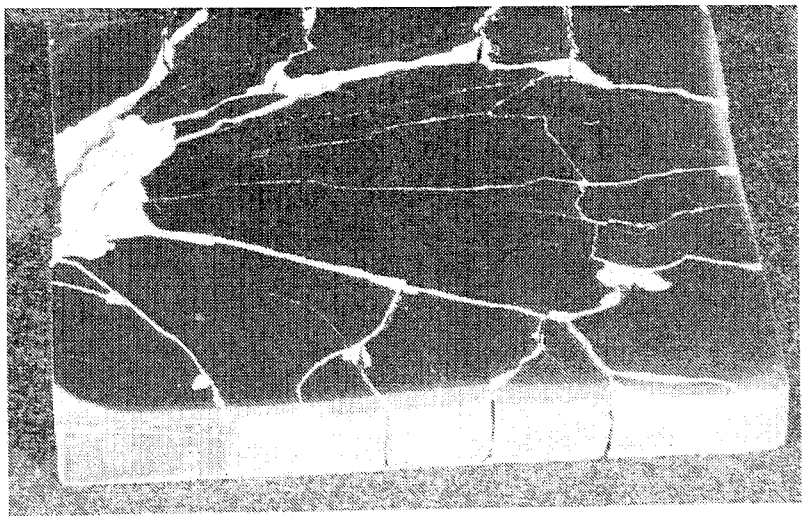


Figure 14.32 Reassembled specimen of shot no. 10130

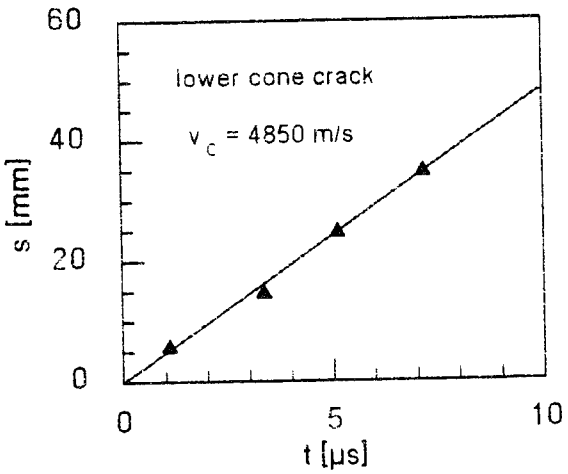


Figure 14.33 Shot no. 10108

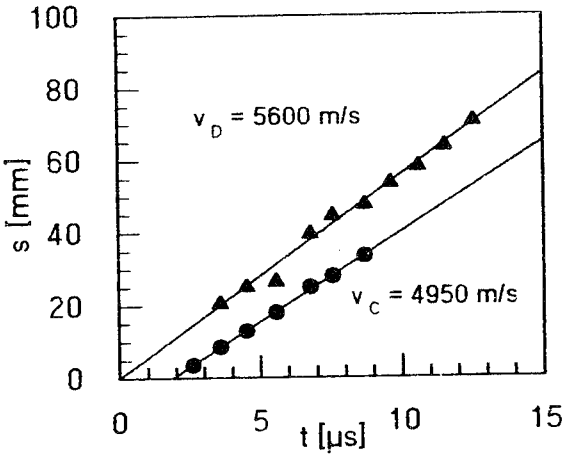
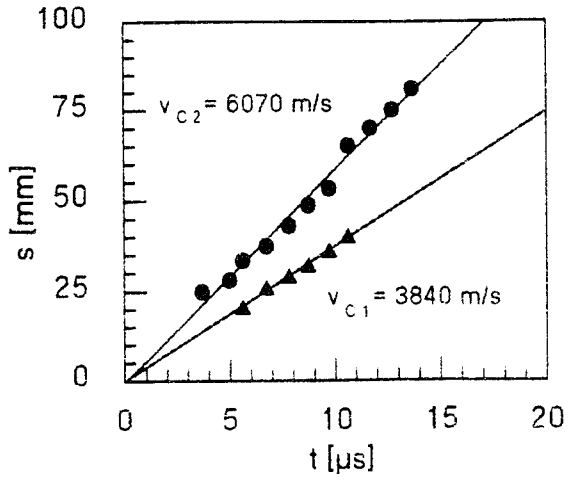


Figure 14.34 Shot no. 10110



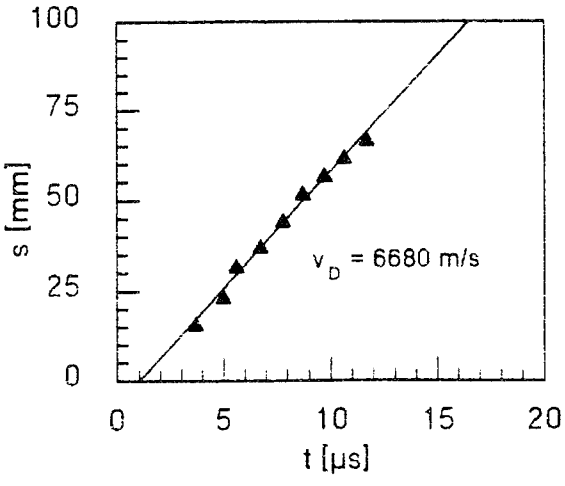


Figure 14.35 Path-time plots of shot no. 10130

Shot No. 10119 (TiB_2, v_P = 70 m/s)

A field of cracks or visible edges of cracks develops between the two cone cracks in a TiB_2 specimen which was impacted at 70 m/s (Fig. 14.36). Most of the cracks do not pierce the specimen as the photograph of the reassembled ceramic plate (Fig. 14.39) shows. In this experiment the lower cone crack propagated at 4240 m/s. The damage velocity v_D (velocity of the front of the fracture field) was 7290 m/s (Fig. 14.41).

Shot No. 10109 (TiB_2, v_P = 85 m/s)

Figure 14.37 shows the destruction of a TiB_2 specimen after impact at 85 m/s. The front of the crack field propagates with a mean velocity of 7470 m/s (Fig. 14.43), the upper cone crack grows at 4870 m/s. One continuously growing crack with a sharp edge (R 3) was observed which could be evaluated. The crack velocity v_C was 4080 m/s (Fig. 14.43). After the reflection of the stress wave at the rear edge of the specimen a spall zone is observed at a distance of 1.1 cm from this edge. A few secondary cracks were observed in this experiment and in some of the other experiments at low impact velocities. The formation of secondary fracture zones, as observed with glasses and in a few cases with SiC, was never observed with TiB_2. The photograph of the reassembled specimen (Fig. 14.40) shows that much more of radial cracks have pierced the ceramic plate compared to the shots at lower velocities. The inspection of the crack surfaces confirmed that an unambiguous correlation between the appearance of the crack edges at the surface of the plate and the structure of the crack surfaces cannot be established. Only the fractures parallel to the polished surface of the plates exhibit smooth surfaces.

Shot No. 10326 (TiB_2, v_P = 108 m/s)

A dense, homogeneous field of cracks developed after the impact at 108 m/s in TiB_2 specimen (see Fig. 14.38). The front of the crack field propagated at a mean velocity of 8370 m/s (Fig. 14.42).

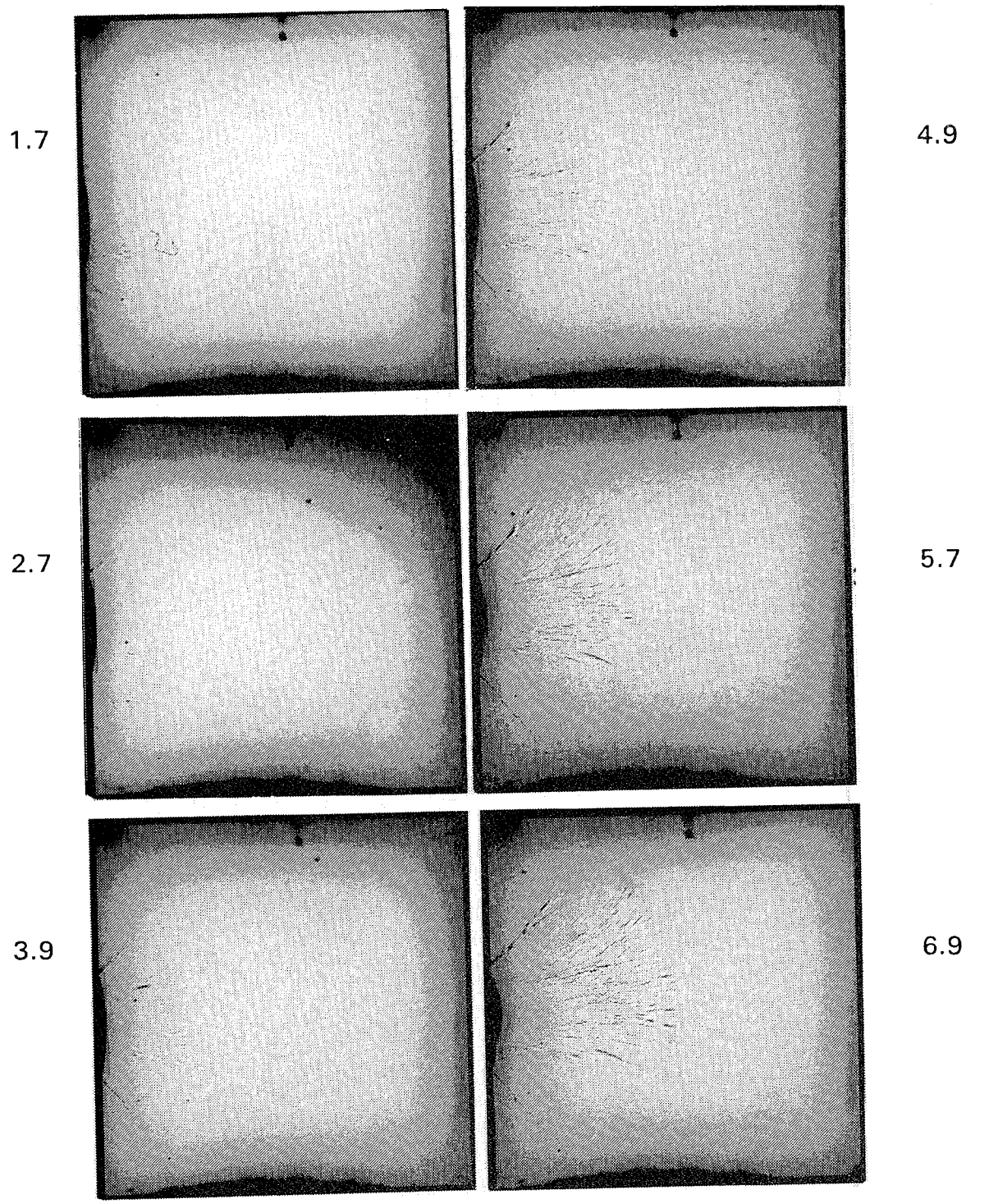


Figure 14.36 High-speed photographs of shot no. 10119

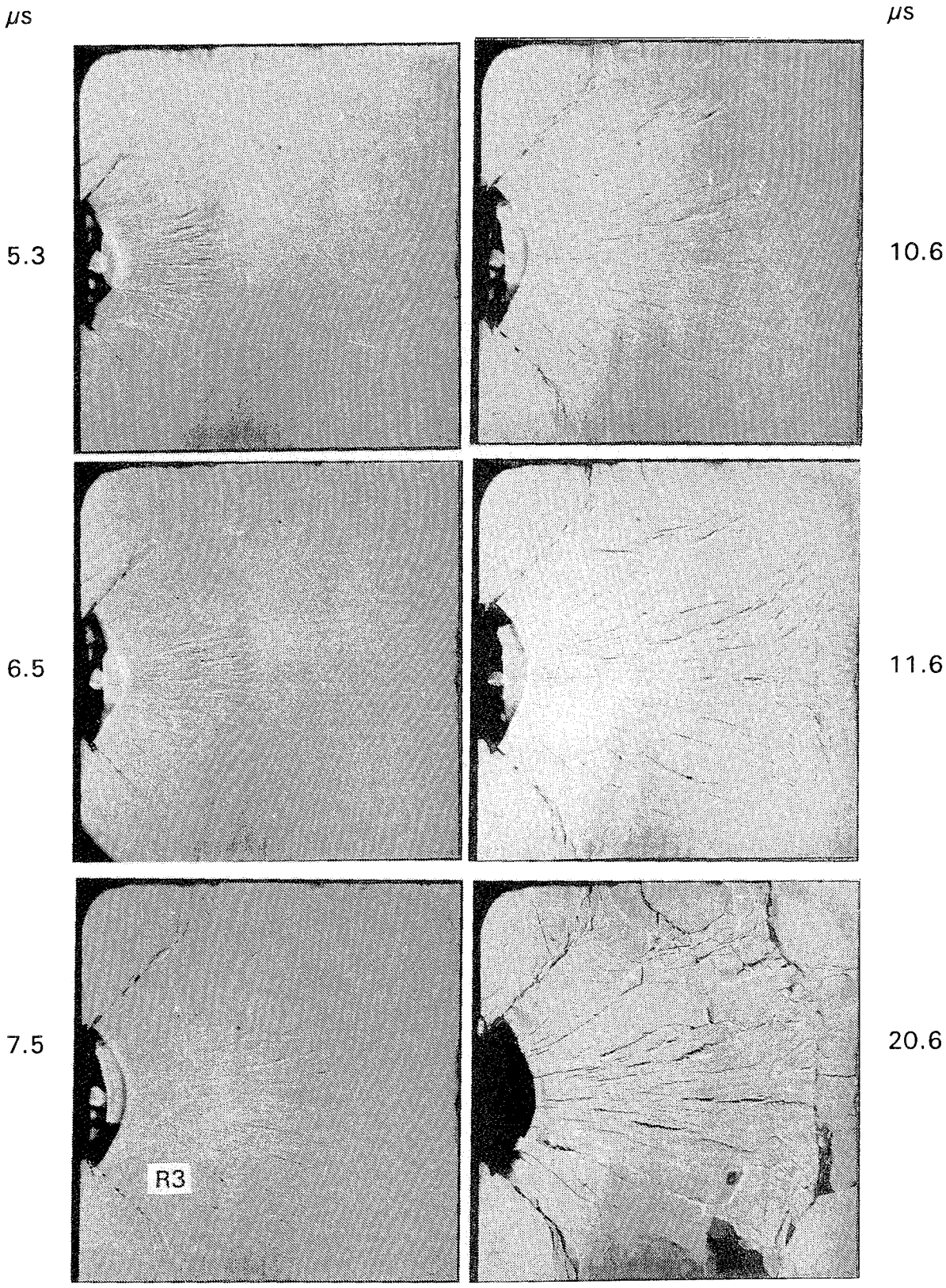


Figure 14.37 High-speed photographs of shot no. 10109

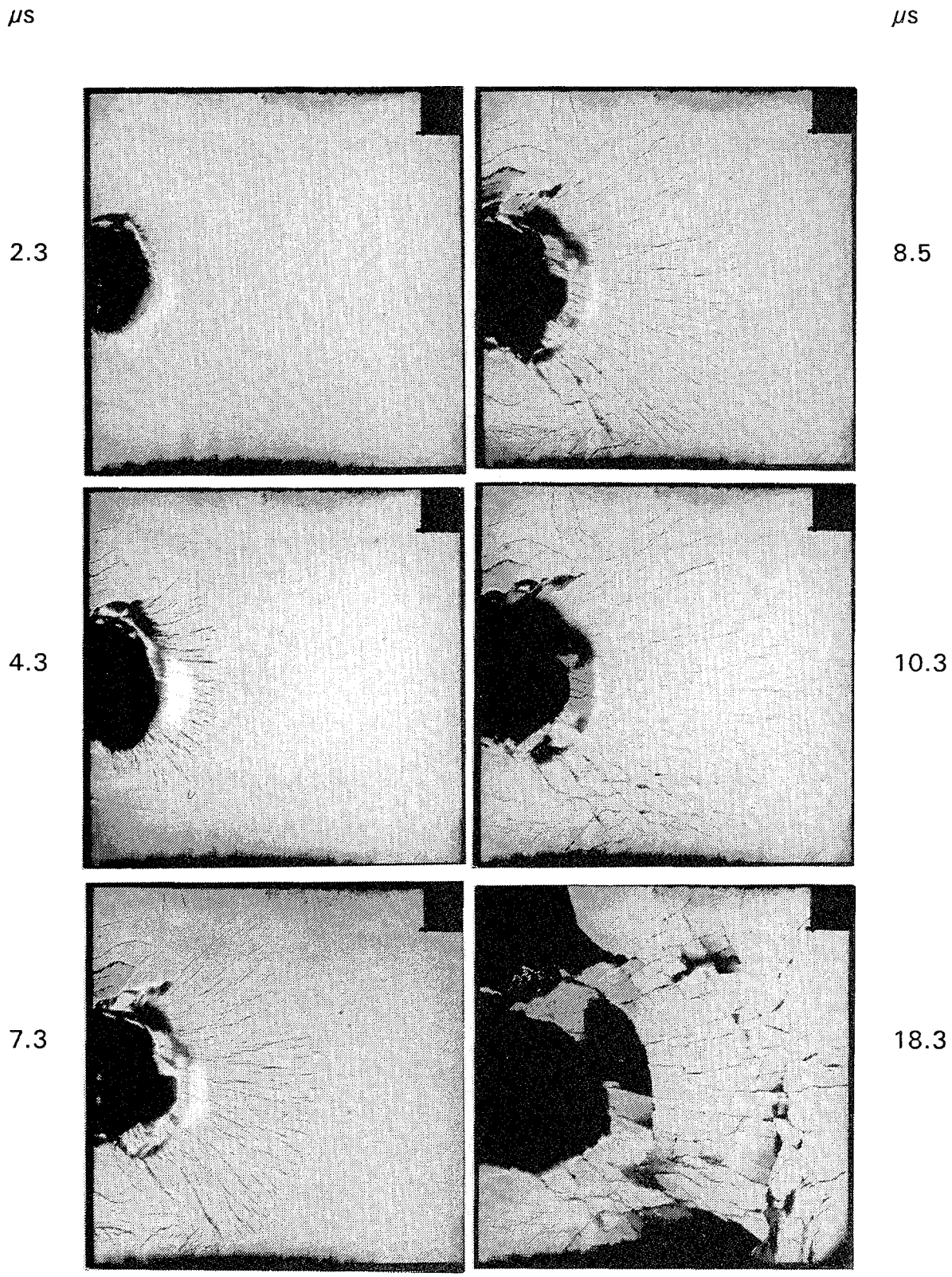


Figure 14.38 High-speed photographs of shot no. 10326

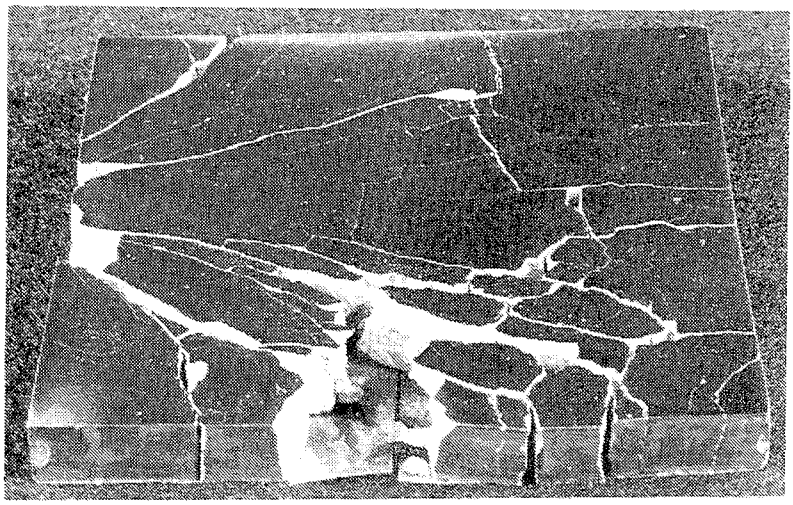


Figure 14.39 Reassembled specimen of shot no. 10119

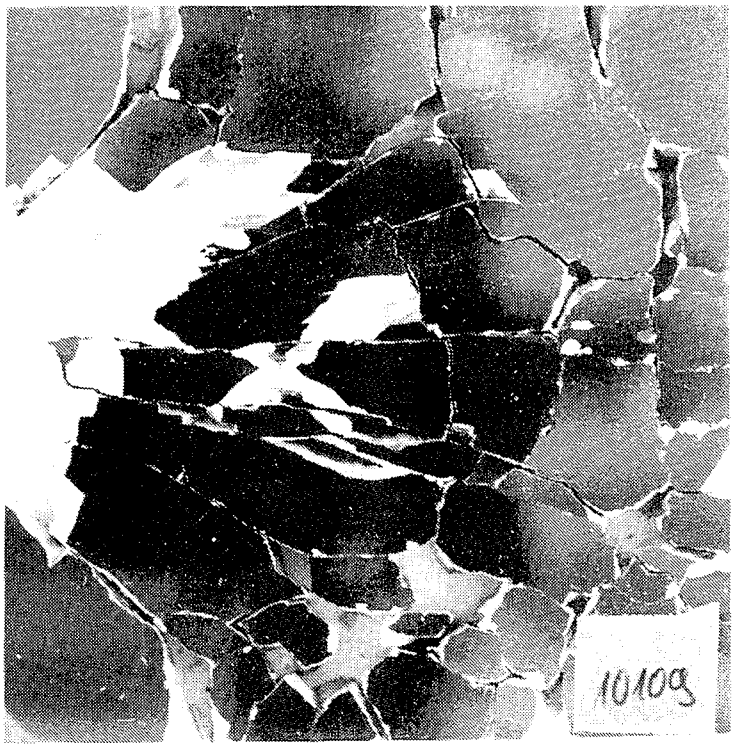


Figure 14.40 Reassembled specimen of shot no. 10109

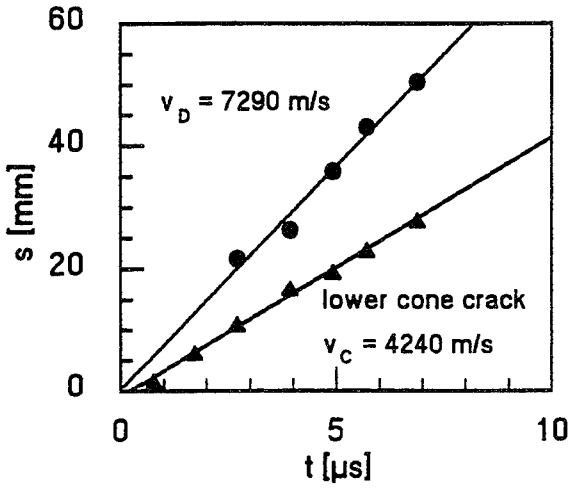


Figure 14.41 Shot no. 10119

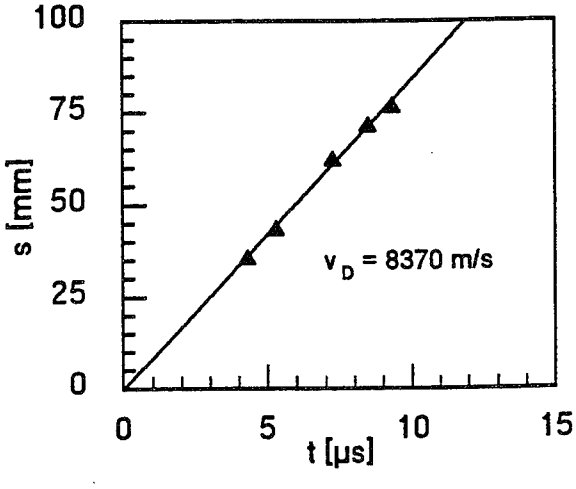
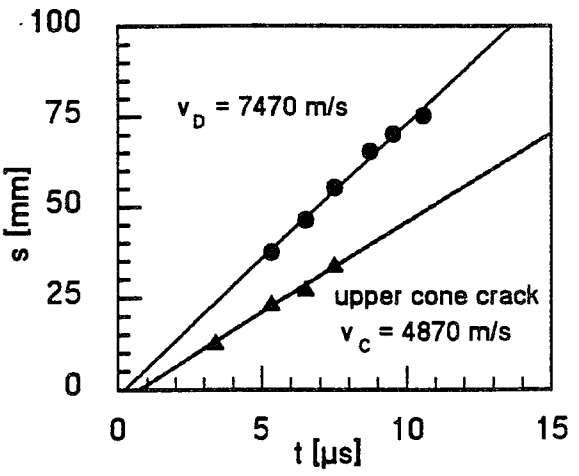


Figure 14.42 Shot no. 10326



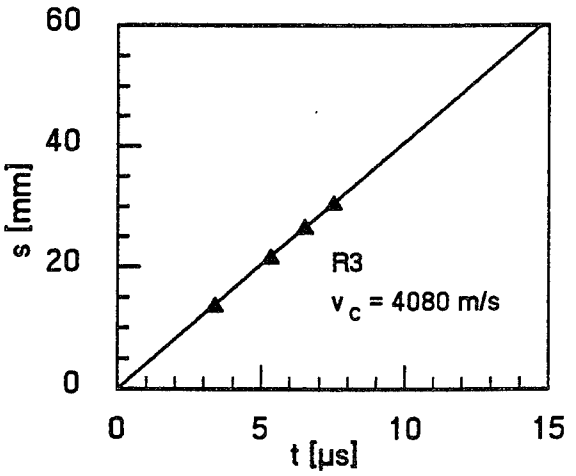


Figure 14.43 Path time plots of shot no. 10109

Shot No. 10136 (TiB_2, v_P = 150 m/s)

The fracture front and the lower cone crack (sharp edge) could be evaluated after the TiB_2 specimen was impacted at 150 m/s. The damage process is illustrated in Figure 14.44. The damage velocity was 8760 m/s, the lower cone crack grew at 4370 m/s (Fig. 14.45). The black spots that are visible within the crack field seem to correspond to small pits where material is broken out of the surface of the ceramic plate. This hypothesis is based on the examination of the surfaces of recovered fragments. Figure 14.46 shows a photograph of two fragments. Along the paths of several cracks pits have formed where material is broken out. Another remarkable feature of some fragments is that they are just 5 mm thick which means that the specimen was partially cleaved in the middle.

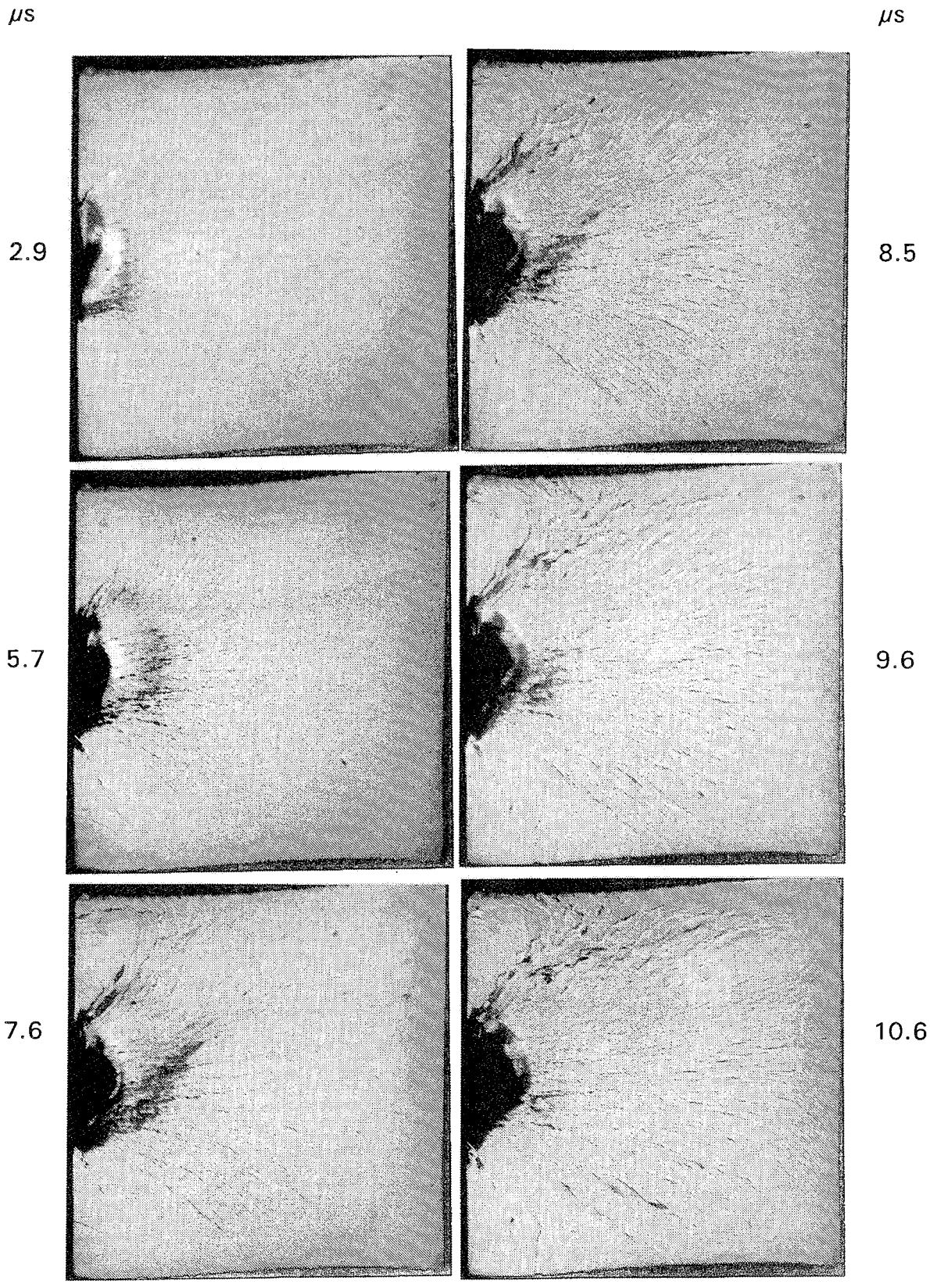


Figure 14.44 High-speed photographs of shot no. 10136

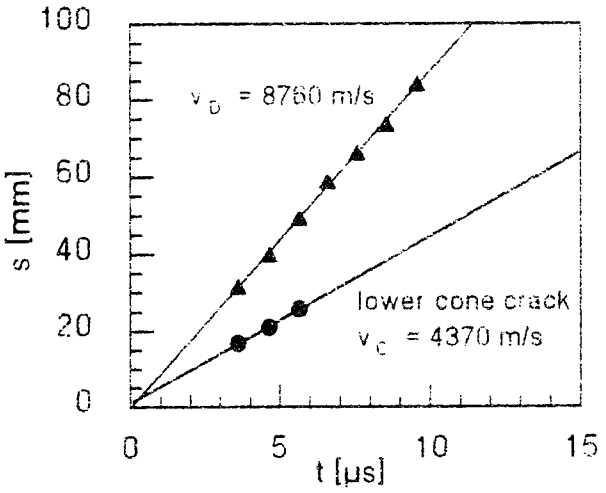


Figure 14.45 Path-time plot of shot no. 10136

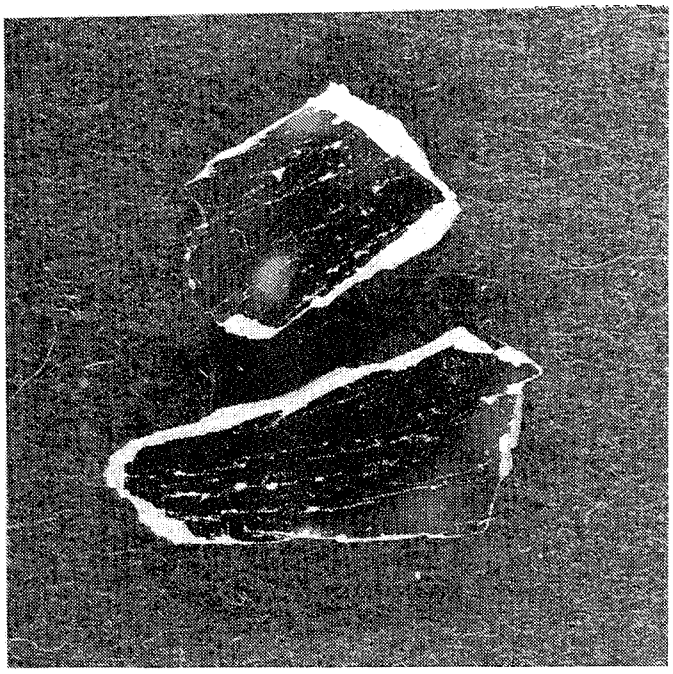


Figure 14.46 Photograph of two fragments of the specimen from shot no. 10136

Shot No. 10117 (TiB_2, v_P = 210 m/s)

The damage processes in a TiB_2 plate impacted at 210 m/s are illustrated in Figure 14.47. It was difficult to observe the cracks in this specimen because of the incomplete finishing of the surface. The evaluation of the damage front resulted in a damage velocity of 9250 m/s (Fig. 14.51).

Shot No. 10360 (TiB_2, v_P = 353 m/s)

After impact at 353 m/s a dense, homogeneous field of cracks radiates from the impacted edge of the TiB_2 specimen (Fig. 14.48). The number of cracks per unit area decreases the farther the field has propagated. The damage velocity was 8390 m/s (Fig. 14.52). The lower damage velocity compared to shot No. 10117 (v_P = 210 m/s) is probably due to a misalignment of the specimen. The axis of the projectile was shifted a few millimeters with respect to the middle plane of the ceramic plate so that the contact area was smaller compared to the other experiments.

Shot No. 10367 (TiB_2, v_P = 560 m/s)

The fracture patterns observed after impact at 560 m/s in TiB_2 (Fig. 14.49) is very similar to that of shot No. 10360 (v_P = 353 m/s). A fracture field radiates from the impacted edge and the number of cracks per unit area decreases with time of propagation. The damage velocity was 10420 m/s (Fig. 14.53). The bright stripes which superimpose the photographs are due to sparks generated by the impact. The head wave of the projectile can be recognized on the first three photographs.

Shot No. 10143 (TiB_2, v_P = 784 m/s)

A new damage phenomenon was found with TiB_2 at an impact velocity of 784 m/s. The photographs of the specimen (Fig. 14.50) show that the fracture front is preceded by a field of black spots on the surface.The damage velocity, which means in this case the propagation velocity of the front of the black spots, was 11195 m/s (Fig. 14.54). Only a few fragments of the specimen could be recovered, most of it was comminuted to very small particles. But an examination of the surfaces of the recovered fragments revealed many small pits where material was broken out (Fig. 14.55). The difference to the black spots observed with shot no. 10136 (v_P = 150 m/s) is that here the spots occur ahead of the fracture front. The macroscopic inspection of the fragments reveals further more that this specimen was cleaved in the middle between the polished surface and the rear surface, too. Figure 14.56 shows a photograph of recovered fragments.

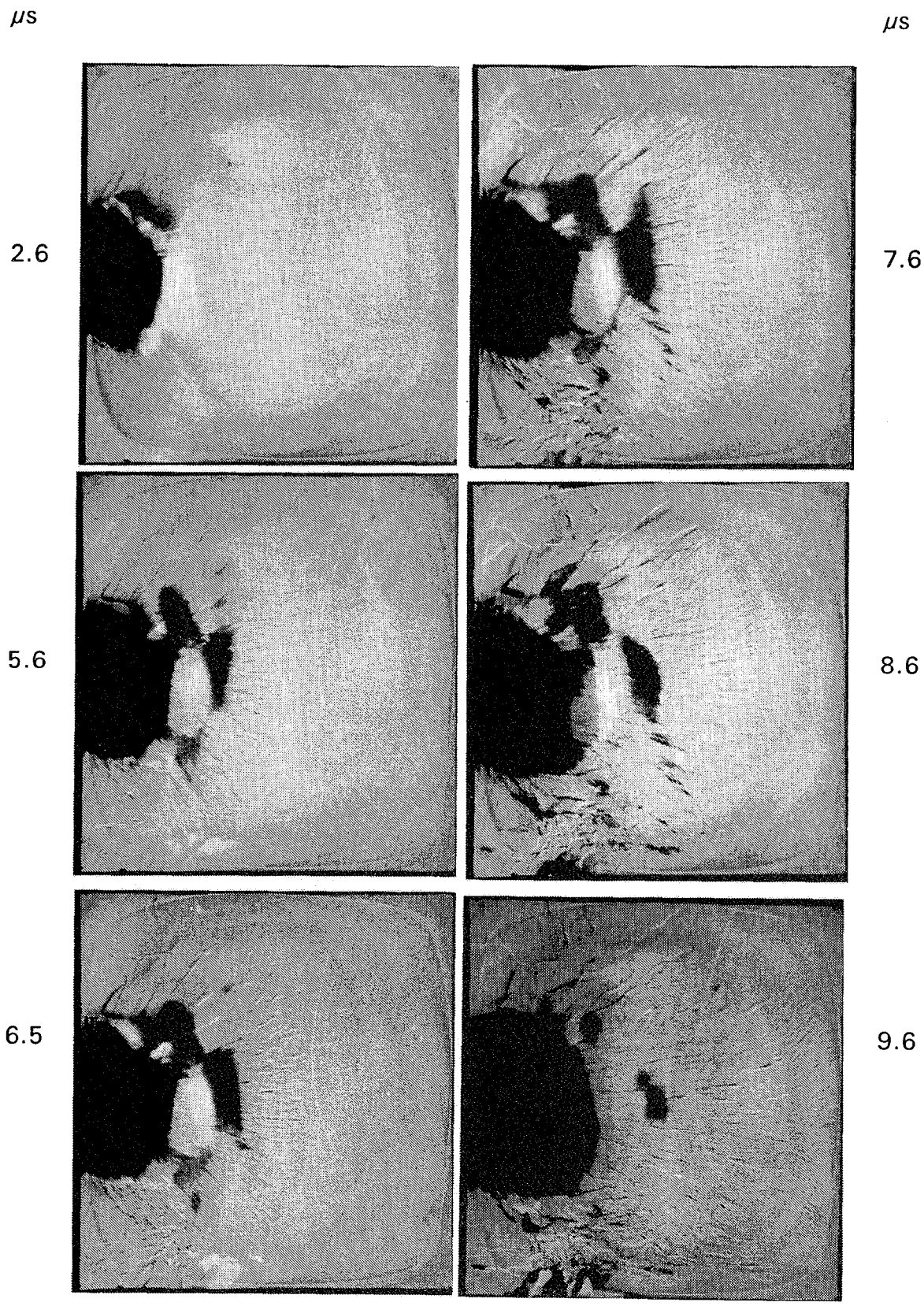


Figure 14.47 High-speed photographs of shot no. 10117

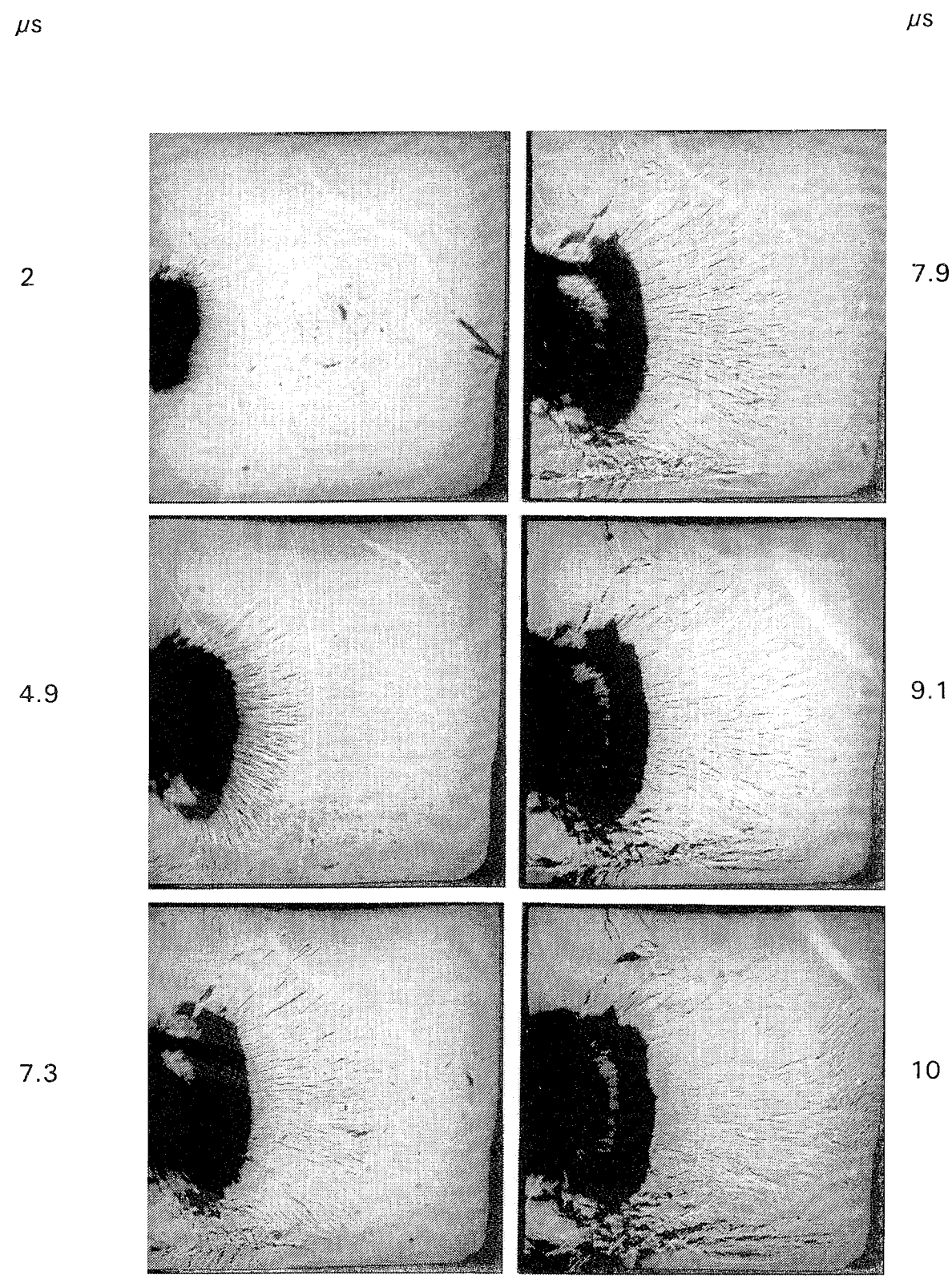


Figure 14.48 High-speed photographs of shot no. 10360

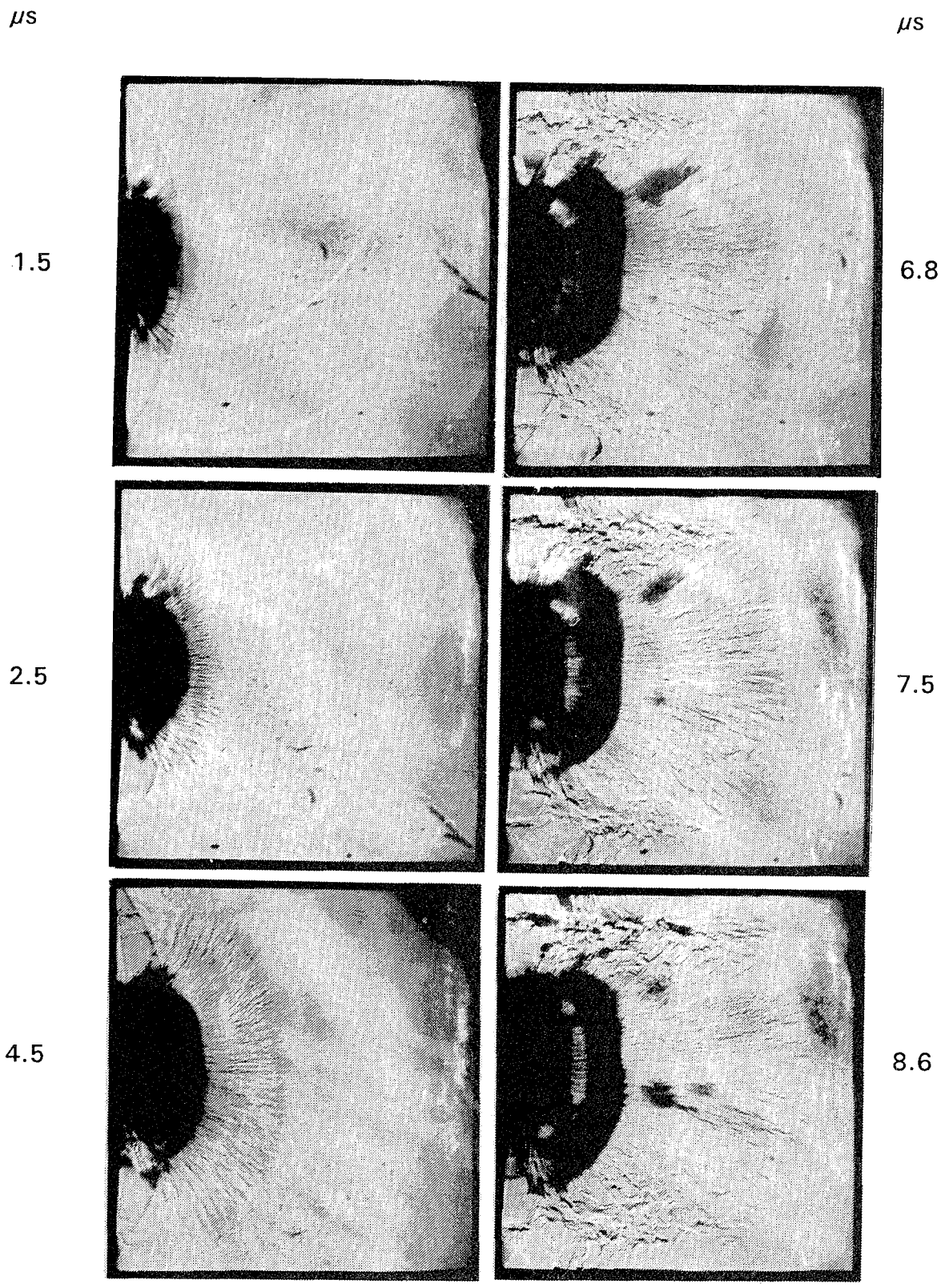


Figure 14.49 High-speed photographs of shot no. 10367

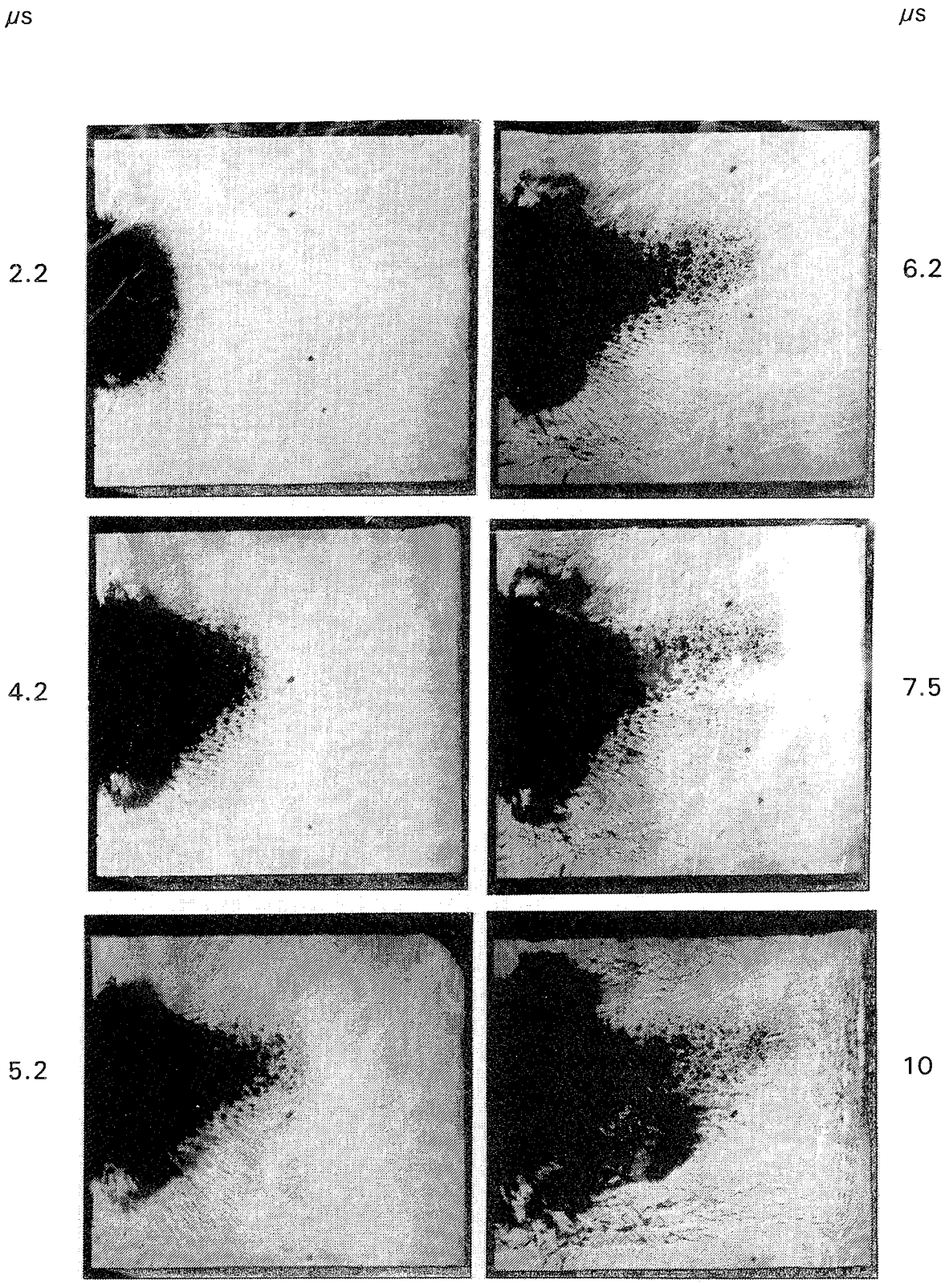


Figure 14.50 High-speed photographs of shot no. 10143

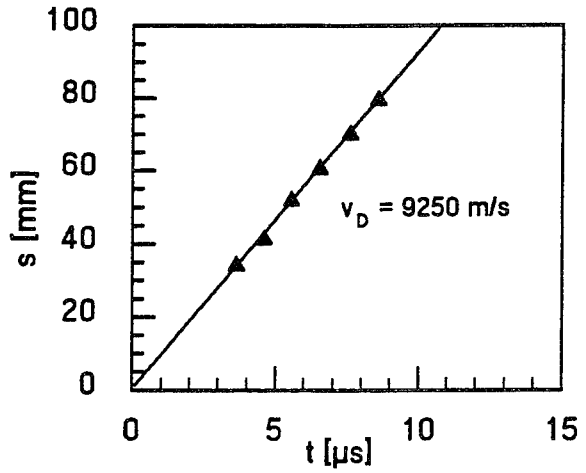


Figure 14.51 Path-time plot of shot no. 10117

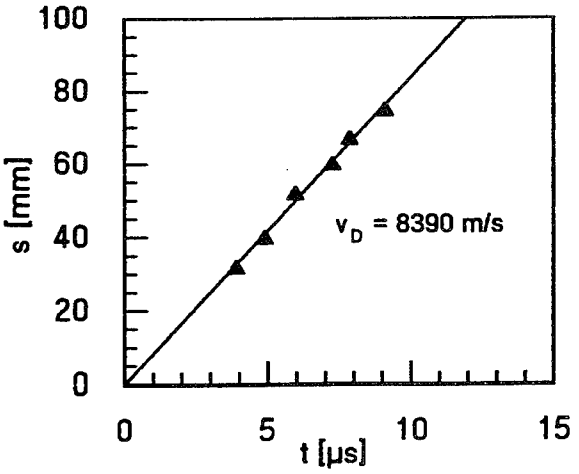


Figure 14.52 Path-time plot of shot no. 10360

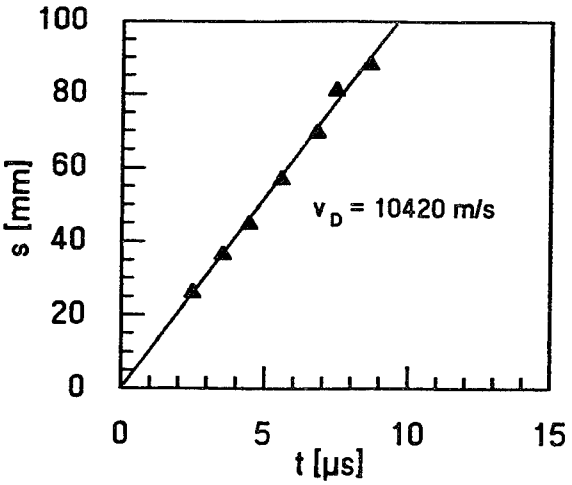


Figure 14.53 Path-time plot of shot no. 10367

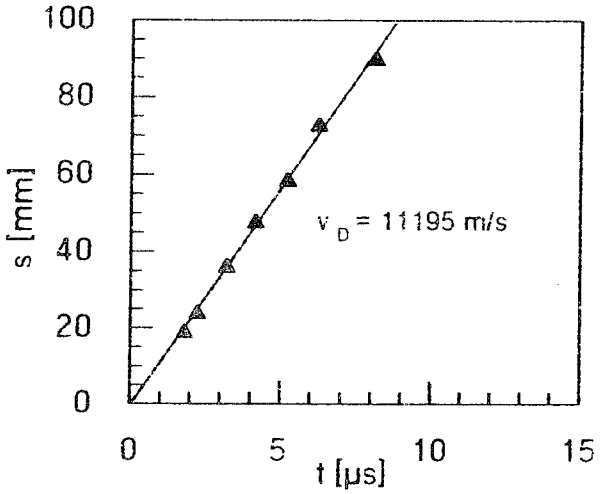


Figure 14.54 Path-time plot of shot no. 10143

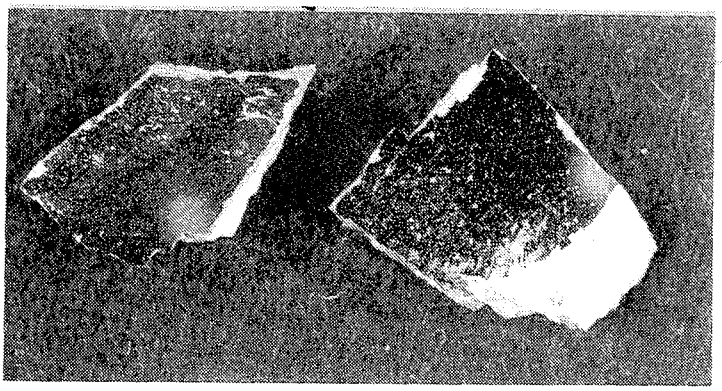


Figure 14.55 Photograph of two fragments of shot no. 10143

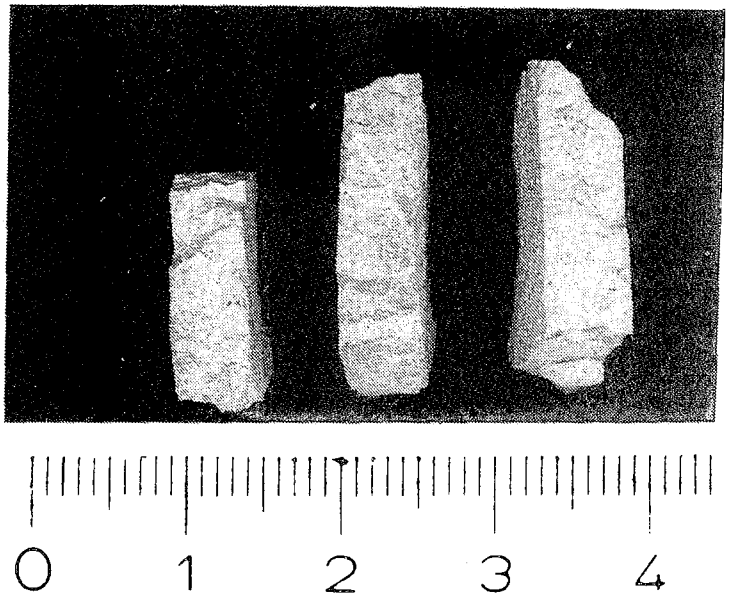


Figure 14.56 Fragments of 5 mm thickness from shot no. 10143 (scale in cm)

Shot No. 10366 (TiB_2, v_P = 1000 m/s)

The TiB_2 plate impacted at 1000 m/s (Fig. 14.57) exhibits the same damage phenomena observed in the experiment at 780 m/s. Black spots precede the fracture field. The damage velocity was 11510 m/s (Fig. 14.59).

14.3 Experiments with Alumina (Al_2O_3)

Shot No. 10131 (Al_2O_3 CeramTech AD 1898, v_P = 31 m/s)

Only one cone crack could be recognized and evaluated during the time interval of observation. The mean fracture velocity was 3090 m/s.

Shot No. 10132 (Al_2O_3 CeramTech AD 1898, v_P = 85 m/s)

Figure 14.58 shows an Al_2O_3 ceramic plate after impact at 85 m/s. The surface of the specimen was coated with a layer of silver. The crack pattern is similar to that observed with SiC at the same impact velocity. Several radial cracks are generated between the cone cracks. Most of the radial cracks have sharp edges in the beginning and turn into frequently branching fractures with fuzzy edges at a distance of about 35 mm from the impacted edge. The specimen could be reassembled only partially, so that the crack surfaces on the fragments could not be associated with specific cracks seen on the high-speed photographs. But several crack surfaces of fragments which obviously originate from the impact zone reveal a transition from smooth to rough as it was observed with SiC (shot no. 10111, Fig. 14.5). The front of the fracture field propagated at a mean velocity of 5320 m/s (Fig.14.60). The mean velocity of the wave which can be observed on three photographs was 5660 m/s. The upper cone crack grew at 3860 m/s, the crack R1 at 4490 m/s during it exhibits a fuzzy edge. The crack R2 exhibits a sharp edge over the full length. This crack grew at 2390 m/s first, slowed down and arrested.

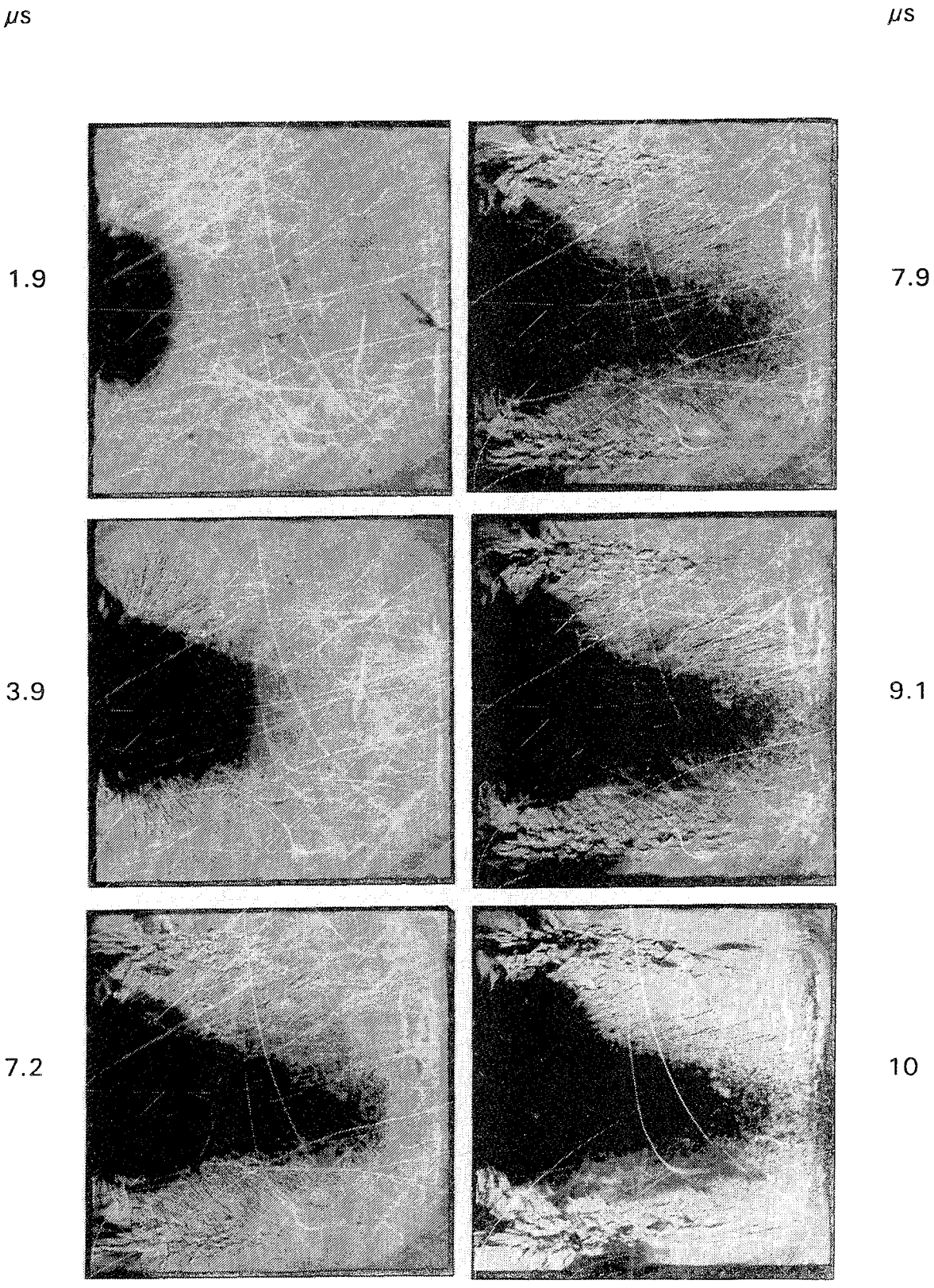


Figure 14.57 High-speed photograph of shot no. 10366

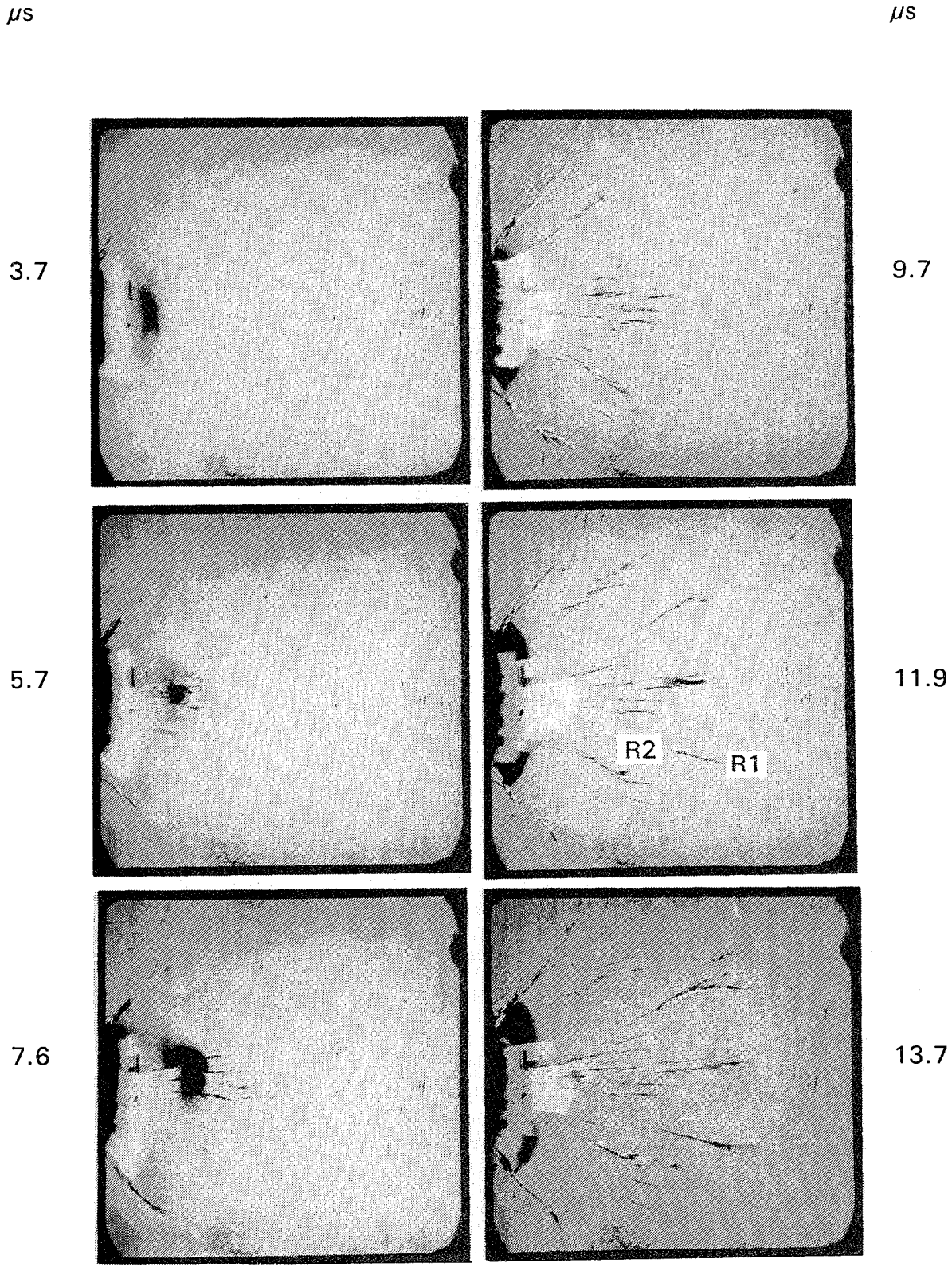


Figure 14.58 High-speed photograph of shot no. 10132

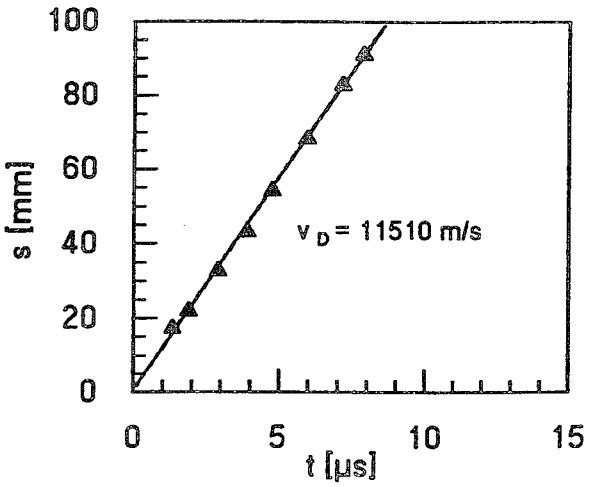


Figure 14.59 Path-time plot of shot no. 10366

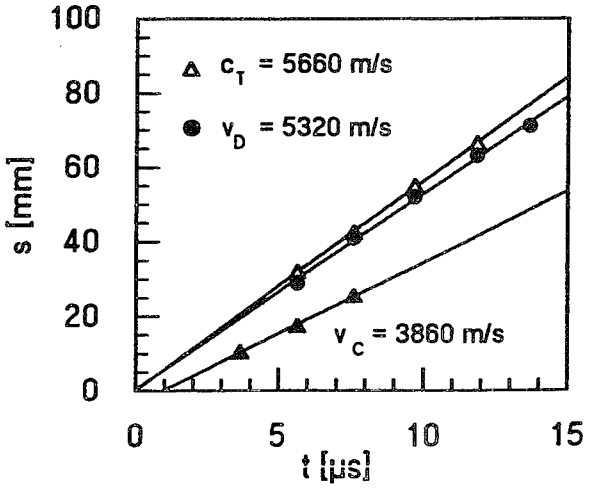


Figure 14.60 Path-time plot of shot no. 10132

Shot No. 10134 (Al_2O_3 CeramTech AD 1898, v_P = 150 m/s)

The fracture and damage propagation in an Al_2O_3 CeramTech specimen after impact at 150 m/s is shown in Figure 14.61. A field of cracks in the lower half of the plate and two main single fractures (R1, R2) in the upper half can be recognized. The propagation velocities were 4840 m/s and 4900 m/s with R1 and R2, respectively, the front of the fracture field propagated at 5635 m/s (Fig. 14.63).

Shot No. 10135 (Al_2O_3 CeramTech AD 1898, v_P = 220 m/s)

The high-speed photographs in Figure 14.62 illustrate the destruction of an Al_2O_3 specimen after being impacted at 220 m/s. The black spots and stripes on the right side are caused by damage of the silver layer on the surface of the ceramics. The concentric rings are due to the polishing process. Fracture propagation itself can hardly be observed in this experiment. Two black zones develop, one approximately in the center of the plate and one below, which seem to be confined by cracks so that crack propagation is indirectly visible. The black zone in the center (or the confining cracks) proceeds at a mean velocity of 9630 m/s (Fig. 14.64).

The shots number 5570 (v_P = 707 m/s) and no. 5542 (v_P = 1062 m/s) are described in detail in [14].

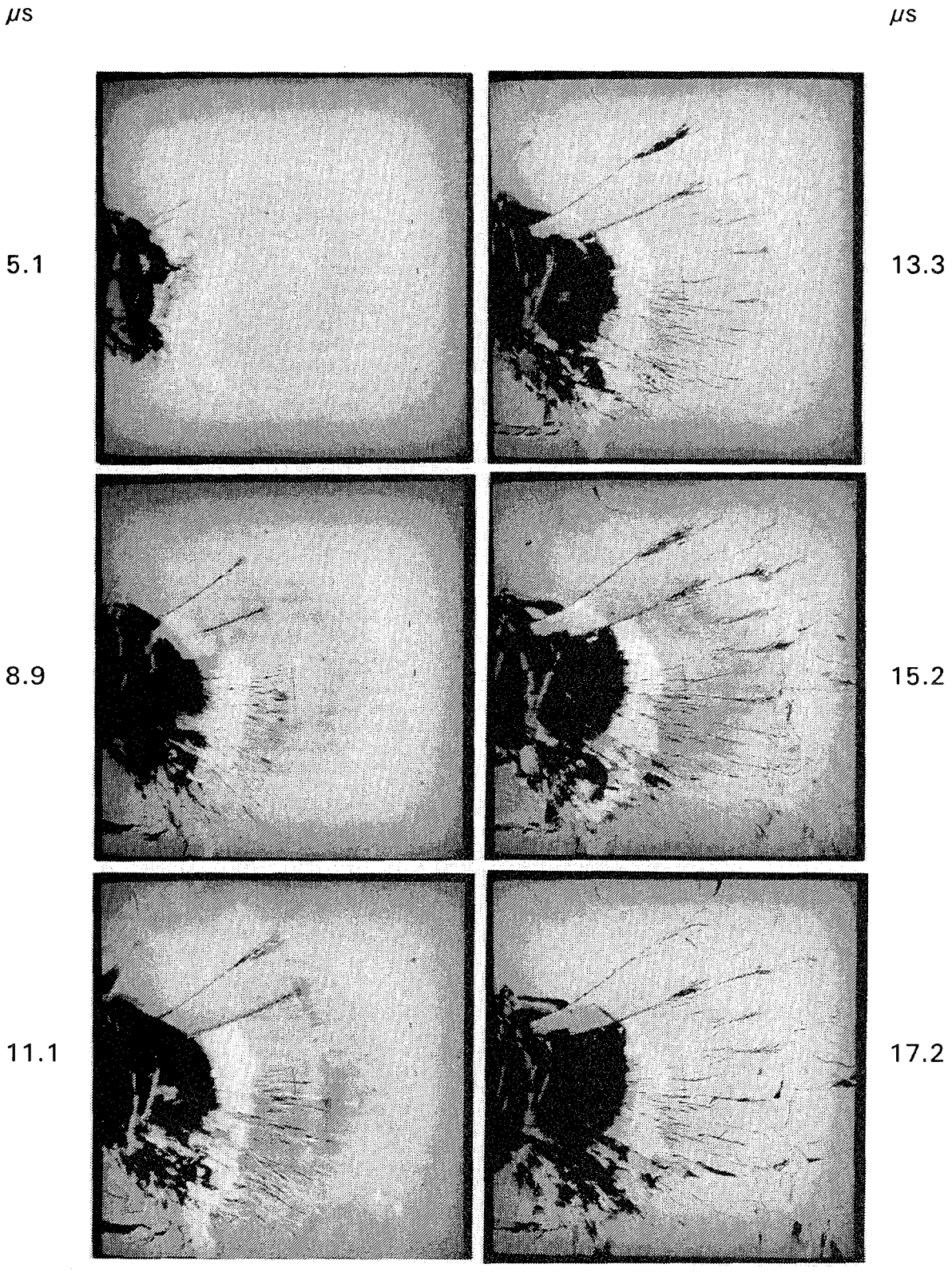


Figure 14.61 High-speed photographs of shot no. 10134

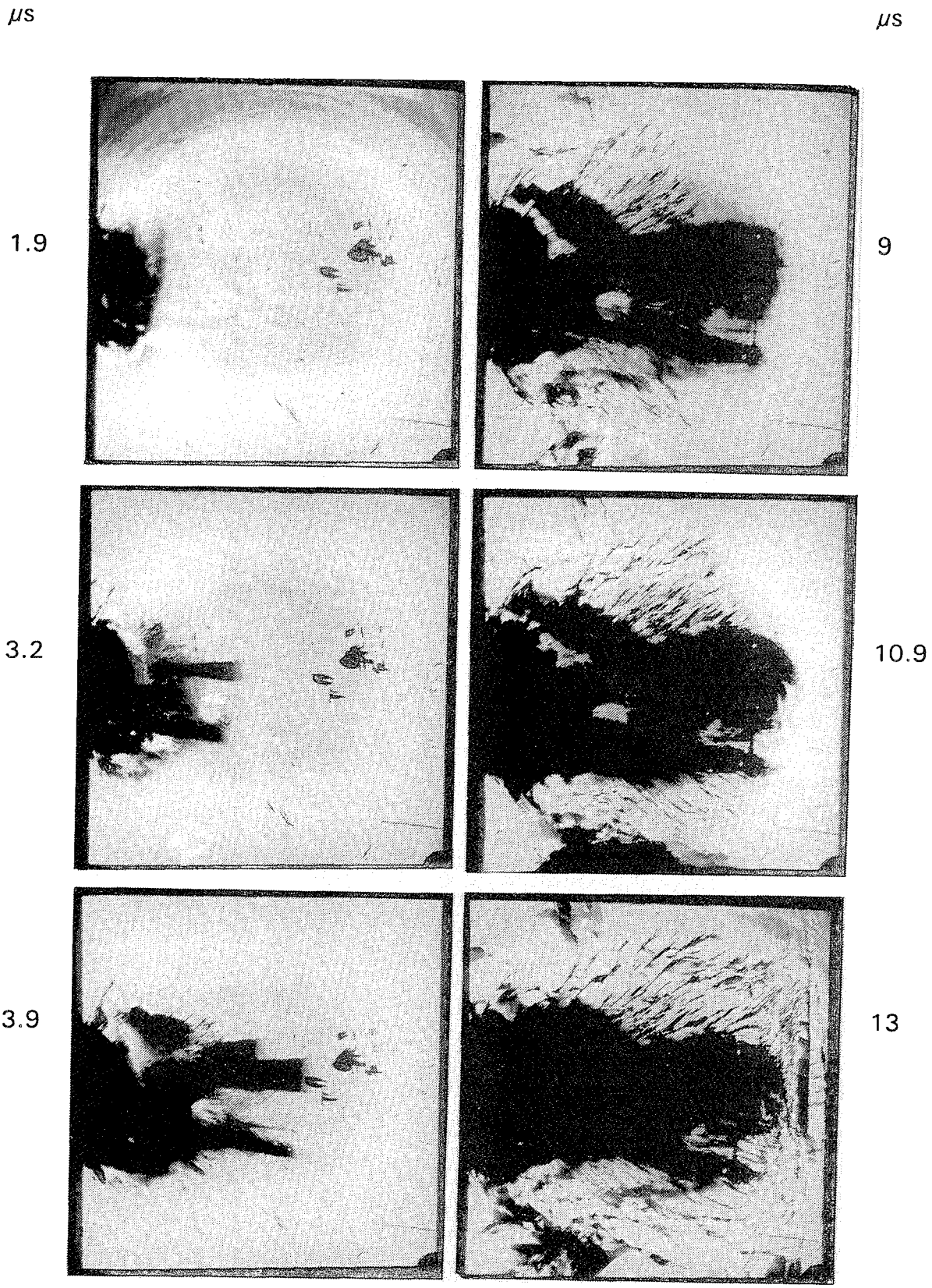


Figure 14.62 High-speed photograph of shot no. 10135

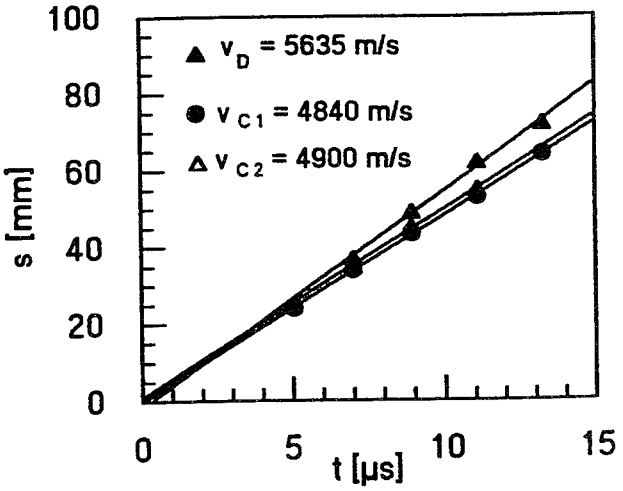


Figure 14.63 Path-time plot of shot no. 10134

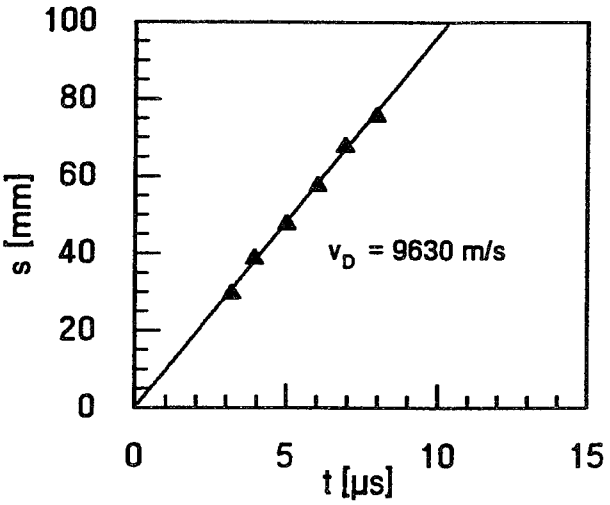


Figure 14.64 Path-time plot of shot no. 10135

15. Classification of Damage

Figure 15.1a and 15.1b show schematically the types of fractures that were observed. The designations for the different types of fracture were chosen analogous to the designations of the fracture types in glass [12]. In most cases the cone cracks could be identified first on the high-speed photographs. They start from the impact site of the edge of the projectile. The cracks that are generated in the region between the cone cracks are called primary cracks. In opposition to the fracture propagation observed in glasses, the primary fractures in ceramics do not appear as fine dark lines which grow continuously from the impact site. In most cases the edges and tips of the primary cracks are fuzzy. Branching of the cracks occurs frequently. Some of the cracks look like branches of a fir-tree (type 1, Fig. 15.1a), others seem to consist of many, successively formed short cracks which include a small angle with the main direction of fracture propagation (type 2, Fig. 15.1a). Two photographs of SiC specimens which exhibit the different types of cracks are shown in Figure 15.2. Primary cracks with sharp edges are observed rarely. But it has also been observed that a crack with sharp edges suddenly turns into a crack of type 1 or 2. At striking velocities $\leq$ 85 m/s the specimens could be rebuilt from the recovered fragments. An inspection of the crack surfaces revealed, that the crack surfaces are smooth when the edges are sharp. Cracks that appear fuzzy on the polished surface of the specimen have rough crack surfaces.

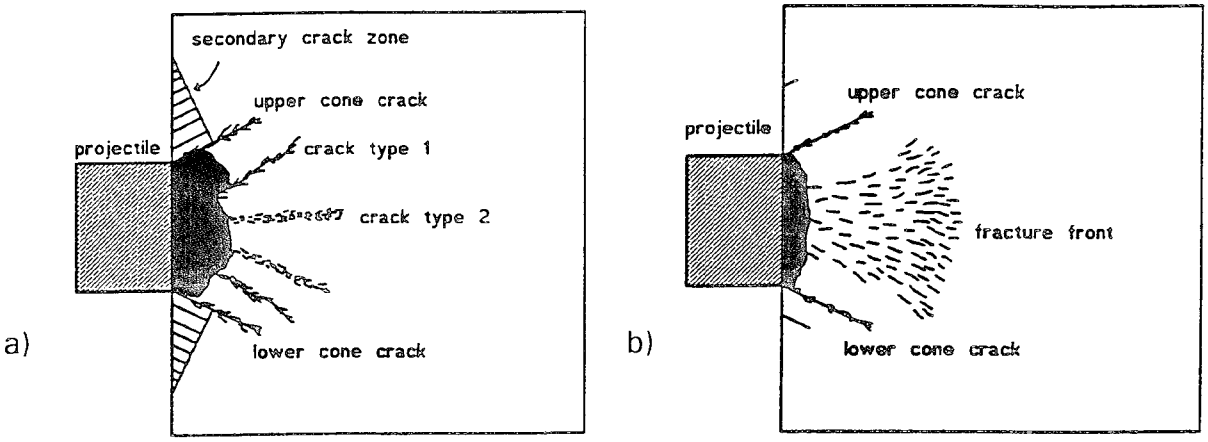


Figure 15.1 Schematic representation of the observed types with SiC and Al_2O_3 (a) and TiB_2 (b)

Similar to the fracture patterns found with glasses, wedge-shaped fracture zones can be recognized above the upper and below the lower cone crack. These secondary cracks always reveal sharp edges. This type of crack occurred most clearly with SiC at a striking velocity of 185 m/s, which can be seen from the photograph (4.6 μs after impact) shown in Figure 15.2b.

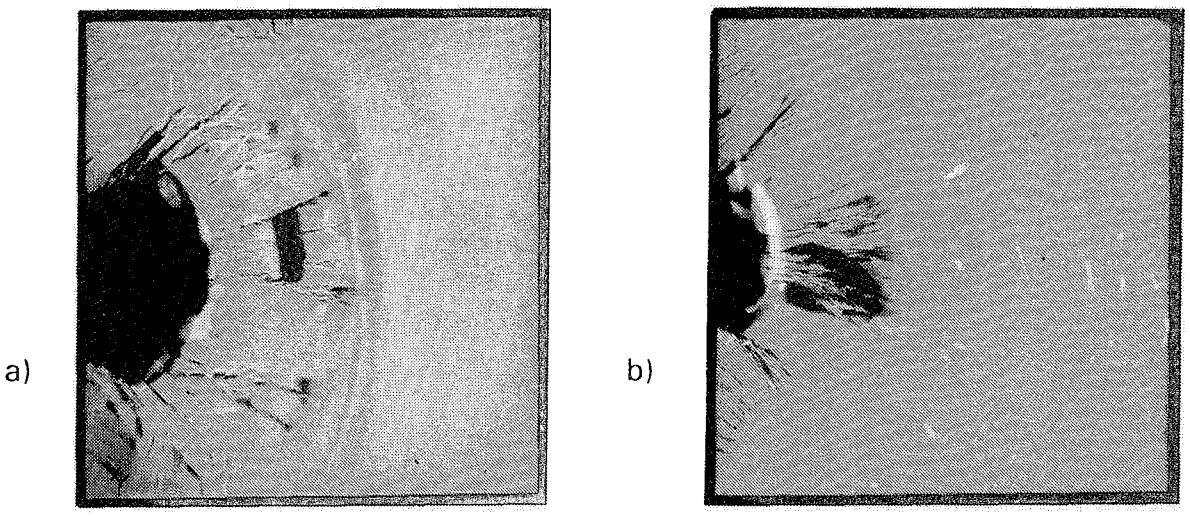


Figure 15.2 SiC at a) v_P = 150 m/s, t = 10.5 μs, b) v_P = 185 m/s, t = 4.6μs

With the TiB_2 specimen cracks of the types 1 and 2 can hardly be observed. Already at low loadings a fracture front forms between the cone cracks that consists of many short cracks. This fracture pattern is drawn schematically in Figure 15.1b. The photograph of a TiB_2 plate 5.3 μs after impact at 85 m/s illustrates this type of damage (Fig. 15.3).

The fracture patterns observed with the Al_2O_3 ceramics are similar to those in the SiC. Figure 15.4 shows an Al_2O_3 specimen 9.7 μs after impact at 85 m/s. At impact velocities in the range 350 m/s $\leq v_P \leq$ 600 m/s the fracture patterns of SiC and TiB_2 are similar. This is demonstrated by the photographs of a SiC specimen (v_P = 513 m/s, 4.6 μs after impact) and a TiB_2 specimen (v_P = 560 m/s, 4.5 μs after impact) in Figure 15.5. In both cases a dense field of fuzzy cracks grows into the specimen. The density of the crack field decreases with increasing time of propagation. The fracture patterns observed with SiC and Al_2O_3 at impact velocities between 600 m/s and 1000 m/s do not differ from those in the range 350 m/s $\leq v_P \leq$ 600 m/s.

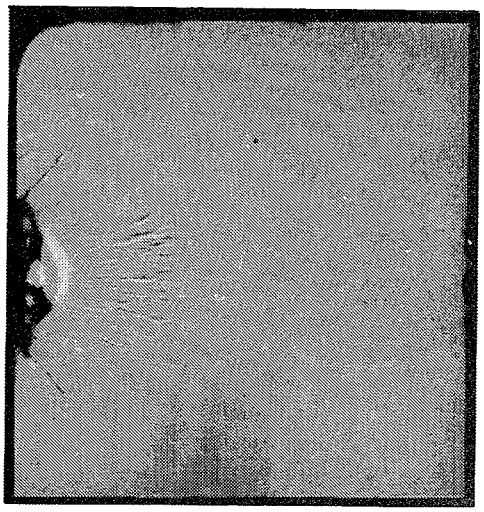
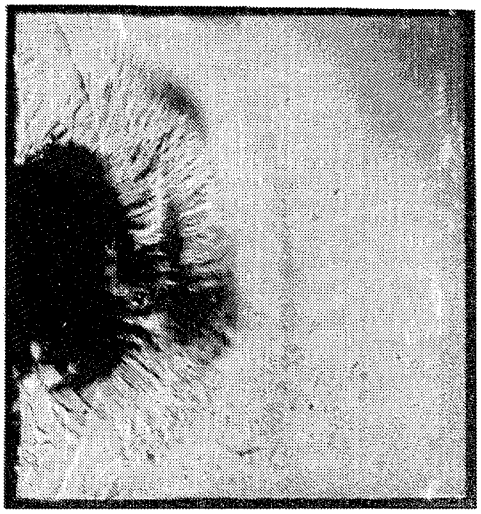


Figure 15.3 TiB_2, v_P = 85 m/s, t = 5.3 μs



Figure 15.4 Al_2O_3, v_P = 85 m/s, t = 9.7 μs

a)



b)

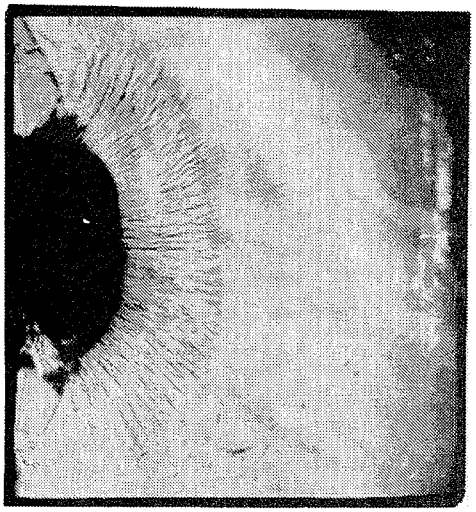


Figure 15.5 SiC, v_P = 513 m/s, t = 4.6 μs (a) and TiB_2, v_P = 564 m/s, t = 4.5 μs (b)

A new damage phenomenon was found with TiB_2 at impact velocities above 780 m/s. Figure 15.6 shows a photograph of a TiB_2 specimen, 6.2 μs after the impact of the projectile at 784 m/s. The fracture front is preceded by a field of black dots on the surface of the specimen. Only few fragments of the specimen could be recovered, most of it was comminuted to very small particles. But an examination of the surfaces of the recovered fragments revealed many small pits where material was broken out. This is the only hint with respect to the origin of the black dots seen on the high-speed photographs.

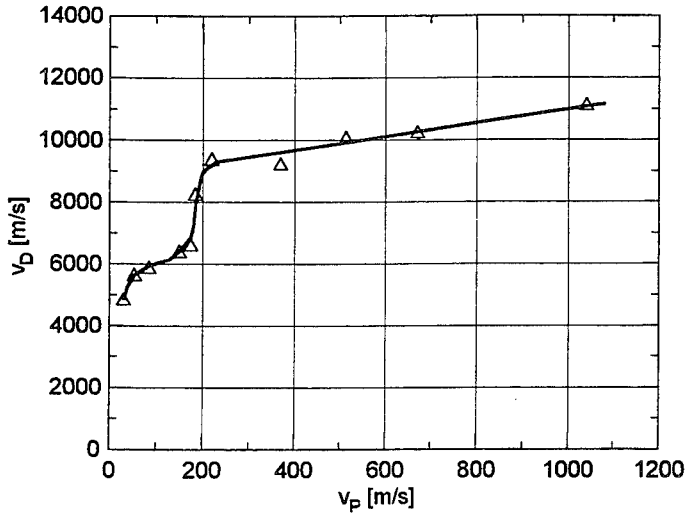


Figure 15.6 TiB_2, v_P = 784 m/s, t = 6.2 μs, shot no. 10143

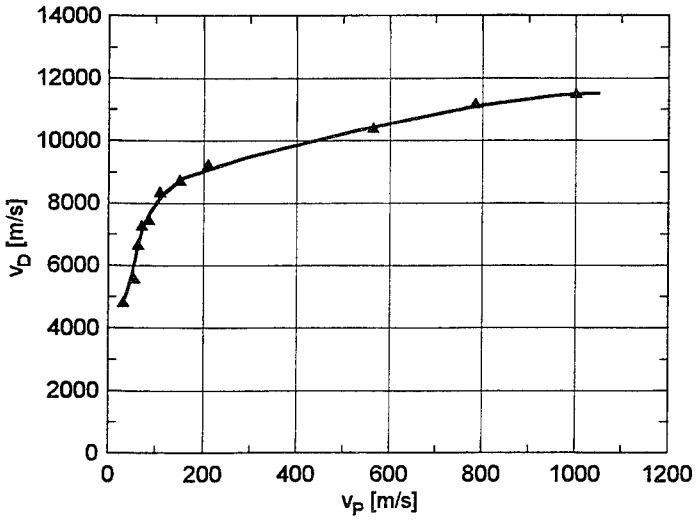
16. Analysis of Fracture Velocities

Other than in glass, different types of cracks are generated and different fracture velocities are observed at one impact velocity in one specimen. Therefore, it is necessary to distinguish between the velocity of continuously growing cracks, including the secondary cracks with sharp edges, fuzzy crack traces and crack fronts. In the following the term damage velocity in ceramics always denotes the velocity of the fastest fracture which was observed. In Figures 16.1a, b, c the mean damage velocities v_D observed with SiC, TiB_2 and Al_2O_3 are plotted versus the impact velocity v_P. In each of the ceramics v_D increases with increasing striking velocity. The damage velocities approach the longitudinal wave velocity c_L at high loadings. With TiB_2, v_D rises continuously and c_L is gained when v_P exceeds 780 m/s. SiC and Al_2O_3 exhibit a steep rise of v_D in the range of striking velocities between 150 m/s and 200 m/s. In the case of SiC this step corresponds to the transition in fracture type from single, distinguishable fuzzy crack traces to a crack front.

a) SiC



b) TiB_2



c) Al_2O_3

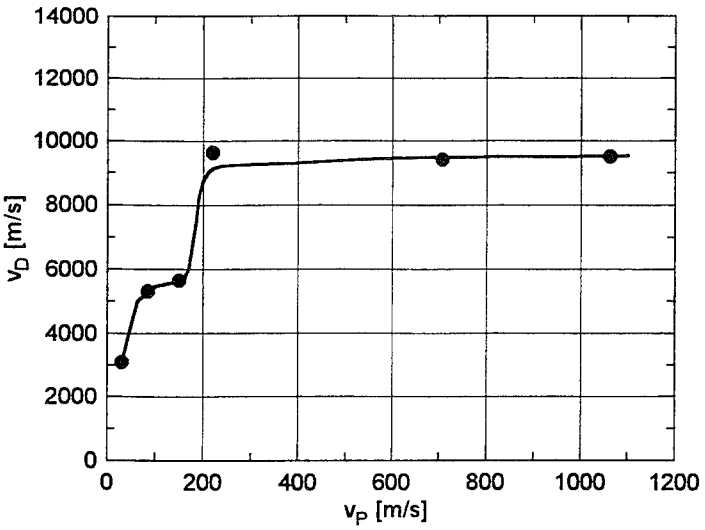


Figure 16.1 Damage velocity versus impact velocity for (a) SiC, (b) TiB_2, and (c) Al_2O_3 (CeramTech A 1898)

Some of the SiC specimen exhibited secondary fracture zones very clearly. The fact that the secondary cracks form a triangle shows that they grow at the same speed. The analysis of velocities of all those secondary cracks whose tips could be observed on several photographs revealed crack velocities between 3000 m/s and 4000 m/s independent of the loading. The mean velocity of the secondary cracks is 3490 m/s ± 390 m/s. In four of our experiments the transversal wave generated at the impact could be observed. The mean of the measured velocities is 7255 m/s ± 140 m/s. The Rayleigh wave velocity c_R is approximately 0.9 c_T from what follows $c_{T,SiC}$ = 6530 m/s. The investigations of glasses [6,12,13] have shown that the secondary cracks propagate at terminal crack velocity v_C, which is approximately half of the Rayleigh wave velocity with float glass and the optical glasses K5 and F6. This is also correct with the secondary cracks in SiC: $v_{C,SiC} \approx 0.5\ c_R$ = 3265 m/s. This analogy suggests that a terminal crack velocity exists for SiC. However, this velocity has been observed only with one of the various types of fracture. Therefore, it is important to distinguish between the different types of fracture whenever fracture velocities are considered.

17. Microstructural Analysis

Recovered fragments were sectioned in a direction perpendicular to the surfaces of the undamaged specimen. Micrographs of TiB_2 specimen (impacted at 784 m/s) and a SiC specimen (impacted at 1040 m/s) are shown in Figure 17.1. The most remarkable feature of the TiB_2 fragment is that a lot of voids have been generated particularly at these points where three or more grains adjoin and in the interior of the large grains. Transcrystalline and intercrystalline fracture is observed. The micrograph shows that the cracks within the large grains as well as the intercrystalline cracks have been formed by coalescence of voids. The formation of voids has not been found with SiC as the micrograph reveals. Cracks are mainly intercrystalline in this fine grained material.

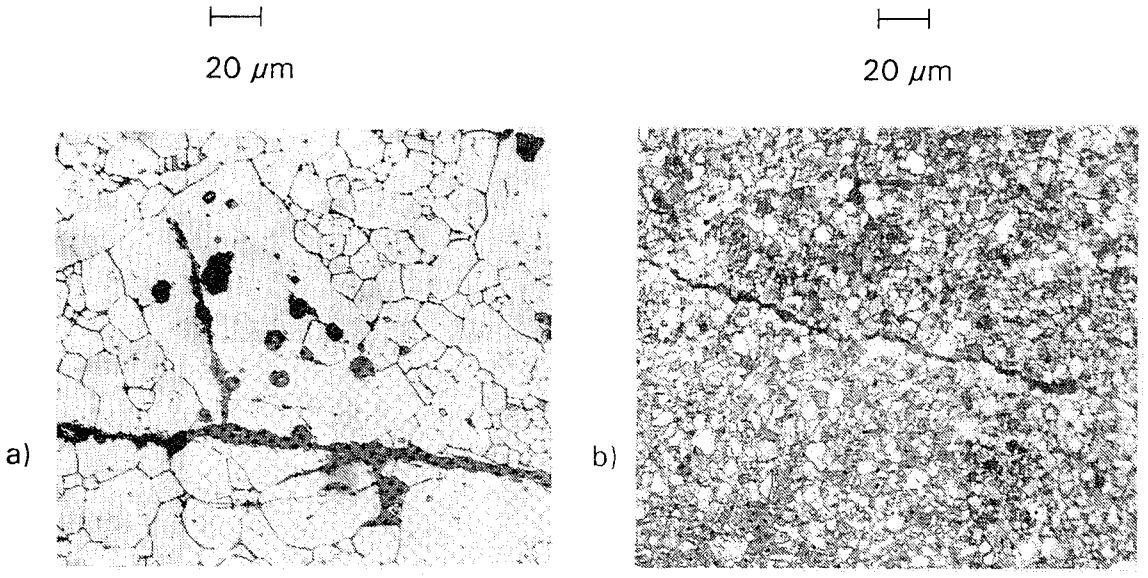


Figure 17.1 Micrographs of impacted ceramics. a) TiB_2, v_P = 784 m/s, b) SiC, v_P = 1040 m/s

18. Dual Side High-Speed Photography

A new experimental configuration was set up to take high-speed photographs of both sides of the impacted specimen simultaneously. Figure 18.1 shows a top view of this set up. The specimen is placed directly in front of the muzzle of the gas gun. One 24-spark unit is positioned above the barrel of the gas gun.

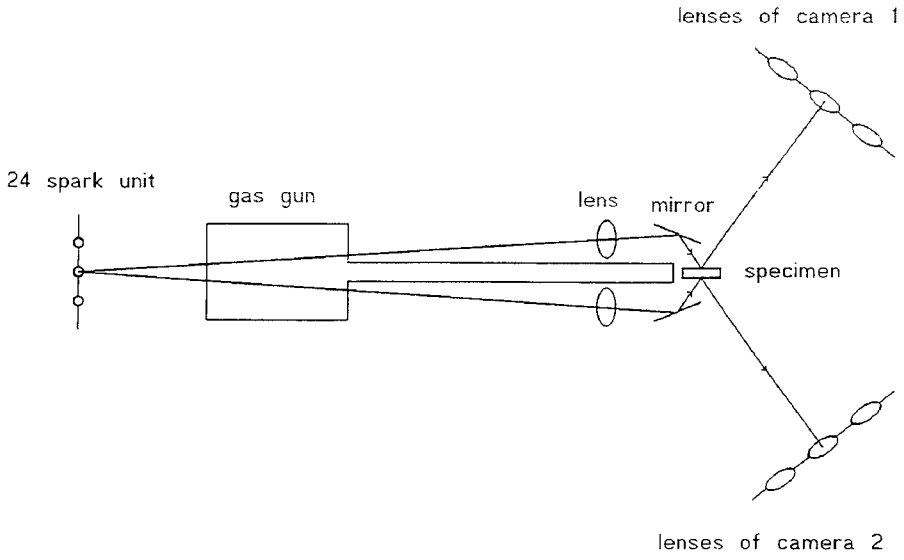


Figure 18.1 Experimental configuration for dual-side high-speed photography

A lens and a mirror on each side of the specimen focus and deflect the light from the sparks to the surfaces of the specimen. Two cameras, one on each side of the specimen, are installed to observe the damage processes.

Three experiments were conducted with SiC specimens which were polished on both sides. Two of the specimens were thin plates of the standard dimensions 100 mm x 100 mm x 10 mm. The impact velocities were 66 m/s and 202 m/s.

The result of the test at 66 m/s is illustrated in Figure 18.2 by three photographs of each side of the specimen. The photographs reveal nearly the same fracture pattern on both sides. Some of the cracks can be seen clearly on one side of the specimen but hardly on the other side. This is due to different crack openings on the different sides. R1 is the crack that could be measured best on both sides. The crack velocity measured on the left side was $v_{c,l}$ = 5210 m/s ± 270 m/s. The measurement on the right side resulted in $v_{c,r}$ = 5030 m/s ± 92 m/s. The differences between the positions of the crack tip on both sides do not exceed 3.5 mm.

Figure 18.3 shows three couples of photographs of the specimen impacted at 202 m/s. The similarity of the fracture patterns is obvious in this case, too. However, a reliable measurement of fracture and damage velocities was not possible in this experiment because the crack tips and the fracture front were superimposed by the black area on most of the photographs.

One experiment was conducted with a thick SiC plate of the dimensions 203 mm x 203 mm x 35 mm at an impact velocity v_P = 202 m/s. Figure 18.4a and 18.4b show the fracture patterns observed on the two polished sides of the specimen. In this arrangement the specimen could not be illuminated completely. When only one side of the specimen is observed, the angle of incidence of the light (with respect to the normal to the surface) is chosen as small as possible. In the arrangement for dual side photography a big angle of incidence not only with respect to the normal to the surface of the specimen but also with respect to the normal to the mirror can not be avoided. This decreases the effective area of the mirrors and the lenses.

Figures 18.4a and 18.4b show the complete series of high-speed photographs of both sides of the specimen. Different fracture patterns are observed on the two sides. It can be recognized that the fracture front is further advanced on the left side of the specimen. From photograph 15 to photograph 20, where the fractures can be seen most clearly, the maximum difference between the x-positions of the fracture fronts is about 22 mm. The fracture velocities observed on the left side range from 4100 m/s to 5440 m/s. On the right side of the specimen fracture velocities between 4730 m/s and 6780 m/s were measured.

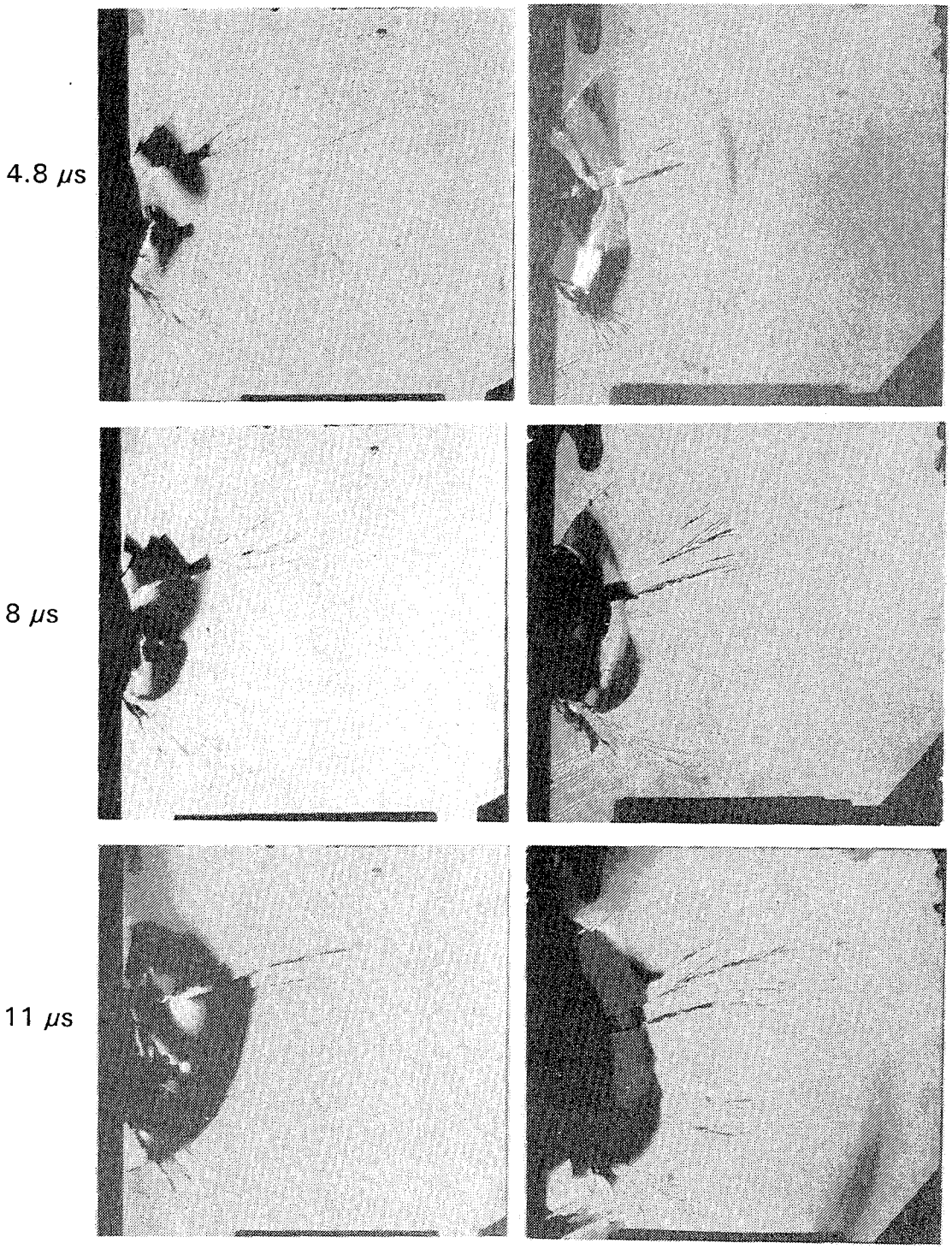
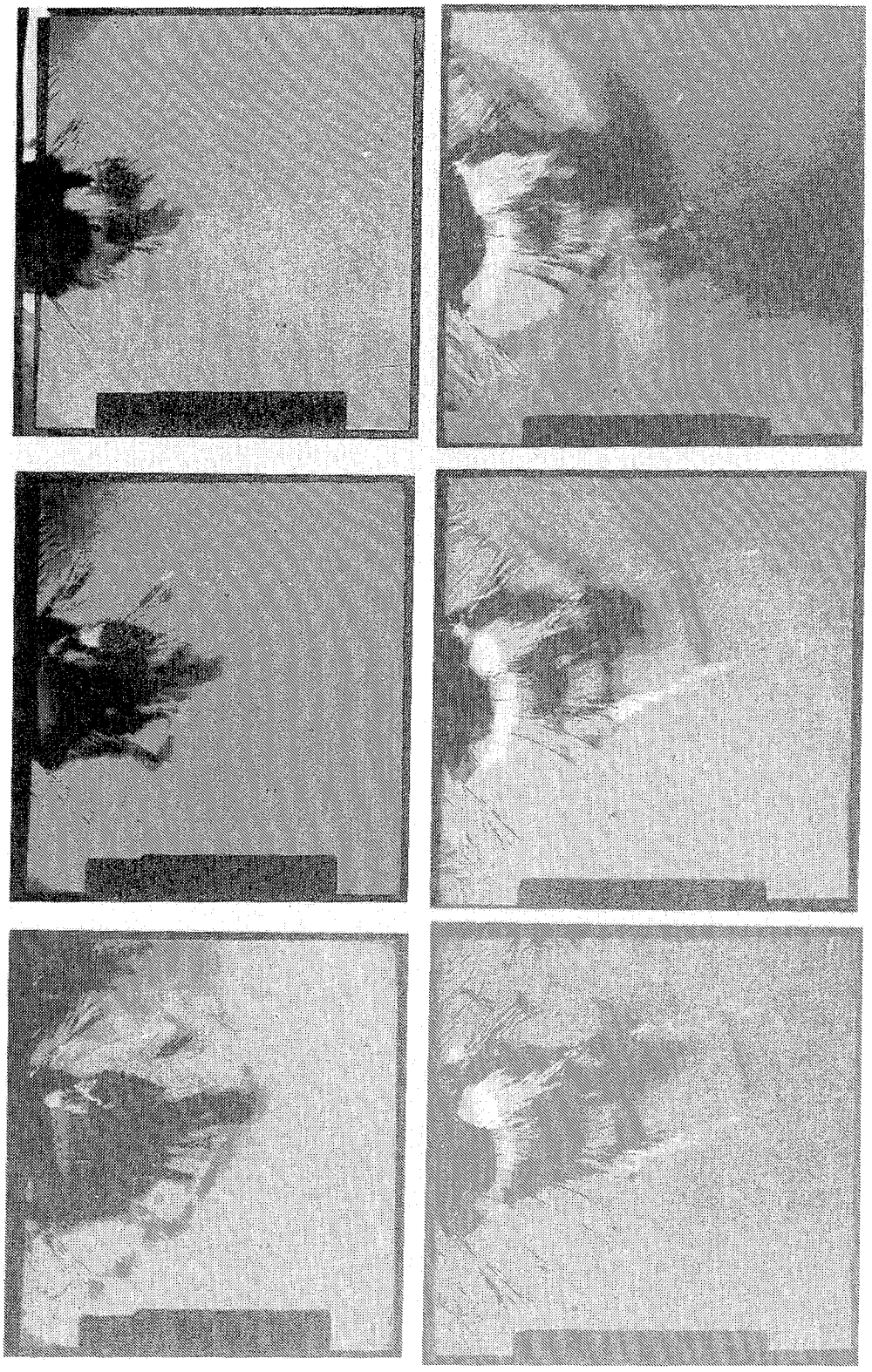


Figure 18.2 Comparison of three high-speed photographs from both sides of a SiC specimen, shot no. 10517, v_P = 66 m/s



left side right side

Figure 18.3 Comparison of three high-speed photographs from both sides of a SiC specimen, shot no. 10551, v_P = 202 m/s, Δt = 1 μs

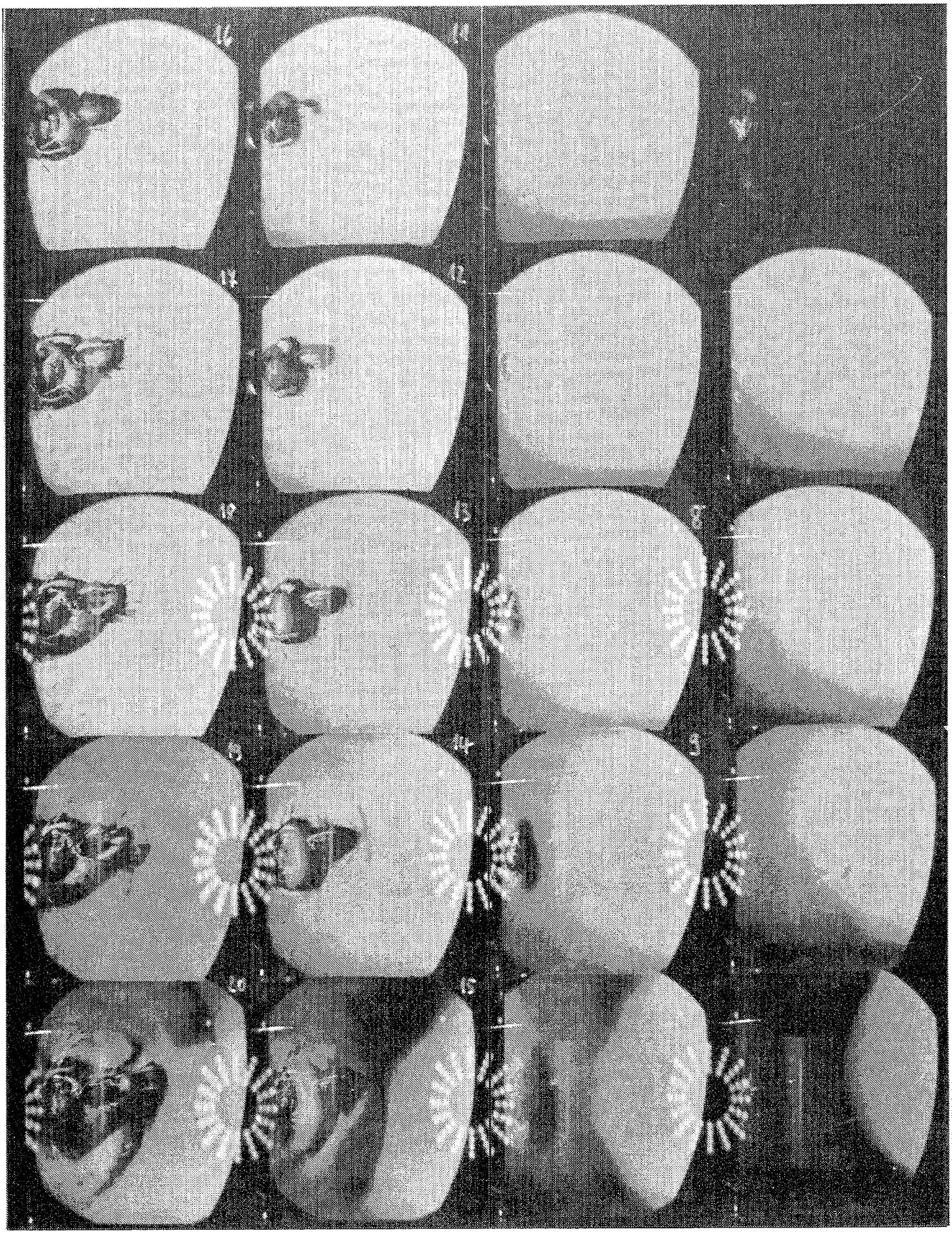


Figure 18.4a Complete series of high-speed photographs of shot no. 10600, left side, $\Delta t = 1\ \mu s$

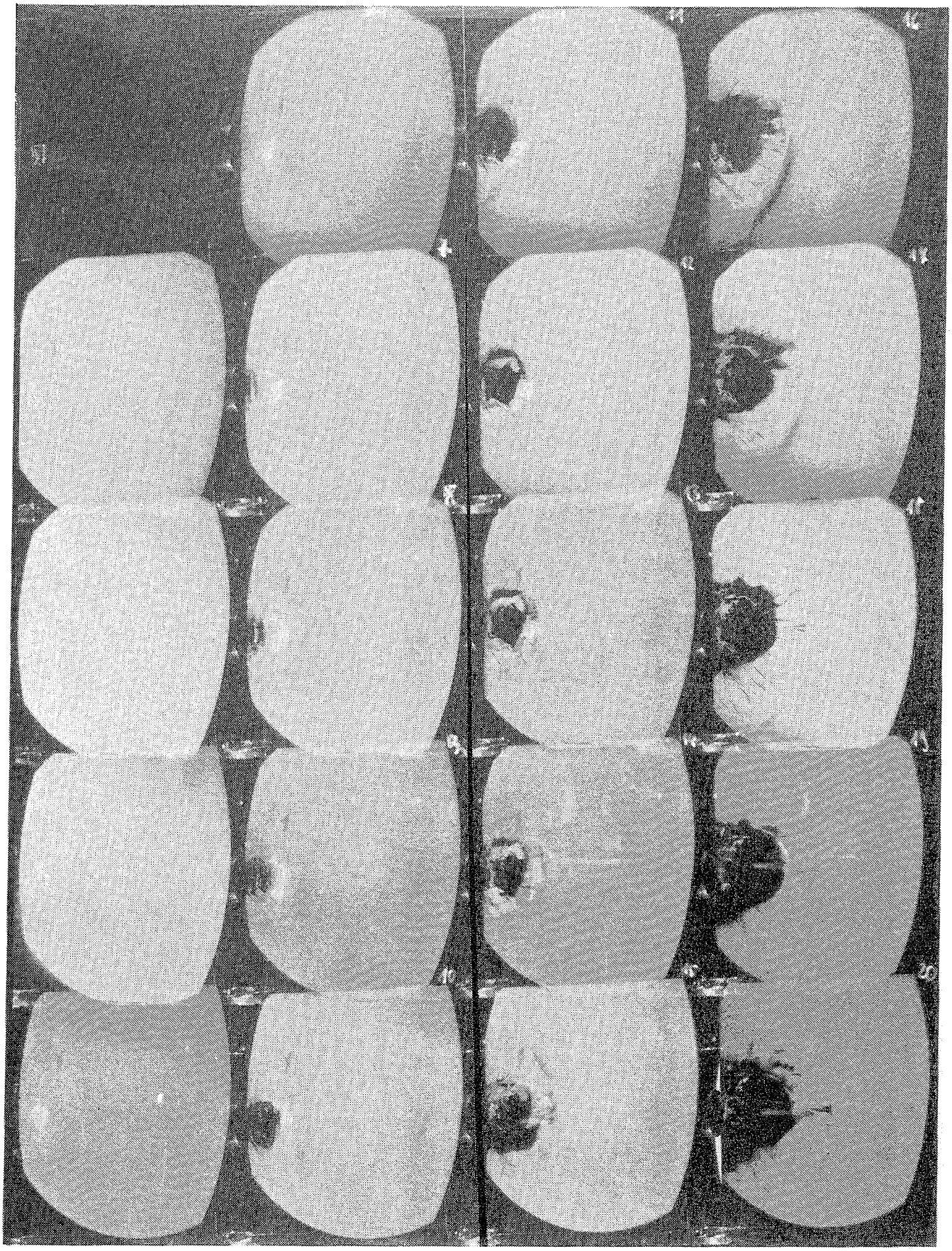
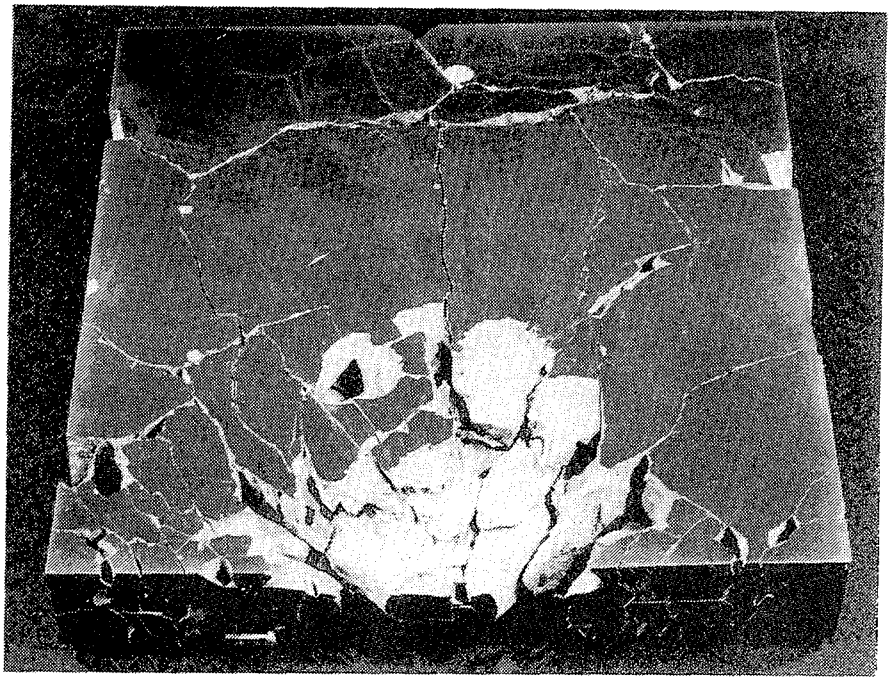


Figure 18.4b Complete series of high-speed photographs of shot no. 10600, right side, $\Delta t = 1\mu s$

The different fracture patterns and different fracture velocities indicate that in case of a thick target plate only a part of the cracks which are visible on the surfaces pierce the plate completely. This is confirmed by an inspection of the impacted specimen which could be almost totally rebuilt from the fragments. Figure 18.5a shows the left side of the specimen, Figure 18.5b shows the right side. The most striking feature of the recovered specimen is that most part of the material in the impact zone seems to be undestroyed. A slice of a truncated cone is formed by the cone cracks. The primary fractures and the shell-shaped fractures have destroyed the top layers of this part of the plate. The thickness of the destroyed layer at the impacted edge is about 10 mm on each side and decreases to zero at a distance of about 90 mm from the edge. The fragments from these zones and from the vicinity of the cone cracks are too small to reassemble these parts of the specimen. Nevertheless, only a very small amount of material is comminuted in this experiment. With a small target plate (100 mm x 100 mm x 10 mm) about 30 % of the target was comminuted at an impact velocity of 220 m/s. This indicates the significant influence of the release waves on the destruction of the specimens.

From the photograph in Figure 18.5a it can be recognized that a small fragment (marked with an arrow) was formed within the cone, in front of the projectile. A fracture surface parallel to the surfaces of the plate was examined by means of SEM. Figure 18.6 shows a micrograph were the fracture surface and the impacted edge can be seen. Figure 18.7 shows a section of the fracture surface near the impacted edge (double magnification in comparison to Figure 18.6). Especially this photograph reveals that material had been molten and again solidified in the impact zone. Additionally, comminuted material is found on the fracture surface in the vicinity of the impact zone. Figure 18.8a shows a section of the fracture surface at a distance of about 300 μm from the impacted edge. The size of the particles is approximately in the range from 0.3 μm to 1 μm. The amount of comminuted material decreases rapidly with increasing distance to the impact zone. The micrographs in Figures 18.8b and 18.8c show the fracture surface at distances of about 1 mm and 2 mm from the impacted edge. No sign of comminuted material is found at a distance of 2 mm.

a)



b)

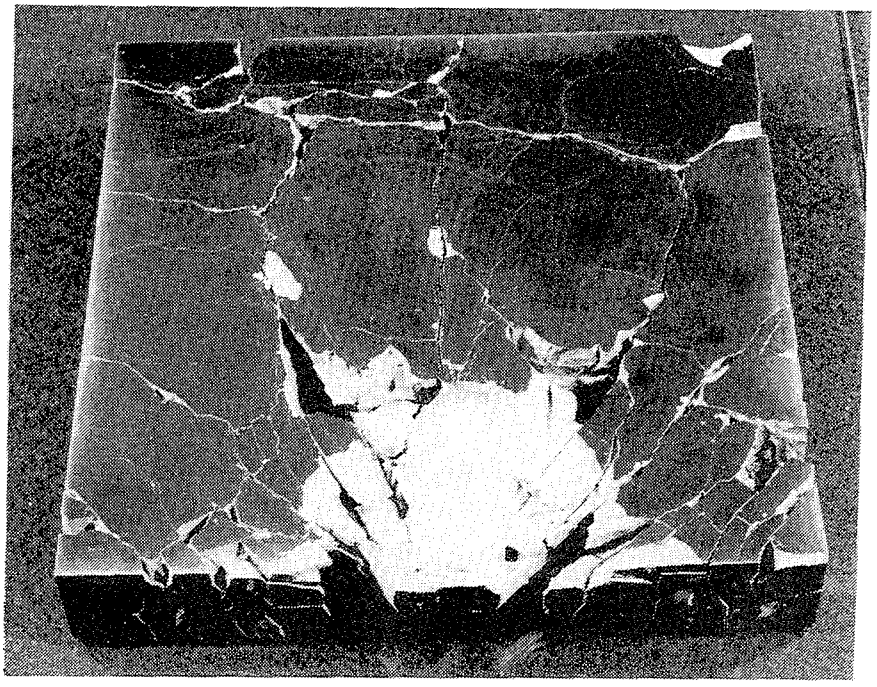


Figure 18.5 Reassembled specimen of shot no. 10600
a) left side, b) right side

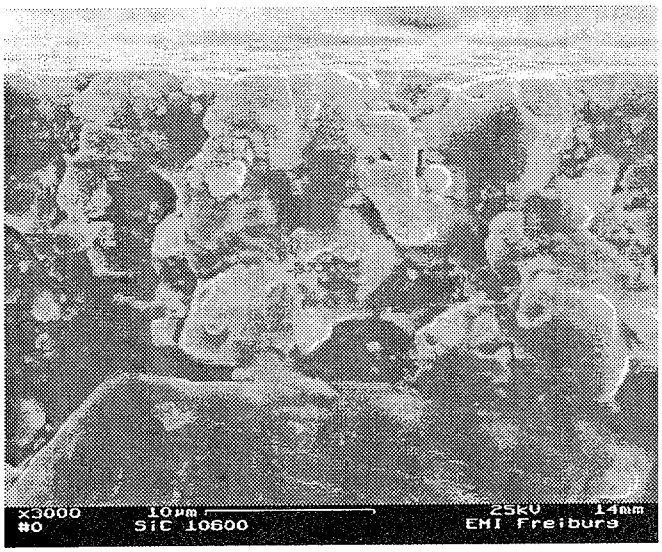


Figure 18.6 Fracture surface normal to the impacted edge of the specimen (visible in the upper part of the micrograph)

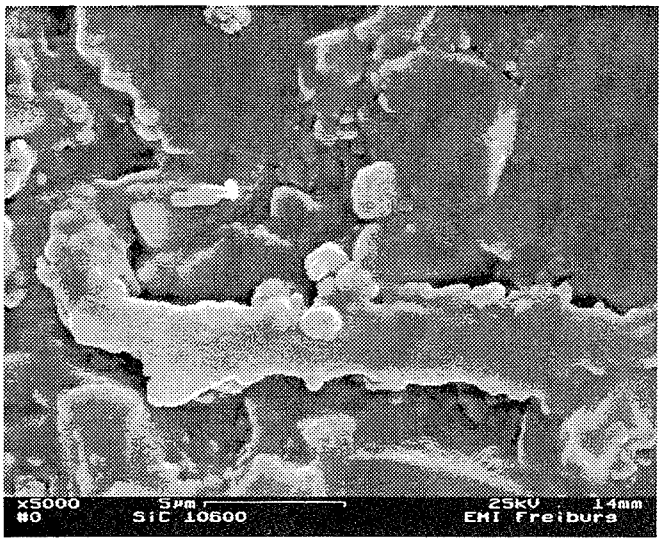
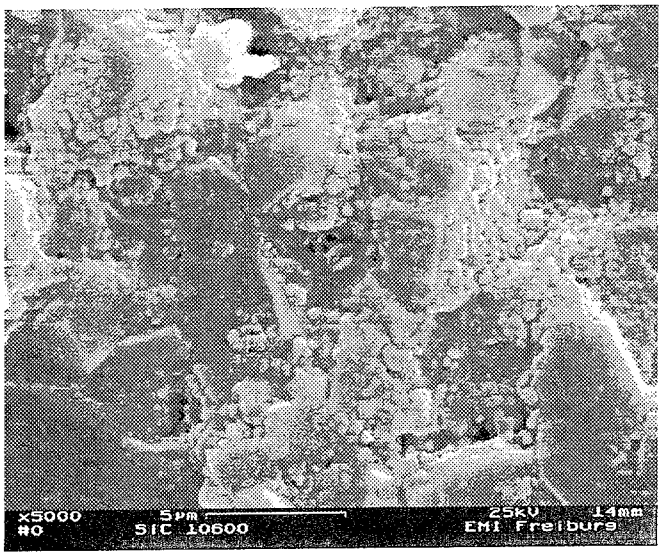
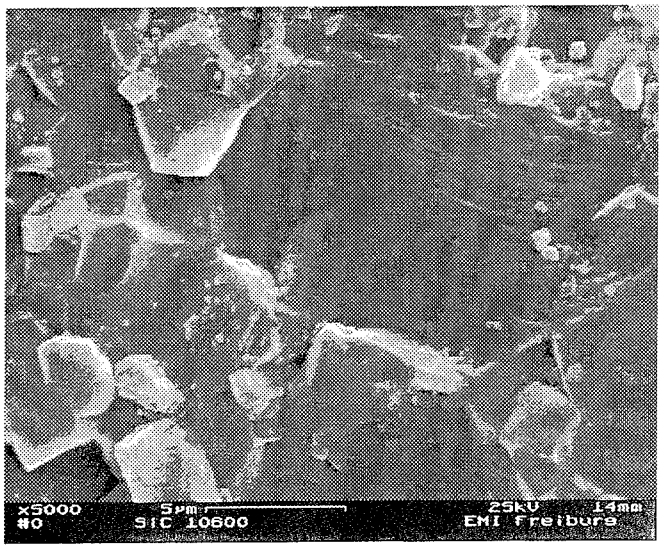


Figure 18.7 Micrograph of the fracture surface near the impacted edge

a)



b)



c)

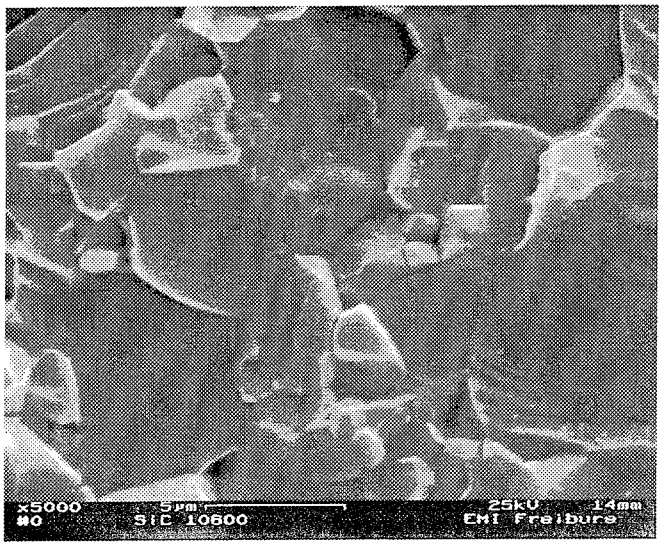


Figure 18.8 Micrographs of the fracture surface at different distances from the impacted edge, a) 300 μm, b) 1 mm, c) 2 mm

19. Summary of the Results with Ceramics

Plates of SiC, TiB_2 and Al_2O_3 were impacted with blunt steel cylinders at striking velocities between 20 m/s and 1000 m/s. Fracture propagation was visualized by means of a Cranz-Schardin camera within the first twenty microseconds before the projectile penetrated the target more than a few millimeters.

The experiments delivered a detailed picture of the destruction of the different types of ceramics before the projectiles penetrated the targets.

- The examined SiC and the Al_2O_3 exhibit similar fracture patterns and the same fracture types over the full velocity range considered. Single cracks and fracture cracks can be distinguished at impact velocities below 200 m/s.

- A dense field of short cracks is observed with TiB_2 already at lower impact velocities.

- In the impact velocity range from 200 m/s to 700 m/s all three ceramics are destroyed by a dense field of cracks.

- A further type of damage is observed with TiB_2 at impact velocities above 700 m/s. A field of black spots preceds the fracture front on the photographs which was due to the breakout of material at the surface of the specimen.

- Ceramographical investigations of TiB_2 fragments have shown that cracks within large grains as well as intercrystalline cracks are formed by coalescence of voids.

- A terminal crack velocity $v_{C,SiC} = 3490$ m/s $\pm$ 390 m/s is observed in SiC with those cracks which grow continuously and have sharp edges (smooth crack surfaces). This crack velocity is approximately half of the Rayleigh wave velocity. This finding corresponds to the experimental results with float glass and the optical glasses K5 and F6 where the relation $v_C \approx 0.5\ c_R$ was found, too. This type of fracture does not determine the damage velocity of the ceramics in the loading range considered in these investigations.

- The damage velocity (velocity of the fastest fracture) increases with increasing loading.

- All ceramics examined are destroyed at velocities close to longitudinal wave velocity at high loadings.

Final Remark:

The stress wave induced damage and fracture in differing glasses show similar behavior. Nevertheless, in the case of the heavy flint-glass SF6 a considerably great difference was observed between the experimentally determined terminal crack velocity (700 m/s) and that calculated from transversal and/or Rayleigh wave velocity on the basis of the fracture mechanics concept ($v_C \approx ½ \cdot c_R$ = 900 m/s). No explanation has been reached yet.

The fracture patterns and the fracture types observed with TiB_2 differ from that of SiC and Al_2O_3 with the several dynamical loading conditions. It is supposed that the dynamic behavior of the ceramics will be strongly influenced by their chemical composition and the kind of chemical bond, the ratio of ingredients, the grain sizes and the grain size distributions, the porosity and further mechanical properties. Therefore, the obtained data should be regarded as a data base for future investigation. They indicate that there is a need to intensify the study of the behavior of brittle material under dynamic loading to reach an improved description of the failure mechanisms.

Acknowledgement

We thank the U. S. Army Research Laboratory, Aberdeen Proving Ground, and the European Research Office of the U. S. Army, London, for funding this work. In particular we are obliged to Mr. W. Gooch for making these investigations possible and for his steady support.

We thank Mr. D. Preuß, Mr. J. Gonschorek and Mr. E. Zipfel who conducted the experiments very carefully. We also acknowledge the assistance of Mrs. E. Meßner in preparation of the manuscript and of Mrs. E. Franz in preparation of the photographs.

INTENTIONALLY LEFT BLANK.

20. References

[1] Rosenberg, Z., Bless, S. J., Yeshurun, Y., Okajima, K.: Proc. of "IMPACT 87", DGM-Informationsgesellschaft 1988, p. 491 ff.

[2] Woolsey, P., Kokidko, D., Mariano, S.: "Alternative Test Methodology for the Ballistic Performance of Armor Ceramics", Proc. 5th TACOM Armor Conf., 1989

[3] Hornemann, U., Rothenhäusler, H., Senf, H., Kalthoff, J. F., Winkler, S.: "Experimental Investigation of Wave and Fracture Propagation in Glass Slabs Loaded by Steel Cylinders at High Impact Velocities", Inst. Phys. Conf. Ser. No. 70, 3rd Conf. Mech. Prop. High Rates of Strain, Oxford, 1984

[4] Senf, H., Rothenhäusler, H.: "Crack Behaviour and Dynamic Response of Alumina Under Impact Loading", Shock-Wave and High-Strain-Rate Phenomena in Materials, Marc A. Meyers, Lawrence E. Murr, Karl. P. Staudhammer, MARCEL DEKKER, Inc., 1992

[5] Winkler, S.: "Experimental Investigation of Wave and Fracture Phenomena in Impacted Ceramics", Final Report 'Experiments on Sapphire', Fraunhofer-Institut für Werkstoffmechanik, Freiburg, IWM Report T 8/93, 1993

[6] Kerkhof, F.: "Bruchvorgänge in Gläsern", Verlag der Deutschen Glastechnischen Gesellschaft, Frankfurt/M., 1970

[7] Schardin, H.: "Results of Kinematographic Investigation of the Fracture Process in Glass", Technical Memorandum, Navy-NOTS TM 968, U. S. Naval Ordnance Test Station, China Lake, California, USA, p. 29, 1953

[8] Schardin, H.: "Ergebnisse der kinematographischen Untersuchung des Glasbruchvorganges", Glastechnische Berichte 23, 1950

[9] Vollkommer, H.: "Schlierenoptische Untersuchung des Schneidenstoßes auf eine Plattenkante", Ernst-Mach-Institut, Freiburg/Br., Bericht 1/67, 1967

[10] Beinert, J.: "Schlierenoptische Untersuchungen zur Ausbreitung kurzer elastischer Impulse in Platten", Fraunhofer-Institut für Festkörpermechanik, Freiburg/Br., 1974

[11] Senf, H., Rothenhäusler, H., Straßburger, E.: "Ausbreitung von Bruch- und Zerstörungsphänomenen in Gläsern bei hohen dynamischen Belastungen", Fraunhofer-Institut für Kurzzeitdynamik, Ernst-Mach-Institut, Weil am Rhein, EMI-Bericht 4/92, 1992

[12] Christie, D. G.: Trans. Soc. Glass Tech. **36T** 88, 1952

[13] Yoffe, E. M.: "The Moving Griffith Crack", Phil. Mag. **42** 739, 1951

[14] Craggs, R. M.: J. Mech. Phys. Solids **8** 66

[15] Kolsky, H.: "Wave Propagation Effects and Fracture",Proceedings of the Conference on Mechanical Properties at High Rates of Strain, Oxford, 1974, The Institute of Physics Conference Series Number 21

[16] Rasorenov, S. V., Kanel, G. I., Fortov, V. E., Abasehov, M. M.: "The Fracture of Glass under High-Pressure Impulsive Loading", High Pressure Research, Vol. 6, pp. 225-232, 1991

[17] Kanel, G. I., Rasorenov, S. V., Fortov, V. E.: "The Failure Waves and Spallations in Homogeneous Brittle Materials", Shock Compression of Condensed Matter 1991

[18] Brar, N. S., Rosenberg, Z., Bless, S. J.: "Spall Strength and Failure Waves in Glass", J. de Physique IV 1, C3 - 639, Proceedings of the 3rd DYMAT Conference, Strasbourg, 1991

[19] Brar, N. S., Bless, S. J.: "Failure Waves in Glass under Dynamic Compression", High Pressure Research, Vol. 10, pp. 773 - 784, 1992

[20] Raiser, G. F., Clifton, R. J.: "Failure Waves in Uniaxial Compression of an Aluminosilicate Glass", Proceedings of Joint AIRAPT/APS Conference, June 28 - July 2, 1993, Colorado Springs,CO

[21] Clifton, R. J.: "Analysis of Failure Waves in Glasses", Appl. Mech. Review, Vol 46, No 12, Part 1, December 1993

[22] Nahme, H.: private communication

[23] Senf, H., Straßburger, E., Rothenhäusler, H.: "Stress Wave Induced Damage and Fracture in Impacted Glasses", to be published in Proc. 4th DYMAT Conference, Oxford, 1994

[24] Straßburger, E., Senf, H., Rothenhäusler, H.: "Stoßwelleninduzierte Risse und Zerstörungen in Gläsern", Fraunhofer-Institut für Kurzzeitdynamik, Weil am Rhein, EMI Report 7/93, 1993

[25] Winkler, S., Senf, H., Rothenhäusler, H.: "Wave and Fracture Phenomena in Impacted Ceramics", Fraunhofer-Institut für Kurzzeitdynamik, Ernst-Mach-Institut, Weil am Rhein, EMI Report V 5/89, 1989 (Final Report Contract DAJA 45-88-C-0011)

NO. OF COPIES	ORGANIZATION
2	ADMINISTRATOR ATTN DTIC DDA DEFENSE TECHNICAL INFO CTR CAMERON STATION ALEXANDRIA VA 22304-6145
1	COMMANDER ATTN AMCAM US ARMY MATERIEL COMMAND 5001 EISENHOWER AVE ALEXANDRIA VA 22333-0001
1	DIRECTOR ATTN AMSRL OP SD TA US ARMY RESEARCH LAB 2800 POWDER MILL RD ADELPHI MD 20783-1145
3	DIRECTOR ATTN AMSRL OP SD TL US ARMY RESEARCH LAB 2800 POWDER MILL RD ADELPHI MD 20783-1145
1	DIRECTOR ATTN AMSRL OP SD TP US ARMY RESEARCH LAB 2800 POWDER MILL RD ADELPHI MD 20783-1145
2	COMMANDER ATTN SMCAR TDC US ARMY ARDEC PCTNY ARSNL NJ 07806-5000
1	DIRECTOR ATTN SMCAR CCB TL BENET LABORATORIES ARSENAL STREET WATERVLIET NY 12189-4050
1	DIR USA ADVANCED SYSTEMS ATTN AMSAT R NR MS 219 1 R&A OFC AMES RESEARCH CENTER MOFFETT FLD CA 94035-1000

NO. OF COPIES	ORGANIZATION
1	COMMANDER ATTN AMSMI RD CS R DOC US ARMY MISSILE COMMAND REDSTONE ARSNL AL 35898-5010
1	COMMANDER ATTN AMSTA JSK ARMOR ENG BR US ARMY TANK AUTOMOTIVE CMD WARREN MI 48397-5000
1	DIRECTOR ATTN ATRC WSR USA TRADOC ANALYSIS CMD WSMR NM 88002-5502
1	COMMANDANT ATTN ATSH CD SECURITY MGR US ARMY INFANTRY SCHOOL FT BENNING GA 31905-5660
	ABERDEEN PROVING GROUND
2	DIR USAMSAA ATTN AMXSY D AMXSY MP H COHEN
1	CDR USATECOM ATTN AMSTE TC
1	DIR USAERDEC ATTN SCBRD RT
1	CDR USACBDCOM ATTN AMSCB CII
1	DIR USARL ATTN AMSRL SL I
5	DIR USARL ATTN AMSRL OP AP L

NO. OF COPIES	ORGANIZATION
1	HQDA SARD TR R CHAIT WASH DC 20310-0103
2	CDR US ARMY TACOM ATTN AMSTA RSS J THOMPSON AMSTA RSK S GOODMAN WARREN MI 48397-5000
1	PM SURVIVABILITY SYS ATTN SFAE ASM SS T T DEAN WARREN MI 48397-5000
2	DIR US ARMY RSRCH OFC ATTN K IYER J BAILEY PO BOX 12211 RSRCH TRI PK NC 27709-2211
7	DIR USARL ATTN AMSRL MA DA J PRIFTI P WOOLSEY D DANDEKAR S CHOU R RAJENDRAN AMSRL MA C D VIECHNICKI M SLAVIN ARSENAL ST WATERTOWN MA 02172
1	CDR NGIC ATTN W MARLEY 220 SEVENTH AVE CHARLTSVL VA 22901-5391
1	CIA ATTN OSWR DSD W WALTMAN ROOM 5P0110 NHB WASH DC 20505
1	DIR ARPA ATTN LTC R KOCHER 3701 NORTH FAIRFAX DR ARLINGTON VA 22203-1714
1	CDR ERO USARDSG (UK) ATTN R REICHENBACH PSC 802 BOX 15 FPO AE 09499-1500

NO. OF COPIES	ORGANIZATION
3	DIR LLNL ATTN R GOGOLEWSKI MS L290 R LANDINGHAM L369 R WHIRLEY L122 PO BOX 808 LIVERMORE CA 94550
2	DIR LLNL ATTN D STEINBERG J REAUGH L32 PO BOX 808 LIVERMORE CA 94550
2	DIR LANL ATTN F ADDESSIO M BURKETT LOS ALAMOS NM 87545
2	DIR LANL ATTN E CORT F GAC LOS ALAMOS NM 87545
1	JET PROPULSION LAB ATTN M ADAMS IMPACT PHYSICS GROUP 4800 OAK GROVE DR PASADENA CA 91109-8099
2	DIR SNL ATTN D GRADY MS 0821 D CRAWFORD ORG 1533 PO BOX 5800 ALBUQUERQUE NM 87185
2	DIR SNL ATTN M FORRESTAL LUK PO BOX 5800 ALBUQUERQUE NM 87185
1	DIR SNL ATTN J ASAY MS 0548 PO BOX 5800 ALBUQUERQUE NM 87185
2	DIR SNL ATTN R BRANNON MS 0820 M KIPP MS 0820 PO BOX 5800 ALBUQUERQUE NM 87185

NO. OF COPIES	ORGANIZATION
2	IAT ATTN S BLESS R SUBRAMANIAN PO BOX 202797 AUSTIN TX 78720-2797
2	IAT ATTN T KIEHNE H FAIR PO BOX 202797 AUSTIN TX 78720-2797
2	UNITED DEFENSE LP ATTN V HORVATICH R RAJAGOPAL PO BOX 359 SANTA CLARA CA 95052-0359
2	UNITED DEFENSE LP ATTN M MIDDIONE J MARROW PO BOX 359 SANTA CLARA CA 95052-0359
1	ALME AND ASSOCS ATTN M ALME 9650 SANTIAGE RD STE 102 COLUMBIA MD 21045
1	NAVAL POST GRAD SCHOOL ATTN J STERNBERG CODE EW MONTEREY CA 93943
1	UNIV OF DAYTON RSRCH INST ATTN N BRAR KLA14 300 COLLEGE PARK DAYTON OH 45469-0182
2	UNIV OF DAYTON RSRCH INST ATTN A PIEKUTOWSKI D GROVE KLA14 300 COLLEGE PARK DAYTON OH 45469-0182
2	LANXIDE ARMOR PRODUCTS ATTN K LEIGHTON V KELSEY 1300 MARROWS RD NEWARK DE 19714-6077
1	LANXIDE ARMOR PRODUCTS ATTN R WOLFFE 1300 MARROWS RD NEWARK DE 19714-6077
1	GENERAL RSRCH CORP ATTN A CHARTERS 5383 HOLLISTER AVE SANTA BARBARA CA 93160-6770
1	UNIV OF CA SAN DIEGO ATTN S NEMAT NASSER DEPT OF APPLIED MECHS & ENGR SVCS R011 LA JOLLA CA 92093-0411
1	UNIV OF CA SAN DIEGO ATTN M MEYERS DEPT OF APPLIED MECHS & ENGR SVCS R011 LA JOLLA CA 92093-0411
1	POULTER LAB ATTN D CURRAN SRI INTERNATIONAL 333 RAVENSWOOD AVE MENLO PARK CA 94025
1	POULTER LAB ATTN R KLOOP SRI INTERNATIONAL 333 RAVENSWOOD AVE MENLO PARK CA 94025
1	POULTER LAB ATTN L SEAMAN SRI INTERNATIONAL 333 RAVENSWOOD AVE MENLO PARK CA 94025
1	POULTER LAB ATTN D SHOCKEY SRI INTERNATIONAL 333 RAVENSWOOD AVE MENLO PARK CA 94025
2	SOUTHWEST RSRCH INST ATTN C ANDERSON J RIEGEL 6220 CULEBRA RD SAN ANTONIO TX 78238

NO. OF COPIES	ORGANIZATION
1	SOUTHWEST RSRCH INST ATTN D LITTLEFIELD 6220 CULEBRA RD SOUTHWEST SAN ANTONIO TX 78238
2	AERONAUTICAL RSRCH ASSOCS ATTN R CONTILIANO J WALKER 50 WASHINGTON RD PRINCETON NJ 08540
1	CA RSRCH & TECH INC ATTN D ORPHAL 5117 JOHNSON DR PLEASANTON CA 94566
1	THE CARBORUNDUM CO ATTN R PALIA PO BOX 1054 NIAGRA FALLS NY 19302
2	CERCOM INC ATTN R PALICKA A EZIS 1960 WATSON WAY VISTA CA 92083
1	CERCOM INC ATTN G NELSON 1960 WATSON WAY VISTA CA 92083
1	BRIGGS CO ATTN J BACKOFFEN 2668 PETERSBOROUGH ST HERNDON VA 22071-2443
1	CENTURY DYNAMICS INC ATTN N BIRNBAUM 7700 EDGEWATER DR SUITE 626 OAKLAND CA 94621
1	APPLIED RSRCH ASSOCS INC ATTN J YATTEAU 5941 SO MIDDLEFIELD RD SUITE 100 LITTLETON CO 801123

NO. OF COPIES	ORGANIZATION
1	ZERNOW TECH SVCS ATTN L ZERNOW 425 W BONITA AVE SUITE 208 SAN DIMAS CA 91773
2	ADELMAN ASSOCS ATTN C CLINE M WILKENS 3301 EL AMINO RIAL SUITE 280 ATHERTA CA 94027
1	R J EICHELBERGER 409 W CATHERINE ST BEL AIR MD 21014-3613
1	CYPRESS INTERNATIONAL ATTN A CAPONECCHI 1201 E ABINGDON DR ALEXANDRIA VA 22314
1	DOW CHEMICAL INC ATTN K EPSTEIN ORDNANCE SYS 800 BUILDING MIDLAND MI 48667
1	CALKINS R&D INC ATTN N CALKINS 515 SEWARD PK AVE ALBUQUERQUE NM 87123
1	KERAMONT CORPORATION ATTN E SAVRUN 4231 S FREEMONT AVE TUSCON AZ 85714
1	KAMAN SCIENCES CORPORATION ATTN M NORMANDIA 1500 GARDEN OF THE GODS RD COLORADO SPRINGS CO 80933
1	SAIC ATTN J FURLONG MS 264 1710 GOODRIDGE DR PO BOX 1303 MCLEAN VA 22102

NO. OF COPIES	ORGANIZATION
1	BOMBS & WARHEAD BRANCH ATTN W COOK MUNITIONS DIVISION EGLIN AFB FL 32542
2	ALLIANT TECHSYSTEMS INC ATTN T HOLMQUIST G JOHNSON 7225 NORTHLAND DR BROOKLYN PARK MN 55428
2	GDLS ATTN W BURKE J ERIDON PO BOX 2094 WARREN MI 48090
1	BATTELLE EDGEWOOD ATTN A RICCHIAZZI 2113 EMMORTON PARK RD EDGEWOOD MD 21040
1	CORNING INC ATTN S HAGG SP DV 22 CORNING NY 14831
1	COORS CERAMICS CO ATTN R PARICIO STRUCTURAL DIV 600 NINTH ST GOLDEN CO 80401
1	SIMULA INC ATTN W PERCIBALLI 10016 SOUTH 51 ST PHOENIX AZ 85044
1	O GARA HESS & EISENHARDT ATTN C WILLIAMS 9113 LE SAINT DR FAIRFIELD OH 45014
2	BROWN UNIV ATTN M CLIFTON S SUNDARAM DIV OF ENGR PROVIDENCE RI 02912

NO. OF COPIES	ORGANIZATION
	ABERDEEN PROVING GROUND
	DIR USARL ATTN AMSRL WT W MORRISON AMSRL WT TD A GUPTA A DIETRICH JR T FARRAND G RANDERS PEHRSON J WALTER JR M SCHEIDLER J SANTIAGO JR K FRANK S SEGLETES M RAFTENBERG AMSRL WT TC F GRACE W WALTERS R SUMMERS L MAGNESS M LAMPSON K KIMSEY D SCHEFFLER G SILSBY W DE ROSSET AMSRL WT TA E HORWATH E RAPACKI JR W GILLICH G FILBEY JR W BRUCHEY JR Y HUANG W GOOCH JR 10 CPS H MEYER JR M BURKINS N RUPERT T HAVEL J RUNYEON M ZOLTOSKI G BULMASH AMSRL WT WD A NIILER AMSRL WT D ECCLESHALL AMSRL WT T T WRIGHT

NO. OF COPIES	ORGANIZATION
3	FRANHOFER INSTITUT FÜR KURZZEITDYNAMIK ERNST MACH INSTITUT ATTN H SENF E STRAßBURGER H ROTENHÄUSLER HAUPTSTRASSE 18 D 79 576 WEIL AM RHEIN GERMANY
3	FRANHOFER INSTITUT FÜR KURZZEITDYNAMIK ERNST MACH INSTITUT ATTN G SCHRÖDER A STILP V HOHLER ECKERSTRAßE 4 D 79 104 FREIBURG GERMANY
3	DEUTSCH FRANZÖSISCHES FORSCHUNGSINSTITUT SAINT LOUIS ATTN H ERNST H LERR K HOOG CÉDEX 5 RUE DU GÉNÉRAL CASSAGNOU F 68301 SAINT LOUIS FRANCE
5	DEFENCE RSRCH AGENCY ATTN W CARSON T HAWKINS B SHRUBSALL C FREW I CROUCH CHOBHAM LANE CHERTEY SURREY KT16 OEE UNITED KINGDOM
1	DEFENCE RSRCH AGENCY ATTN T BARTON FT HALSTEAD SEVEN OAKS KENT TN14 7BP UNITED KINGDOM
1	BATTELLE INGENIEURTECHNIK GMBH ATTN W FUCHE DUESSELDORFLER STR 9 D 65760 ESCHBORN GERMANY
1	DEUTSCHE AEROSPACE AG ATTN M HELD POSTFACH 13 40 D 86 523 SCHROBENHAUSEN GERMANY
5	RAPHAEL BALLISTICS CENTER ATTN Y PARTOM G ROSENBERG M MAYSELESS Z ROSENBERG Y YESHURUN BOX 2250 HAIFA 31021 ISRAEL
1	DYNAMEC RSRCH AB ATTN Å PERSSON PARADISGRÄND 7 S 151 36 SÖDERTÄLJE SWEDEN
1	DEFENCE RSRCH ESTABLISHMENT SUFFIELD ATTN C WEICKERT BOX 4000 MEDICINE HAT ALBERTA TIA 8K6 CANADA
4	CENTRE DE RECHERCHES ET D'ETUDES D'ARCUEIL ATTN F TARDIVAL C COTTENNOT S JONNEAUX H ORSINI 16 BIS AVENUE PRIEUR DE LA CÔTE D'OR F 94114 ARCUEIL CÉDEX FRANCE
1	INGENIEURBÜRO DEISENROTH ATTN F DEISENROTH AUF DE HARDT 33 35 D 5204 LOHMAR 1 GERMANY
1	CONDAT ATTN K THOMA MAXILLANSTR 28 8069 SCHEYERN FERNHAG GERMANY

NO. OF COPIES	ORGANIZATION
3	SWEDISH DEFENCE RSRCH ESTABLISHMENT ATTN B JANZON I MELLGARD L HOLMBERG BOX 551 S 147 25 TUMBA SWEDEN
2	TNO PRINS MAURITS LAB ATTN H PASMAN R YSSELSTEIN PO BOX 45 2280 AA RIJSWIJK LANGE KLEIWEG 137 RIJSWIJK NETHERLANDS
2	DEFENCE TECHNOLOGY AND PROCUREMENT AGENCY ATTN G LAUBE W ODERMATT BALLISTICS WEAPONS AND COMBAT VEHICLE TEST CENTER CH 3602 THUN SWITZERLAND
1	CELSIUS MATERIALTEKNIK KARLSKOGA AB ATTN L HELLNER S 691 80 KARLSKOGA SWEDEN
1	SWISS FEDERAL ARMAMENT WORKS ATTN W LANZ ALLMENDSSTRASSE 86 CH 3602 THUN SWITZERLAND
1	HIGH ENERGY DENSITY RSRCH CENTER ATTN G KANEL IZHORSKAYA 13 19 MOSCOW 127412 RUSSIAN REPUBLIC
1	HIGH ENERGY DENSITY RSRCH CENTER ATTN V FORTOV IZHORSKAYA 13 19 MOSCOW 127412 RUSSIAN REPUBLIC

NO. OF COPIES	ORGANIZATION
1	EMBASSY OF AUSTRALIA ATTN R WOODWARD COUNSELLOR DEFENCE SCIENCE 1601 MASSACHUSETTES AVE NW WASH DC 20036-2273 USA
1	IOFFE PHYSICO TECHNICAL INSTITUTE ATTN A KOZHUSHKO ST PERTERBURG 194021 RUSSIAN REPUBLIC
2	AERONAUTICAL & MARITIME RSRCH LAB ATTN N BURMAN S CIMPOERU PO BOX 4331 MELBOURNE VIC 3001 AUSTRALIA
1	TECHNION INSTITUTE OF TECHNOLOGY FACULTY OF MECHANICAL ENGINEERING ATTN S BODNER TECHNION CITY HAIFA 32000 ISRAEL
2	FEDERAL MINISTRY OF DEFENCE DIRECTORATE FOR EQUIPMENT & TECH LAND Rü V 2 ATTN D HAUG L REPPER POSTFACH 1328 53003 BONN GERMANY
1	CENTER d'ETUDES GRAMAT ATTN J CAGNOUX 46500 GRAMAT FRANCE

INTENTIONALLY LEFT BLANK.

USER EVALUATION SHEET/CHANGE OF ADDRESS

This Laboratory undertakes a continuing effort to improve the quality of the reports it publishes. Your comments/answers to the items/questions below will aid us in our efforts.

1. ARL Report Number ARL-CR-214 Date of Report February 1995

2. Date Report Received _____

3. Does this report satisfy a need? (Comment on purpose, related project, or other area of interest for which the report will be used.) _____

4. Specifically, how is the report being used? (Information source, design data, procedure, source of ideas, etc.) _____

5. Has the information in this report led to any quantitative savings as far as man-hours or dollars saved, operating costs avoided, or efficiencies achieved, etc? If so, please elaborate. _____

6. General Comments. What do you think should be changed to improve future reports? (Indicate changes to organization, technical content, format, etc.) _____

CURRENT ADDRESS

_____
Organization

_____
Name

_____
Street or P.O. Box No.

_____
City, State, Zip Code

7. If indicating a Change of Address or Address Correction, please provide the Current or Correct address above and the Old or Incorrect address below.

OLD ADDRESS

_____
Organization

_____
Name

_____
Street or P.O. Box No.

_____
City, State, Zip Code

(Remove this sheet, fold as indicated, tape closed, and mail.)

(DO NOT STAPLE)

DEPARTMENT OF THE ARMY

OFFICIAL BUSINESS

NO POSTAGE
NECESSARY
IF MAILED
IN THE
UNITED STATES

BUSINESS REPLY MAIL
FIRST CLASS PERMIT NO 0001, APG, MD

Postage will be paid by addressee

Director
U.S. Army Research Laboratory
ATTN: AMSRL-OP-AP-L
Aberdeen Proving Ground, MD 21005-5066